Dipl.-Ing. Clemens Dorfmann

Flow Phenomena in a Reservoir investigated by Field Measurements and Numerical Modelling

DOCTORAL THESIS

to achieve the university degree of

Doktor der technischen Wissenschaften

submitted to

Graz University of Technology

Supervisor

Univ.-Prof. Dipl.-Ing. Dr.techn. Gerald Zenz
Institute of Hydraulic Engineering and Water Resources Management

External Reviewers

Prof. Dr. Franc Steinman - University of Ljubljana
Prof. Dr. Jean-Michel Hervouet

Graz, July 2017

AFFIDAVIT

I declare that I have authored this thesis independently, that I have not used other than the declared sources/resources, and that I have explicitly indicated all material which has been quoted either literally or by content from the sources used. The text document uploaded to TUGRAZonline is identical to the present doctoral thesis.

25th July 2017

Date

Signature

Abstract

Natural river courses typically are in a dynamic equilibrium with balance in water flow and sediment transport. The construction of dams and reservoirs alter the dynamic balance regarding water flow, sediment budget and associated river morphology. The impounding at a run-of-river hydro power plant causes the deposition of transported sediment in the reservoir which has a possible impact on flood safety, aquatic ecology or operational management. The shape of a shallow reservoir can have a significant influence on the developing flow fields and the sedimentation behaviour. The knowledge of the large-scale flow velocity distributions is essential for an effective reservoir management in terms of prediction of preferential sedimentation zones or increase of the flushing efficiency. Hence, the predictive capability of experimental and numerical models to simulate developing flow fields in shallow reservoirs is of high practical relevance.

This thesis focuses on the investigation of flow phenomena in a prototype-scale shallow reservoir at a run-of-river hydro power plant. The reservoir is characterized by a gradual horizontal expansion zone. The research is based on a physical model study of the case study which dealt with the optimization of the sediment management in the reservoir. The experimental results demonstrated that the large-scale flow field, in terms of main stream location, varies, depending on the applied steady hydraulic boundary conditions. In the physical model a training structure was developed in order to align the flow fields for different steady flow conditions. The implementation of the physical model results in the field has provided a unique opportunity to assess in prototype scale the developing flow fields by means of field measurements and numerical modelling.

In the prototype Acoustic Doppler Current Profiler (ADCP) velocity measurements are carried out. The measurements capture the developing large-scale flow fields, the horizontal shear layers and flow redistributions in the reservoir. The ADCP measurements are able to replicate the experimental results. Furthermore, the measurements reveal the unsteady meandering flow behaviour in the reservoir. In addition to the study of the large-scale flow fields, the estimation of bed shear stress, roughness height as well as turbulent kinetic energy by means of two stationary ADCP measurements is investigated.

The three-dimensional and two-dimensional depth-averaged numerical simulations aim at identifying the sensitivities in numerical modelling of gradual expansion flow on real bathymetry and flow conditions. With both numerical models extensive parameter studies are carried out in order to investigate the principal physical and numerical factors which control the resulting simulated flow behaviour in the reservoir. The steady simulations focus in particular on the variation of bed resistance, turbulence model and hydraulic boundary conditions. Unsteady two-dimensional depth-averaged simulations investigate and attempt to replicate unsteady meandering flow measured in two ADCP field campaigns by applying the measured time-varying discharges and water levels in the numerical model.

Kurzfassung

Der Wasser- und Sedimenthaushalt in natürlichen Flüssen ist typischerweise in einem dynamischen Gleichgewicht. Der Bau von Dämmen und Stauräumen verändert dieses Gleichgewicht. Der Aufstau von Stauräumen bei Flusskraftwerken verursacht die Anlandung von transportiertem Sediment mit möglichen Auswirkungen auf Hochwassersicherheit, Ökologie und Kraftwerksmanagement. Die Gestaltung bzw. die Form des Stauraums kann einen signifikanten Einfluss auf das Strömungs- und Sedimentationsverhalten haben. Die Kenntnis des Strömungsverhaltens ist essentiell für ein effizientes Stauraummanagement bezüglich der Prognose des räumlichen Sedimentationsverhaltens. Folglich ist die Prognosefähigkeit von physikalischen und numerischen Modellen für die Simulation des Strömungsverhaltens in flachen Stauräumen von großer Bedeutung.

Die Dissertation untersucht die auftretenden Strömungsphänomene in einem Stauraum eines Flusskraftwerks, welcher durch eine markante Aufweitungszone gekennzeichnet ist. Die Forschungsarbeit basiert auf einen physikalischen Modellversuch des Stauraums. Die experimentellen Untersuchungen wiesen nach, dass sich die Position der Hauptströmung verändert in Abhängigkeit der hydraulischen Randbedingung. Im physikalischen Modellversuch wurde eine Leitstruktur entwickelt mit dem Ziel, die Hauptströmungen für unterschiedliche hydraulische Lastfälle anzupassen. Das nicht überströmbare Leitwerk wurde im Prototyp eingebaut. Mit der Umsetzung im Stauraum konnten die auftretenden Strömungsphänomene vor und nach Einbau der Leitstruktur mittels Feldmessungen und numerischen Modellen im Naturmaßstab untersucht werden.

Im Prototyp wurden Acoustic Doppler Current Profiler (ADCP) Geschwindigkeits-messungen durchgeführt. In mehreren Messkampagnen konnten die großräumigen Strömungsstrukturen, die horizontalen Scherschichten und die Strömungsumwälzungen bestimmt werden. Es konnte nachgewiesen werden, dass unter bestimmten hydraulischen Randbedingungen ein instationäres Strömungsverhalten mit mäandrierender Hauptströmung auftritt. Zusätzlich zu diesen Messkampagnen wurden mittels zwei örtlich, stationären ADCP Messungen untersucht, ob mittels der ADCP Messmethode in einem Flussstauraum die quantitative Bestimmung der Schubspannung, der Rauheit und der turbulenten kinetischen Energie möglich ist.

Die dreidimensionalen und zweidimensionalen tiefengemittelten numerischen Simulationen hatten zum Ziel, die Sensitivitäten in der numerischen Modellierung von Aufweitungs-strömungen zu erfassen. In beiden Modellen wurden in Studien die physikalischen und numerischen Parameter untersucht, welche die numerische Berechnung der Aufweitungströmung beeinflussen. In den stationären Simulationen wurden insbesondere die Rauheit, Turbulenzmodell und hydraulische Randbedingungen untersucht. In instationären zweidimensionalen tiefengemittelten Simulationen wurde versucht, das in zwei ADCP Messkampagnen gemessenen instationäre Strömungsverhalten numerisch zu reproduzieren.

Acknowledgements

This thesis was written during my time at the Institute of Hydraulic Engineering and Water Resources Management - Graz University of Technology. Without the guidance and encouragement of several people this thesis wouldn't exist.

First of all I want to say thank you to Univ.-Prof. Dipl.-Ing. Dr.techn. Gerald Zenz for his review, guidance, critical thoughts and advises. I want to express my sincere gratitude to Prof. Franc Steinman and Prof. Jean-Michel Hervouet for reviewing this thesis.

I would also like to express my appreciation to Helmut Knoblauch and the staff of the hydraulic laboratory who supported the initial project with their knowledge and experience in the area of hydraulic model tests. Many thanks to all my colleagues from the Institute of Hydraulic Engineering and Water Resources Management for the good atmosphere. I want to say thank you especially to Markus Goldgruber, Shervin Shahriari and Josef Schneider for our technical and philosophical discussions and amusing talks during and after work.

The original project was funded by Verbund Hydro Power. Many thanks to the people from the branch office Villach who accompanied the project and helped in the measurement campaigns. A special thank you goes to Andreas Moser who greatly encouraged and supported me with his detailed knowledge about the fascinating river Drau.

Thanks to all professors, assistants, colleagues and friends who helped me on my way. In particular, I want to name Prof. Nils Reidar Olsen who was always willing to listen to my questions. Special thanks to the developers of the great open source modelling suite openTelemac – one feels supported by the community.

I would like to express my gratitude to my parents, my brother and sisters for their support in all circumstances.

My last and biggest thank you goes to Christina, the Astonishing, for her love and patience. Thank you so much.

I dedicate the thesis to my father Anton and to my sister Veronika. Remembered with love.

Essentially, all models are wrong, but some are useful. (George E. Box)

Contents

List of Symbols

C	constant in the Turbulent Kinetic Energy method	-
C_f	dimensionless quadratic friction coefficient	-
C_h	Chezy coefficient	$m^{1/2}/s$
C_l	empirical coefficient in the depth-averaged Mixing Length model	-
D_l	longitudinal dispersion	m^2/s
D_t	transversal dispersion	m^2/s
F	force	N
Fr	Froude number	-
L_R	horizontal scale factor	-
P	pressure	N/m^2
P_k	production of turbulent kinetic energy in the k-ε turbulence model	J/kg
$P_{\varepsilon v}$	source term for turbulent production in the depth-averaged k-ε model	J/kg
P_{kv}	source term for turbulent production in the depth-averaged k-ε model	J/kg
Re_*	roughness Reynolds number	-
R_h	hydraulic radius	m
S	source term in the momentum or continuity equation	m/s^2
T	depth-averaged Reynolds stress	N/m^2
U, V, W	flow velocity components in the in the x,y,z directions	m/s
U^*	shear velocity	m/s
Z	free surface elevation	m
α_t	proportionality constant in the Elder and Mixing Length turbulence model	-
ε	dissipation rate of the turbulent kinetic energy in the k-ε turbulence model	m^2/s^3
ε_{in}	dissipation rate at the inflow boundary in the k-ε model	m^2/s^3
ε_w	dissipation rate at the wall node in the k-ε model	m^2/s^3

ε_{ws}	dissipation rate at the water surface in the k-ε model	m^2/s^3
η	molecular dynamic viscosity	N s/m^2
κ	Von Kármán constant (set to $\kappa = 0.4$)	-
λ	wave length	m
μ_i	mean value of a spatial cluster of velocity components u_i	m/s
ν	kinematic viscosity	m^2/s
ν_t	turbulent eddy viscosity	m^2/s
ν_t^H	horizontal component of the turbulent viscosity ν_t	m^2/s
ν_t^V	vertical component of the turbulent viscosity ν_t	m^2/s
ρ	fluid density	kg/m^3
$\rho\overline{u_i' u_j'}$	Reynolds stress	N/m^2
σ_ε	empirical constant in the k-ε turbulence model	-
σ_k	empirical constant in the k-ε turbulence model	-
σ_i	standard deviation of a velocity component u_i	m/s
τ	shear stress	N/m^2
τ_b	bed shear stress	N/m^2
φ	absolute angle between velocity vectors at the bottom and the water surface	deg
c	speed of sound	m/s
$c_{1\varepsilon}$	empirical constant in the k-ε turbulence model	-
$c_{2\varepsilon}$	empirical constant in the k-ε turbulence model	-
c_μ	empirical constant in the k-ε turbulence model	-
c_k	empirical parameter in the depth-averaged k-ε turbulence model	-
c_ε	empirical parameter in the depth-averaged k-ε turbulence model	-
d_i	relative deviation of a velocity component u_i	-
f	frequency	Hz
f_D	Doppler shift frequency	Hz
f_S	frequency of sound	Hz

g	gravity acceleration	m/s^2
h	water depth	m
k	turbulent kinetic energy in the k-ε turbulence model	J/kg
k_{in}	turbulent kinetic energy at the inflow boundary in the k-ε model	J/kg
k_w	turbulent kinetic energy at the wall node in the k-ε model	J/kg
k_s	equivalent roughness height	m
k_{st}	Strickler coefficient	m$^{1/3}$/s
l_m	mixing length	m
$l_{m,w}$	mixing length at the wall node in the depth-averaged Mixing Length model	m
l_h	horizontal mixing length	m
l_v	vertical mixing length	m
n	vertical distortion factor	-
p	instantaneous pressure	N/m^2
t	time	s
u_i	instantaneous flow velocity in the direction i	m/s
$\overline{u_i'^2}$	variance of instantaneous velocity component u_i	m^2/s^2
$\overline{u_{i,corr}'^2}$	variance of velocity component u_i corrected by instrument noise	m^2/s^2
$\vec{u}_{bed}$	flow velocity vector at the bottom	m/s
$\vec{u}_{ws}$	flow velocity vector at the water surface	m/s
x, y, z	spatial geometrical scales in the Cartesian coordinate system	m

1 Introduction

Rivers in a natural state typically are systems in dynamic equilibrium with balance in water flow and sediment transport. Human activity changes the form of river courses. Anthropogenic uses and impacts such as construction of dams and reservoirs alter the dynamic balance regarding the water flow and the sediment budget. The impounding at a run-of-river hydro power plant causes the decrease of the flow velocities which leads to sedimentation of the transported bed load and suspended load in the reservoir. The progressive sedimentation can have a negative impact on the flood safety and may reduce the efficiency or even the life span of the turbines of the power plant due to abrasion. Moreover, the decreased storage capacity can limit the energy production. The reservoir management, e.g. by means of dredging works or reservoir flushing, entails relevant operating costs.

Transportation, deposition, remobilization or resuspension of sediment is governed by the flow velocity. In shallow reservoirs the developing large-scale flow velocity distributions or flow fields may have a strong influence on the spatial pattern of sediment deposits and overall trapping efficiency. For prediction of preferential sedimentation zones or increase of flushing efficiency in complex reservoir geometries, detailed knowledge of spatial velocity distributions is essential for effective reservoir management (Dorfmann and Zenz, 2013a).

In the past most of the reservoirs were designed by taking into account the storage volume only, but without considering its shape. In the research, the study on the influence of the shape of the reservoir on the developing flow field and sedimentation has grown interest for some time. The research works focused on experimental and numerical investigations of shallow, rectangular symmetrical basins with sudden expansion at the entrance and abrupt contraction at the outlet (Kantoush, 2008; Dewals et al., 2008; Dufresne et al., 2010a, 2010b, 2011; Camnasio et al., 2011; Peltier et al., 2014, 2015). In the studies different lateral expansion ratios and lengths were investigated. These research works show the complexity of flows in rectangular shallow reservoirs, despite their simple configuration. Depending on the geometry and hydraulic characteristics, different types of flow patterns develop: channel-like flow, symmetric flow patterns characterized by two or four large eddies, asymmetrical flow patterns and meandering flows. As Peltier et al. (2015) states, the hydraulic conditions and the geometries leading to symmetric and asymmetric flows in shallow rectangular reservoirs are well documented in literature. However, only a few experimental and numerical studies dealt with developing meandering flows in shallow rectangular reservoirs. The meandering jet causes a wider spreading of sediments on both sides of the jet, compared to a configuration without meandering jet. This can result in significantly other spatial patterns of sediment deposits and overall trapping efficiencies of the reservoir. Therefore, the predictive capability of experimental and numerical models to simulate developing complex flow fields in shallow reservoirs is of high practical relevance (Peltier et al., 2013).

This thesis focuses on the investigation of developing flow phenomena in a prototype-scale shallow reservoir which is characterized by a gradual horizontal expansion zone. Intensive literature review didn't yield any studies on such investigations in prototype-scale. The aim is investigation and analysis of developing flow fields in the reservoir by means of field measurements and numerical modelling. In this context the research also wants to identify challenges in measuring and assessing complex flow fields in prototype-scale as well as demonstrate the sensitivities in numerical modelling on real bathymetry and flow conditions.

The study presented here is based on the research project "Sediment management of the reservoir of the run-of-river hydro power plant Feistritz - Ludmannsdorf". The project dealt with optimization of the reservoir management by means of a physical model study. At first, the developing flow fields in the reservoir were investigated. Second, the physical model experiments aimed at finding optimal positioning and design of training structures with purpose of aligning the flow fields under varying hydraulic flow conditions. In turn, it should reduce the disordered sedimentation and lead to the increase of the flushing efficiency. Based on the physical model results a non-submerged training structure was implemented in the prototype. The case study and results from the physical model study serve as basis for the investigations presented in this thesis.

1.1 Objectives of the research

The research questions examined in this thesis are summarized as follows:

- Is the Acoustic Doppler Current Profiler (ADCP) velocity measurement technique basically capable of capturing the complex flow pattern in flow conditions in which very low flow velocities prevail?
- Can ADCP field measurements prove the validity of the physical model experiments of the reservoir?
- Does the flow field in the prototype have an unsteady meandering behaviour? Is it possible to capture the meandering flows by means of ADCP measurements?
- What impact has the installed non-submerged groyne in the prototype on the developing flow field? Can the groyne stabilize the flow field for different hydraulic boundary conditions?
- Is ADCP technique feasible to estimate turbulent kinetic energy, bed shear stress and roughness height in reservoir-like flow conditions?
- Which physical and numerical factors in numerical simulations are controlling the flow field to be calculated in terms of main stream development: variation of bottom roughness, turbulence model, hydraulic boundary conditions, installation of the groyne, etc.?

- Is the computed flow field stringently three-dimensional or can the large-scale flow phenomena be resolved by means of the 2D depth-averaged shallow water assumption?

- Can the 2D depth-averaged numerical model replicate the unstable meandering flow fields which were measured in the ADCP field campaigns?

For the purpose of this research two further objectives of the thesis can be stated:

- The development of an open source postprocessing software with the aim at providing specialized and concurrently flexible as well as fast methods to process and analyse ADCP measurement data.

- The implementation of the depth-averaged Mixing Length turbulence model in the open source 2D depth-averaged shallow water solver Telemac-2D. This turbulence model is a viable alternative to the already existing zero-equation turbulence models in Telemac-2D, especially in cases in which transverse shear is the dominant turbulence generation mechanism.

1.2 Methodologies and structure of the thesis

In this thesis the three classical methodologies of hydraulic research – physical model experiments, field measurements and numerical modelling – have been employed in order to meet the objectives.

Chapter II outlines the fundamentals of numerical modelling of open channel flow. In this research the three-dimensional computational fluid dynamics program Telemac-3D and the two-dimensional depth-averaged shallow water solver Telemac-2D are used. Both programs belong to the open source suite TELEMAC-MASCARET. The discussion focuses on the numerical approaches of both programs, in particular resistance modelling, turbulence modelling and hydraulic boundary conditions. The last section of this chapter explains the theory of the depth-averaged Mixing Length turbulence model, the motivation for the implementation in Telemac-2D and its validation by means of a laboratory experiment. Along with a comprehensive literature study the main features of the depth-averaged Mixing Length turbulence model are presented and discussed.

Chapter III starts by introducing basic principles of the Acoustic Doppler Current Profiler (ADCP) measurement technique and provides a literature overview of the fields of application in research. The development of the open source postprocessing software ADCPtool, its purpose and the functionalities are explained.

Chapter IV presents physical model experiments of the case study. First, the case study and the investigated study area are introduced in detail. The relevant hydraulic load cases and the physical model setup are described. The methodology of using the ADCP technique for measuring flow velocities in the model is discussed. In the last section of this chapter the

main physical experiments and their results in terms of measured flow fields are presented for the cases without and with implementation of the non-submerged groyne.

The flow fields in the prototype are investigated by means of ADCP velocity measurements. *Chapter V* presents and discusses five measurement campaigns and their results. Two of them are carried out before installation of the groyne and three campaigns after its installation. For a comprehensive analysis of the developing flow fields in the expanded area, the campaigns differ in hydraulic boundary conditions in terms of discharge and operating water level. In addition to the investigation of large-scale flow fields, the estimation of bed shear stress, roughness height as well as turbulent kinetic energy by means of two single-point ADCP measurements is presented and discussed. The results are compared with approaches of literature. In the final section two ADCP field campaigns are compared with the physical model experiments.

Chapter VI presents 3D and 2D depth-averaged numerical simulations of the developing flow fields in the reservoir. With both numerical models extensive parameter studies are carried out. They investigate the principal physical and numerical factors which control the resulting simulated flow behaviours for the cases with and without installation of the groyne. A special emphasis is given on the Mixing length turbulence model implemented in Telemac-2D and the variation of its semi-empirical coefficients. In the last section unsteady 2D depth-averaged numerical simulations are compared with two ADCP measurement campaigns.

In *Chapter VII* the results and findings are summarized and discussed. The thesis is concluding with recommendations for further research.

2 Numerical Modelling of Open Channel Flow

In this work the three-dimensional numerical model Telemac-3D and the two-dimensional depth-averaged numerical model Telemac-2D have been used.

TELEMAC-MASCARET is an integrated open source suite of solvers for use in the field of free-surface flow (www.opentelemac.org).
The main components are the solvers **Telemac-2D** for solving the two-dimensional shallow water Saint-Venant equations and **Telemac-3D** for solving the three-dimensional Navier-Stokes equations with or without the hydrostatic pressure assumption. Both modules can take several processes into account by solving the transport equations of intrinsic quantities like contaminants, salinity and temperature.
The suite consists of additional modules for simulating one-dimensional flow (Mascaret), sediment transport in 2D (Sisyphe) or 3D (Sedi-3D), wave propagation in the coastal zone (Tomawac), wave agitation in harbours (Artemis) and groundwater flows (Estel-2D and Estel-3D). The system has been developed by the Laboratoire National d'Hydraulique, a department of Electricité de France's Research and Development Division. Since 2010 it has been available as open source and is developed and managed by the Open Telemac-Mascaret Consortium. The modules have been used in the context of several research and industrial projects. Further informations about the individual modules, the community forum and a list of publications can be found on the above mentioned website. The main theory of the numerical models Telemac-2D and Telemac-3D is described in Hervouet (2007).

In the subsequent sections the fundamental equations and briefly the numerical techniques employed by the numerical models Telemac-3D and Telemac-2D are presented. The elaboration mainly covers the methods and approaches which have been used in the context of the presented research. Section 2.3 in detail presents and discusses the features of the newly implemented depth-averaged Mixing Length turbulence model in Telemac-2D.

2.1 3D numerical modelling with Telemac-3D

2.1.1 Governing equations

The main equations governing fluid flow are the Navier-Stokes equations. They describe the instantaneous motions of turbulent flow and are derived from fundamental physical laws: conservation of fluid mass and conservation of momentum.
For incompressible and transient flow with constant density these laws are expressed by the continuity equation (2.1) and the momentum equation (2.2):

$$\frac{\partial u_i}{\partial x_i} = 0 \tag{2.1}$$

$$\frac{\partial u_i}{\partial t} + u_j \frac{\partial u_i}{\partial x_j} = -\frac{1}{\rho}\frac{\partial p}{\partial x_i} + \frac{1}{\rho}\frac{\partial}{\partial x_j}\eta\left(\frac{\partial u_i}{\partial x_j} + \frac{\partial u_j}{\partial x_i}\right) + g_i + F_i \tag{2.2}$$

where t is the time, x_i is the spatial geometrical scale in the Cartesian direction i ($i = 1,2,3$), u_i is the instantaneous velocity component in the direction i, p is the instantaneous pressure, ρ is the fluid density (constant in time and space), η is the molecular dynamic viscosity, g_i represents the gravity ($g_1 = g_2 = 0, g_3 = -g$) and F_i represents external forces other than pressure and gravity, e.g. the Coriolis acceleration.

The Navier-Stokes equations in (2.1) and (2.2) form a system of four equations with the four unknowns pressure and flow velocity components in the three spatial directions. They can be solved directly for laminar flow conditions. However, free surface flows are almost always turbulent where physical quantities like velocity and pressure show rapid variations in time and space. As stated by Rodi (1984), turbulent flow is characterized by highly random, unsteady and three-dimensional fluid motion.
For turbulent flows with high Reynolds numbers, in most cases the Navier-Stokes equations cannot be solved directly because of limited computer capacity. Therefore, for engineering purposes, in which the description and the solution of the mean motions of turbulent flow are relevant, the instantaneous physical quantities can be separated into mean and fluctuating quantities based on the approach by Osborne Reynolds: $u_i = U_i + u_i'$ and $p = P + p'$ with U_i the mean velocity, P the mean pressure and u_i' and p' the fluctuating turbulent quantities, respectively. The premise for the Reynolds decomposition is, that the averaging time is much longer than the time scale of turbulent motion. The Reynolds-averaging of equations (2.1) and (2.2) yields the mean continuity and momentum equations which are named the Reynolds-averaged-Navier-Stokes (RANS) equations:

$$\frac{\partial U_i}{\partial x_i} = 0 \tag{2.3}$$

$$\frac{\partial U_i}{\partial t} + U_j \frac{\partial U_i}{\partial x_j} = -\frac{1}{\rho}\frac{\partial P}{\partial x_i} + \frac{1}{\rho}\frac{\partial}{\partial x_j}\left[\eta\left(\frac{\partial u_i}{\partial x_j} + \frac{\partial u_j}{\partial x_i}\right) - \rho\overline{u_i' u_j'}\right] + g_i + F_i \tag{2.4}$$

The continuity equation (2.3) is unchanged, averaged values and fluctuations all being zero. In the momentum equation (2.4) the averaging process has introduced the so called turbulent

stress or Reynolds stress term $-\rho\overline{u_i' u_j'}$ which represents the momentum transport due to turbulent motions.
The momentum equation (2.4) consists of seven terms: on the left side of the equation the transient term (local acceleration) and advection term; on the right side of the equation the pressure term, the viscous stress term, the Reynolds stress term, the gravity term and a source term representing external forces. In fully turbulent flow turbulent stresses dominate and the viscous stress term could therefore be omitted in numerical models.

2.1.2 The Law of the wall

The outer boundaries of a numerical domain or the boundary of an internal island are usually modelled as solid and impermeable walls where the no-slip condition is employed. The velocity region which is influenced by the wall is called the turbulent boundary layer.

In hydraulic smooth flow conditions near the wall a thin viscous (laminar) sublayer exists in which turbulence is suppressed by viscosity and a linear velocity distribution is present. In hydraulic rough flow conditions the characteristic roughness size of the wall is greater than the thickness of the viscous sublayer and this sublayer cannot develop.
The integration of the momentum equations through the viscous sublayer or individual roughness elements requires many grid points in order to resolve the high velocity gradients in this zone which, in turn, would lead to very expensive computations. To overcome this handicap, most of the 3D numerical models for open channel flow use the so called law of the wall or log-law. The first grid point (or cell center) adjacent to the wall is placed in the logarithmic wall region, outside the viscous sublayer and above the roughness elements.

The universal law of the wall was first published by Theodore von Kármán (1930):

$$\frac{U}{U^*} = \frac{1}{\kappa}\ln(y^+) + A \tag{2.5}$$

where U^* is the shear velocity, $y^+ = yU^*/\nu$ is the dimensionless wall distance with y the distance from the wall and ν the kinematic viscosity. A is an integral constant.
The logarithmic layer starts at $y^+ = 30$ and it is commonly assumed that the log-law is inherently valid only in the wall region, for $y/h < 0.2$, with y the vertical distance from the river bed and h the water depth. Though, the wall law can be a good approximation for the entire vertical velocity profile in natural streams.

Based on experiments of smooth pipe flow, Nikuradse (1932) determined the von Kármán constant κ and the integral constant A with 0.40 and 5.5, respectively. Different researchers report slightly different values for both constants. An overview can be found in Nezu and Nakagawa (1993). With dimensions, the logarithmic law of the wall in equation (2.5) is often written as (Schlichting, 1979):

$$\frac{U}{U^*} = \frac{1}{\kappa} ln\left(\frac{y}{y_0}\right) \tag{2.6}$$

The distinction between smooth turbulent flow and rough turbulent flow conditions can be expressed by means of the roughness Reynolds number Re_*, defined in equation (2.7), and the equivalent roughness height k_s.

$$Re_* = \frac{U^* k_s}{\nu} \tag{2.7}$$

The roughness Reynolds number increases with turbulence and wall roughness and is related to the zero-point y_0 ($U(y_0) = 0$) of the logarithmic velocity profile in equation (2.6). The two turbulent regimes are then defined as follows:

$$\begin{aligned} y_0 &= \frac{\nu}{9.0U^*} && Re_* < 5 && smooth\ turbulent\ flow \\ y_0 &= \frac{k_s}{30} && Re_* > 70 && rough\ turbulent\ flow \end{aligned} \tag{2.8}$$

It is to note that for transitional flow with Re_* in the range of $5 < Re_* < 70$ no simple relationship exists. An analytical approach for solving transitional flow near the wall is given e.g. in Wu (2008).
In riverine open channel flow the rough turbulent regime prevails usually. Inserting the relation for rough turbulent flow from equation (2.8) into (2.6) yields the well-known law of the wall for rough walls:

$$\frac{U}{U^*} = \frac{1}{\kappa} ln\left(\frac{30y}{k_s}\right) = \frac{1}{\kappa} ln\left(\frac{y}{k_s}\right) + 8.5 \tag{2.9}$$

Finally, it should be mentioned that in numerical models which apply the log-law for boundary layer treatment, the first grid point (or cell center) adjacent to the wall should have the distance y_p to the wall in order to comply with the condition in (2.10). Though, the upper bound depends on the Reynolds number and may have a larger value.

$$30 < y^+ = \frac{y_p U^*}{\nu} < 300 \tag{2.10}$$

2.1.3 Turbulence modelling

The set of RANS equations (2.3) and (2.4) is not closed due to the unknown correlations between fluctuating velocities $\overline{u_i' u_j'}$. To overcome this problem, a strategy in numerical models is the expression of the turbulence correlations on the basis of averaged physical quantities with the help of a turbulence model.

For modelling turbulent stresses, the Boussinesq's eddy viscosity concept is a widely used method. This concept assumes that, in analogy to viscous stresses in laminar flows, the turbulent stresses are proportional to the mean velocity gradients:

$$-\rho\overline{u_i' u_j'} = \rho\nu_t\left(\frac{\partial U_i}{\partial x_j} + \frac{\partial U_j}{\partial x_i}\right) - \frac{2}{3}\rho k\delta_{ij} \tag{2.11}$$

where ν_t is the turbulent viscosity (eddy viscosity), k is the turbulent kinetic energy and δ_{ij} is the Kronecker delta ($\delta_{ij} = 1$ for $i = j$ and $\delta_{ij} = 0$ for $i \neq j$). The turbulent kinetic energy k is a direct measure of the intensity of turbulent fluctuations in the three spatial directions. It is defined as:

$$k = \frac{1}{2}\overline{u_i' u_i'} \tag{2.12}$$

The turbulent viscosity ν_t is not a fluid property but strongly depends on the local state of turbulence and may vary largely in time and space. As seen in equation (2.11), the turbulent viscosity ν_t is a scalar and hence, it is the same for all stress components.
The role of the turbulence model is the determination of the turbulent viscosity ν_t and its spatial as well as time-dependent distribution in a model domain.

The turbulence models can be classified according to the number of equations to be solved for the calculation of the Reynolds Stress term: the zero-equation model which is an algebraic relation, the single equation model which is a combination of an algebraic relation and a transport equation, the two-equation model which consists of a transport and a diffusion equation and more advanced models like the Reynolds stress model. The zero-, one-, or two- equations turbulence models rely on the Boussinesq's assumption in equation (2.11) which implies the hypothesis of isotropic turbulence. Thus, these models aren't able to solve turbulence-driven secondary motion in channels (Prandtl's second kind of secondary motion) for which a Reynolds stress model or a non-isotropic eddy viscosity model would be needed.
In the case of numerical modelling of large water bodies with large aspect ratios between horizontal and vertical mesh resolution, it is common practice to consider the eddy viscosity as anisotropic quantity and to adopt different turbulence models for the horizontal and vertical direction, respectively (Hervouet, 2007).

The following description of some of the several established turbulence models is restricted to the commonly used zero-equation models and two-equation models available in Telemac-3D. The here outlined zero-equation models are the Constant Eddy Viscosity model, the Mixing Length model and a variant of it as well as the Parabolic Eddy Viscosity model. They do not account for changes in local turbulence structure and assume implicitly that the turbulence is dissipated where it is generated (local equilibrium). In contrast, the two-equation k-ε turbulence model describes the transport of turbulent quantities. This model accounts for history effects of turbulence and it can calculate the altered state of turbulence at a point influenced by the turbulence generation somewhere else (Rodi, 1984).

Constant Eddy Viscosity model

The constant eddy viscosity model is not a proper turbulence model but it is often used in numerical models to parametrize the horizontal diffusion including the dispersion, especially in maritime applications but also in fluvial hydraulics. The value of this coefficient has a strong effect on the extent and shape of recirculation. By choosing a low value small eddies will tend to dissipate only, whereas by choosing a high value large recirculations will also tend to dissipate. The user must handle the value of the constant eddy viscosity with care and it should be calibrated by means of field measurements, e.g. dye-spreading experiments or ADCP measurements or by means of physical model tests. As Rodi (1984) states, in some numerical methods the constant eddy viscosity model is merely introduced to generate artificial diffusion in order to improve numerical stability.

Mixing Length model

The Mixing Length model is most commonly used, as in Telemac-3D, to calculate the distribution of eddy viscosities along the vertical. Originally proposed by Prandtl (1925), the model assumes that the eddy viscosity ν_t is proportional to a mean fluctuating velocity and a mixing length l_m. Furthermore, he postulated that the fluctuating velocity is equal to the mean velocity gradient times the mixing length l_m. These hypotheses yield the following equation for the case of a two-dimensional flow:

$$\nu_t = l_m^2 \left|\frac{\partial U}{\partial z}\right| \tag{2.13}$$

where U is the flow velocity at a vertical distance z from the river bed. Extending the Mixing Length model to calculate the vertical eddy viscosity distribution $\nu_{t,z}$ in three-dimensional flow, equation (2.13) becomes:

$$\nu_{t,z} = l_m^2 \sqrt{\left(\frac{\partial U}{\partial z}\right)^2 + \left(\frac{\partial V}{\partial z}\right)^2} \tag{2.14}$$

where U and V are the flow velocity components in the x and y horizontal directions at a vertical distance z from the river bed. For the specification of the mixing length l_m various simple empirical formulae for different situations have been found. For boundary layer flows or open channel flow, l_m can be approximated by a ramp function as given in equation (2.15) (Rodi, 1984). Near the wall or river bed, within the logarithmic layer, l_m increases linearly and in the upper portion a constant value of $l_m/h = 0.2\kappa = 0.08$ has been found to be appropriate. This approach implemented also in Telemac-3D is called the standard Mixing Length model.

$$l_m = \begin{cases} \kappa z & if\ z \leq 0.2h \\ 0.2\kappa h & if\ z > 0.2h \end{cases} \tag{2.15}$$

Nezu and Nakagawa model as variant of the Mixing Length model

Based on the measurements of the vertical mixing length distribution in open channel flow, which indicate smaller values for the mixing length near the free water surface, Nezu and Nakagawa (1993) propose the following relation:

$$l_m = \kappa z \sqrt{1 - \frac{z}{h}} \tag{2.16}$$

The Mixing Length model (2.14) in combination with equation (2.16) is well suitable for river flow calculations where simple shear layer flow prevails and where turbulence is in local equilibrium. Figure 2.1 shows the vertical distribution of the mixing length l_m for the standard Mixing Length model and the Nezu and Nakagawa approach.

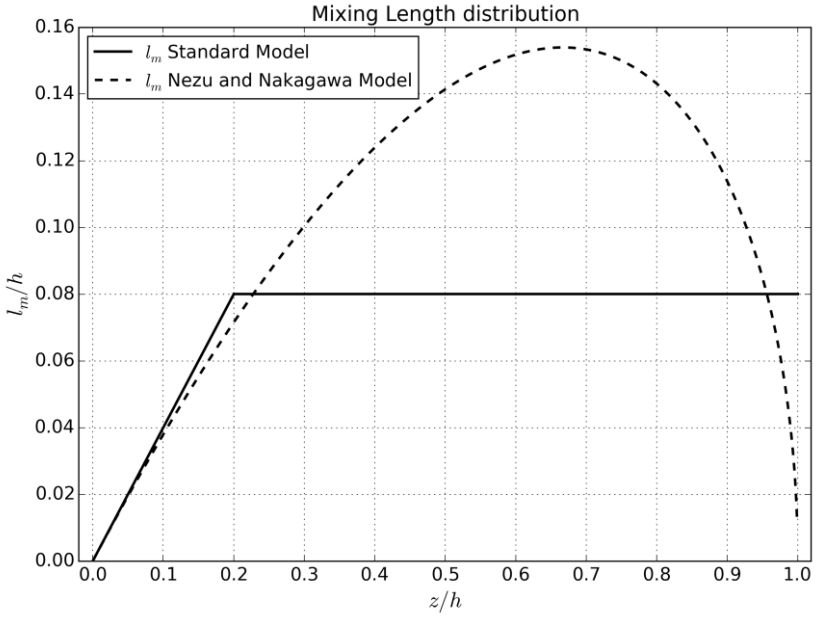

Figure 2.1: Mixing length distribution along the water depth

For maritime applications, where buoyancy and stratification effects can be important and need to be modelled, equation (2.14) must be extended with additional damping functions (Hervouet, 2007).

Parabolic Eddy Viscosity model

The Parabolic Eddy Viscosity model, published by Nezu and Nakagawa (1993) and often used in open channel calculations, can be considered as a special variant of the Mixing Length model. It stems from the fact that in two-dimensional open channel flow the vertical eddy viscosity follows a parabolic distribution along the water depth. The model implies a perfect balance between hydrostatic pressure gradient and vertical shear stress. Assuming a logarithmic velocity distribution along the water depth, the vertical velocity gradient is:

$$\frac{\partial U}{\partial z} = \frac{U^*}{\kappa z} \tag{2.17}$$

Substituting equation (2.17) and equation (2.16) into equation (2.13), the following expression for the vertical eddy viscosity distribution along the water depth is obtained:

$$\nu_{t,z} = \kappa U^* z \left(1 - \frac{z}{h}\right) \tag{2.18}$$

The Mixing Length model or the Parabolic Eddy Viscosity model are well suitable for calculating the turbulent diffusion along the water depth. However, the influence of horizontally generated turbulence on the flow field, e.g. in the vicinity of water works due to significant horizontal velocity gradients, is not taken into account. Such horizontal turbulence effects have to be modelled by means of a horizontal constant eddy viscosity or a horizontal mixing length model.

***k*-*ε* model**

The standard k-ε model is one of the most widely used turbulence models in open channel and internal flow computations because of its universal application range. The two-equation turbulence model solves the two transport equations for the kinetic energy k of the turbulent motion and the dissipation rate ε of the turbulent kinetic energy, respectively. By solving the advection and diffusion of turbulence quantities the model accounts for history effects of turbulence. The turbulent eddy viscosity ν_t is expressed in terms of turbulent kinetic energy k and dissipation rate ε via the Kolmogorov - Prandtl expression (Jones and Launder, 1972):

$$\nu_t = c_\mu \frac{k^2}{\varepsilon} \tag{2.19}$$

where c_μ is an empirical model constant.

The turbulent kinetic energy k and its dissipation rate ε are obtained by solving the following transport equations:

$$\frac{\partial k}{\partial t} + U_i \frac{\partial k}{\partial x_i} = \frac{\partial}{\partial x_i}\left(\frac{\nu_t}{\sigma_k}\frac{\partial k}{\partial x_i}\right) + P_k - \varepsilon \tag{2.20}$$

$$\frac{\partial \varepsilon}{\partial t} + U_i \frac{\partial \varepsilon}{\partial x_i} = \frac{\partial}{\partial x_i}\left(\frac{\nu_t}{\sigma_\varepsilon}\frac{\partial \varepsilon}{\partial x_i}\right) + c_{1\varepsilon}\frac{\varepsilon}{k}P_k - c_{2\varepsilon}\frac{\varepsilon^2}{k} \tag{2.21}$$

where σ_k, σ_ε, $c_{1\varepsilon}$, and $c_{2\varepsilon}$ are empirical constants. Hervouet (2007) also includes a source term in both equations in order to account for gravity forces in the case of temperature gradients. These source terms also are implemented in Telemac-3D. The production of turbulence P_k represents the transfer of kinetic energy from the mean flow to the turbulent motion through the interaction between the turbulent fluctuations and the mean flow velocity gradients. P_k is given by:

$$P_k = \nu_t \frac{\partial U_i}{\partial x_j}\left(\frac{\partial U_i}{\partial x_j} + \frac{\partial U_j}{\partial x_i}\right) \tag{2.22}$$

The five empirical constants used in the two transport equations (2.20) and (2.21) are based on extensive examination of free turbulent flows, but they can also be used for wall flows. The constants have been chosen to make the model compatible with the logarithmic velocity distribution near the wall with the von Kármán constant $\kappa = 0.435$. The values recommended by Launder and Spalding (1974) are:

$$c_\mu = 0.09 \quad c_{1\varepsilon} = 1.44 \quad c_{2\varepsilon} = 1.92 \quad \sigma_k = 1.0 \quad \sigma_\varepsilon = 1.3 \tag{2.23}$$

It can be remarked that Nezu and Nakagawa (1993) argue that if the von Kármán constant is set to $\kappa = 0.41$, as measured in channel flows, $\sigma_k = \sigma_\varepsilon = 1.2$ should be adopted. However, the variation of the constants within this range may alter the simulation results to some extend in detailed small-scale investigations only.

2.1.4 Numerical discretization techniques

Telemac-3D solves the RANS equations (2.3) and (2.4) in the non-conservative form on an unstructured grid, using a semi-implicit time integration. For each point in the grid, the main hydrodynamic results are the water depth, the velocity components and the pressure in the three spatial directions.

The spatial domain is discretized using an unstructured grid composed of prisms. The three-dimensional grid is generated from a two-dimensional unstructured triangle mesh by replicating the horizontal grid over the vertical. The structured grid in the vertical is layered, applying a terrain-following sigma transformation.

The basic solution algorithm is the fractional steps method which consists of three computational steps. First, in the advection step, the transport of the flow velocities (or also turbulent quantities) is computed by only solving the advection terms in the momentum equations. In the second step, from the advected velocities, an intermediate velocity field is calculated, taking into account the diffusion terms and the source terms in the momentum equations. In the case of hydrostatic pressure hypothesis the third step consists of the pressure-continuity step in which the water depth and the vertical velocity component are computed by integrating the continuity and momentum equations along the vertical. In the non-hydrostatic version the pressure P in equation (2.4) is the sum of the hydrostatic pressure and the dynamic pressure. First, by means of the fractional step method the equations are solved assuming a hydrostatic pressure distribution. In an additional step, the so called projection step, the continuity equation is solved by adding the dynamic pressure as a correction term to the hydrostatic pressure in order to provide a zero divergence of velocity (Hervouet, 2007).

For the calculation of the advection terms Telemac-3D offers several different advection schemes: the method of characteristics (MOC), the Streamline-Upwind Petrov-Galerkin scheme (SUPG) and residual distributive schemes such as the Multidimensional Upwind Residual Distribution (MURD) scheme with the Narrow (N) scheme and the Positive Streamwise Invariant (PSI) scheme. In order to ensure an exact mass conservation of the water the advection of the water depth is computed by means of the mass conservative PSI scheme. The diffusion terms and the source terms are computed by means of the Finite Element method. The discretised equations form a linear system which is solved using an iterative solver based on the conjugate gradient method.

2.1.5 Hydraulic boundary conditions

In the three-dimensional modelling of open channel flow three types of boundary conditions have to be considered: solid boundary, liquid boundary and water surface boundary.

At the solid impermeable boundary, which may be the bottom, the bank or an island, usually high velocity gradients appear (no-slip condition). Instead of resolving the velocity profile in the near vicinity of the wall down to the viscous sublayer, Telemac-3D uses the logarithmic wall law. In natural rivers, like the case study presented here, hydraulic rough conditions prevail for which Telemac-3D uses the law of the wall for rough walls in equation (2.9).
When using the k-ε turbulence model the turbulent kinetic energy k_w and its dissipation rate ε_w at the wall nodes are defined as (Rodi, 1984):

$$k_w = \frac{U^{*2}}{\sqrt{c_\mu}} \quad \text{and} \quad \varepsilon_w = \frac{U^{*3}}{\kappa\,\delta} \tag{2.24}$$

where δ is half the distance from the wall node to the adjacent node measured along the normal direction to the wall. The relations in (2.24) assume local equilibrium of turbulence near the wall which means that the production of turbulence is equal to the dissipation.

At the liquid boundaries, depending on the flow regime (subcritical or supercritical), the velocity and / or the water depth have to be specified. In this case study at the inflow boundary the discharge is imposed and a logarithmic velocity profile is assumed. For the water depth a zero-gradient condition is set. The velocity direction at the inflow boundary is normal to the boundary segments, unless otherwise specified. At the outflow boundary a zero gradient boundary condition is used for the velocity and a Dirichlet boundary condition for the water depth.

In the case of the k-ε turbulence model at the inflow boundary the turbulent kinetic energy k and the dissipation rate ε have a Dirichlet condition. By default they are set to constant minimum values with k equal to 1.E-10 J/kg and ε equal to 1.E-16 W/kg. If the zone of interest is located too near to the inflow boundary the problem may appear that the computed flow field including the turbulent quantities is affected by the arbitrarily chosen turbulent quantities and the assumed theoretical logarithmic velocity profile at the inflow boundary.

In this study numerical tests with the modification of the inflow boundary conditions for k and ε have been performed. As Figure 5.32 in section 5.8 demonstrates, the adoption of the wall boundary condition for k in equation (2.24) with the assumption of the linear decrease towards the water surface yields a good agreement with the measured TKE values in the inflow zone. Thus, at the inflow boundary for both the quantities k and ε the relations defined in equation (2.24) for the bottom nodes with a linear decrease towards the water surface have been tried. In the test simulations almost identical flow fields were computed compared to the simulations with the default boundary settings. Nevertheless, for the main investigations in this research the modified version has been used.

At the outflow boundary a zero-gradient boundary condition is used for both the turbulent quantities.

At the free water surface by default Telemac-3D applies a zero gradient boundary condition for the velocity components U, V and W, the pressure P as well as for the turbulent quantities k and ε.

When using the k-ε model an additional, alternative approach more suitable for open channel flow is implemented. The method accounts for turbulence damping at the free surface by using a Dirichlet boundary condition for ε which is in line with experimental observations (Nezu and Nakagawa, 1993). The Dirichlet condition for the dissipation rate ε_{ws} at the water surface, given in equation (2.25), increases the dissipation at the free surface which in turn limits the length scale near the free surface. The increased dissipation reduces the turbulent kinetic energy k at the free surface and thus, also the turbulent eddy viscosity ν_t. In this way

the turbulent eddy viscosity follows more a parabolic profile over the water depth as typically measured in open channel flow and computed in the Mixing Length model of Nezu and Nakagawa, already described before.

$$\varepsilon_{ws} = \frac{{k_w}^{3/2}}{\alpha \cdot h} \tag{2.25}$$

The relation in (2.25) must be seen as tentative condition in which h is the water depth and α is an empirical constant. For the quantity α Rodi (1984) proposes a value of 0.43 whereas Nezu and Nakagawa (1993) recommend a value of 0.18. The latter value by default is used in Telemac-3D. The condition for ε_{ws} at the water surface in (2.25) was tested for the case study. However, compared to the use of a Neumann condition for ε, almost no change in the calculated flow fields could be detected.

2.2 2D depth-averaged numerical modelling with Telemac-2D

2.2.1 Governing equations

The depth-averaged Saint-Venant equations or shallow water equations (SWE) were derived first by Barré de Saint-Venant in 1871. They also can be obtained by depth-averaging the hydrostatic Navier-Stokes equations of motion, assuming that the vertical length scale (water depth h) is small compared to the horizontal length L of the wavelike motion, that means if $h/L \ll 1$ (Hervouet, 2007).

The shallow water assumption implies the following hypotheses:

- The pressure distribution over the flow depth is hydrostatic.
- The vertical velocity component is much smaller than the horizontal components, and can therefore be neglected.
- The horizontal pressure gradients are due to the displacement of the water surface, implying that the horizontal velocity field is constant over the flow depth.

The shallow water equations are non-linear partial differential equations (given here in Cartesian coordinates), namely the continuity equation (2.26) and the momentum equations in both the spatial directions x (2.27) and y (2.28). The continuity equation expresses the conservation of the water mass. The momentum equations represent the balance between the local and convective acceleration, the pressure forces, the turbulent stresses and source terms like the bed resistance.

$$\frac{\partial h}{\partial t} + \frac{\partial Uh}{\partial x} + \frac{\partial Vh}{\partial y} = S_h \tag{2.26}$$

$$\frac{\partial U}{\partial t} + U\frac{\partial U}{\partial x} + V\frac{\partial U}{\partial y} = -g\frac{\partial Z}{\partial x} + S_x + \frac{1}{h\rho}\frac{\partial (hT_{xx})}{\partial x} + \frac{1}{h\rho}\frac{\partial \left(hT_{xy}\right)}{\partial y} \tag{2.27}$$

$$\frac{\partial V}{\partial t} + U\frac{\partial V}{\partial x} + V\frac{\partial V}{\partial y} = -g\frac{\partial Z}{\partial y} + S_y + \frac{1}{h\rho}\frac{\partial \left(hT_{yy}\right)}{\partial y} + \frac{1}{h\rho}\frac{\partial \left(hT_{yx}\right)}{\partial x} \tag{2.28}$$

where t is the time, h is the water depth, U and V are the depth-averaged velocity components in the x and y horizontal directions, respectively, g is the gravity acceleration, Z is the free surface elevation, ρ is the density of fluid and S_h accounts for the source or sink of fluid in the continuity equation. The latter two terms in both the momentum equations account for the turbulent diffusion by means of the depth-averaged Reynolds stresses T_{xx}, T_{xy}, T_{yx} and T_{yy}. S_x and S_y are source terms in the momentum equations in x and y horizontal directions, respectively. In Telemac-2D they represent, amongst others, the bed resistance, the Coriolis force, the influence of the wind, the atmospheric pressure, the spatial variation of density, the drag force due to vegetation or a source or sink of momentum in the domain. By limiting the treatment to riverine applications, only the bed resistance is considered hereafter.

2.2.2 Bed resistance

Every environmental flow is associated with energy losses due to friction, e.g. the bottom friction at the river bed. The computational determination of the energy losses due to bottom friction is based mainly on empirical friction laws. For this reason numerical models have to be calibrated for example against measured water levels or flow velocities by means of the variation of the friction coefficient.

The constraint due to friction of a flow on a flat plane that is parallel to the flow is expressed by the classical quadratic friction law. This law relates the bed shear stress τ_b to the depth-averaged velocity by a quadratic function dependency. The friction law in two dimensions has the two components:

$$\tau_{bx} = -\frac{1}{2}\rho C_f U\sqrt{U^2+V^2} \quad , \quad \tau_{by} = -\frac{1}{2}\rho C_f V\sqrt{U^2+V^2} \tag{2.29}$$

where τ_{bx} and τ_{by} are the bed shear stresses in the x and y directions, respectively, and C_f is the dimensionless quadratic friction coefficient.
By the use of the relationships in (2.29), the forces (source terms) S_x and S_y due to bottom friction in the momentum equations (2.27) and (2.28), respectively, are expressed as follows:

$$S_x = -\frac{1}{2h} C_f U \sqrt{U^2 + V^2} \quad , \quad S_y = -\frac{1}{2h} C_f V \sqrt{U^2 + V^2} \tag{2.30}$$

The dimensionless friction coefficient C_f can be specified by different well known friction laws such as the law of Chezy. This law was established for uniform flow but is commonly applied to all type of flows, with C_h the Chezy coefficient. It is to note that the Chezy coefficient is not constant since it depends not only on the bottom roughness but also on the water depth.

$$C_f = \frac{2g}{{C_h}^2} \tag{2.31}$$

The empirical friction law of Strickler is related to the Chezy law via the Strickler roughness coefficient k_{st} and the hydraulic radius R_h. The law of Strickler was developed under fully rough flow conditions and thus, strictly speaking, it is valid only under such conditions. However, usually environmental flow is rough turbulent flow. Contrary to the law of Chezy, the Strickler coefficient is independent of the water depth and depends on the bottom roughness only. This fact may facilitate the calibration of a numerical model and therefore it may be one reason for the major popularity of the Strickler law in the hydraulic community.
Approximating the hydraulic radius R_h by the water depth h, which in principle is true for wide channels with large width-to-depth ratios only, the relation between the dimensionless friction coefficient C_f and the Strickler law is:

$$C_f = \frac{2g}{h^{1/3}} \frac{1}{k_{st}^2} \quad and \quad C_h = k_{st} R_h^{1/6} \tag{2.32}$$

For completeness the Keulegan relation for rough turbulent flow should be mentioned which is based on the vertical logarithmic profile of velocity. This friction law, implemented in Telemac-2D as well, relates the Nikuradse's equivalent roughness height k_s by use of the log-law for rough walls from equation (2.9) to the dimensionless friction coefficient C_f, as follows:

$$C_f = 2\left[\frac{\kappa}{ln\left(\frac{30}{e}\frac{h}{k_s}\right)}\right]^2 \tag{2.33}$$

2.2.3 2D turbulence models in Telemac-2D

In this section the three turbulence models available in Telemac-2D, applicable in riverine case studies, are described.

By analogy with the explanations in section 2.1.3, the turbulent shear stresses, appearing in the depth-averaged momentum equations (2.27) and (2.28), are determined by the Boussinesq's assumption (Rodi, 1984):

$$T_{xx} = 2\rho\nu_t \frac{\partial U}{\partial x} - \frac{2}{3}\rho k \tag{2.34}$$

$$T_{xy} = T_{yx} = \rho\nu_t \left(\frac{\partial U}{\partial y} + \frac{\partial V}{\partial x}\right) \tag{2.35}$$

$$T_{yy} = 2\rho\nu_t \frac{\partial U}{\partial y} - \frac{2}{3}\rho k \tag{2.36}$$

where ν_t is the depth mean turbulent eddy viscosity and k is the turbulent kinetic energy. If the zero-equation turbulence models are used, which don't account for the transport of turbulent quantities, the last term involving the kinetic energy k in equations (2.34) and (2.36), respectively, is neglected.
It is to note that in the context of 2D depth-averaged turbulence modelling, where only horizontal transport is considered, the depth mean turbulent eddy viscosity ν_t not only models the lateral stress effects that include viscous friction and the Reynolds stresses. It has to account for the dispersive transport due to vertical non-uniformities of the mean flow velocities U and V, too. For illustration, if a depth mean eddy viscosity ν_t is determined from experiments, it is impossible to distinguish between the turbulent and the dispersion contribution (Rodi, 1984).

The Constant Eddy Viscosity model
The use of a mean depth constant eddy viscosity for the whole flow field and constant in time is common engineering practice in 2D depth-averaged hydraulic modelling. Most of the available 2D hydraulic software offer this option as default configuration. It is to note that in 2D the chosen value for the constant viscosity should include dispersion. Eventually it should account also for sub-grid energy losses or energy losses due to not resolved 3D flow properties.

The Elder model
The Elder model can be derived by integrating equation (2.18) from the parabolic eddy viscosity model over the flow depth and averaging the eddy viscosity. The basic assumption of this approach is, that in open channel flow the turbulence is mainly generated by bed

friction in that the depth mean turbulent viscosity is correlated with the shear velocity U^* and the water depth h. This leads in a first step to the depth-averaged parabolic eddy viscosity model with the mean depth turbulent diffusion coefficient ν_t (Socolofsky and Jirka, 2002):

$$\nu_t = \frac{1}{h}\kappa U^* \int_0^h z\left(1-\frac{z}{h}\right)dz = \frac{1}{6}\kappa U^* h = \alpha_t\, U^* h \tag{2.37}$$

Equation (2.37) with the theoretical proportionality constant $\alpha_t = 1/6\,\kappa$ provides reasonable eddy viscosities only in zones where the water depths or the shear velocities are high. The constant $\kappa/6$ is valid only for infinitely wide channels and doesn't account for anisotropic structures of turbulence in horizontal and vertical directions as well as for the transversal or longitudinal dispersion. Therefore, for most of the 2D applications this constant can be considered as too low (Malcherek, 2002). By using the equation above solely, the influence of horizontal shear is ignored, which means that this model doesn't account for horizontal velocity gradients and associated shear zones which emerge e.g. at the region of rigid walls or at abrupt geometrical transitions, e.g. at groyne fields.
Elder (1959) and later Fischer et al. (1979) developed, based on the equation (2.37) and experiments in laboratory channels and natural streams, dispersion equations for the transport of substances in natural streams and determined higher values for the proportionality constant α_t. Fischer et al. (1979) proposed that for transverse turbulent dispersion α_t is about 0.15 in laboratory channels and 0.6 in irregular natural streams with weak meanders. Wu et al. (2004) compared five depth-averaged turbulence models in the simulation of flows around a spur-dyke, in a sudden-expanded flume and in two natural rivers. They applied values for α_t in the range from 0.6 to 1.0. In their numerical models, Vionnet et al. (2004) in turn used values in the range of $\kappa/6$ to 0.3. Jia and Wang (2001) employ in their 2D depth-averaged numerical model the coefficient $\alpha_t = A \cdot \kappa/6$ with A as calibration parameter for which they recommended values in the range of 1 to 10. Steffler and Blackburn (2002) in the depth-averaged numerical model River2D software set α_t to a default value of 0.5 and recommend values from 0.2 to 1.0 as a reasonable range. As it can be seen from these elaborations, the proportionality coefficient α_t has to be considered as a calibration coefficient.

The Elder turbulence model implemented in Telemac-2D is based on the parabolic eddy viscosity model. It adopts the findings by Elder to account for dispersion. In Telemac-2D the dispersion is calculated separately in the longitudinal main stream flow direction and transversal to it. The user manual recommends two different coefficients for the calculation of longitudinal dispersion D_l and transversal dispersion D_t (EDF, 2014). Strictly speaking, both proportionality coefficients should be used as calibration parameters.

$$\begin{aligned} D_l &= 6.0 \cdot U^* h \\ D_t &= 0.6 \cdot U^* h \end{aligned} \tag{2.38}$$

The depth-averaged k-ε turbulence model

Rastogi and Rodi (1978) adapted the 3D standard k-ε model described in section 2.1.3 for the use in depth-averaged calculations. The depth-averaged turbulent eddy viscosity ν_t is calculated based on equation (2.19) by means of the depth-averaged quantities k and ε. The depth-averaging of the transport equations (2.20) and (2.21) yields the following transport equations for the depth-averaged turbulent kinetic energy k and its dissipation ε:

$$\frac{\partial k}{\partial t} + U\frac{\partial k}{\partial x} + V\frac{\partial k}{\partial y} = \frac{\partial}{\partial x}\left(\frac{\nu_t}{\sigma_k}\frac{\partial k}{\partial x}\right) + \frac{\partial}{\partial y}\left(\frac{\nu_t}{\sigma_k}\frac{\partial k}{\partial y}\right) + P_k + P_{kv} - \varepsilon \tag{2.39}$$

$$\frac{\partial \varepsilon}{\partial t} + U\frac{\partial \varepsilon}{\partial x} + V\frac{\partial \varepsilon}{\partial y} = \frac{\partial}{\partial x}\left(\frac{\nu_t}{\sigma_\varepsilon}\frac{\partial \varepsilon}{\partial x}\right) + \frac{\partial}{\partial y}\left(\frac{\nu_t}{\sigma_\varepsilon}\frac{\partial \varepsilon}{\partial y}\right) + c_{1\varepsilon}\frac{\varepsilon}{k}P_k + P_{\varepsilon v} - c_{2\varepsilon}\frac{\varepsilon^2}{k} \tag{2.40}$$

where P_k is the production of the turbulent kinetic energy k due to interactions of turbulent stresses with the horizontal velocity gradients. P_k is calculated as:

$$P_k = \nu_t\left[2\left(\frac{\partial U}{\partial x}\right)^2 + 2\left(\frac{\partial V}{\partial y}\right)^2 + \left(\frac{\partial U}{\partial y} + \frac{\partial V}{\partial x}\right)^2\right] \tag{2.41}$$

In the two transport equations for k and ε, P_{kv} and $P_{\varepsilon v}$ are now additional source terms in order to account for the shear force of flow along the vertical. They represent the production of the turbulent kinetic energy k due to the vertical velocity gradients which mainly develop near the river bed. In this region the turbulent shear stress and the associated production of turbulence energy depends strongly on the bottom roughness. Rastogi and Rodi (1978) related the production terms P_{kv} and $P_{\varepsilon v}$ to the shear velocity U^*. They proposed the following expressions for P_{kv} and $P_{\varepsilon v}$:

$$P_{kv} = c_k\frac{U^{*3}}{h} \quad , \quad P_{\varepsilon v} = c_\varepsilon\frac{U^{*4}}{h^2} \tag{2.42}$$

By use of the quadratic friction law in equation (2.29), the dimensionless quadratic friction coefficient C_f and the relation $U^* = \sqrt{\tau/\rho}$, the shear velocity is expressed as:

$$U^* = \sqrt{\frac{1}{2}C_f(U^2 + V^2)} \tag{2.43}$$

The empirical parameters c_k and c_ε in equations (2.42) are defined as:

$$c_k = \frac{1}{\sqrt{C_f}} \quad , \quad c_\varepsilon = c_{\varepsilon\Gamma} \frac{c_{2\varepsilon}}{C_f^{3/4}} \sqrt{c_\mu} \tag{2.44}$$

The empirical constants c_μ, $c_{1\varepsilon}$, $c_{2\varepsilon}$, σ_k, and σ_ε in the above equations (2.39), (2.40) and (2.44) are the same as in the 3D standard k-ε model and are already given in equation (2.23). The coefficient $c_{\varepsilon\Gamma}$ in equation (2.44) should have value of 3.6 for laboratory scale modelling and a value of 1.8 for field scale modelling. In Telemac-2D the coefficient $c_{\varepsilon\Gamma}$ is calculated as a function of the hard coded Schmidt number (0.5) which yields $c_{\varepsilon\Gamma} = 3.07$.

From a modelling / user point of view it has to be mentioned that the depth-averaged k-ε model doesn't account for the dispersion terms appearing in the depth-averaged momentum equations. For the majority of fluvial and maritime applications the model will compute a too low depth-averaged eddy viscosity ν_t compared to the typically used (or calibrated) eddy viscosity values obtained with the constant Eddy Viscosity model or the Elder model. This means that in order to dissipate larger recirculations, too, the k-ε model generally requires a finer mesh than the zero-equation turbulence models. Hence, the possibly necessary usage of a finer mesh and the solving of the two transport equations increases significantly the computation time.

2.2.4 Numerical discretization techniques

Telemac-2D solves the depth-averaged Saint-Venant equations (2.26), (2.27) and (2.28) in the non-conservative form on an unstructured triangular grid and using a semi-implicit time integration. At each node of the mesh, the program calculates the water depth and the two flow velocity components.

As in Telemac-3D, the basic solution algorithm is the fractional steps method which in the 2D case consists of two computational steps. First, in the advection step, the transport of the flow velocities (or also turbulent quantities) is computed by only solving the advection terms in the momentum equations. In the second step the remaining terms in the momentum equations are considered: propagation, diffusion and source terms. In this stage, the final velocity field is resolved by the finite element technique, using the before calculated advected velocities. The discretised equations form a linear system which is solved using an iterative solver based on the conjugate gradient method. (Hervouet, 2007).

For the calculation of the advection terms several different advection schemes are available in Telemac-2D: the method of characteristics (MOC), the Streamline-Upwind Petrov-Galerkin scheme (SUPG) and residual distributive schemes such as the Multidimensional Upwind Residual Distribution (MURD) scheme with the Narrow (N) scheme and the Positive Streamwise Invariant (PSI) scheme. In order to ensure an exact mass conservation

of the water the advection of the water depth is computed by means of the mass conservative PSI scheme.

2.2.5 Hydraulic boundary conditions

In the two-dimensional modelling of open channel flow two types of boundary conditions have to be considered: solid boundary and liquid boundary.

The solid boundary, which may be a bank or an island, is impermeable which means that no flow crosses a rigid boundary. The boundary condition at the wall may be defined as a fully-slip boundary condition which usually is a suitable choice in the numerical modelling of large domains. With the usage of a no-slip condition for the wall boundary the flow velocity and the shear velocity at the wall are calculated according to the chosen friction law and the chosen turbulent regime (rough or smooth).
When using the depth-averaged k-ε turbulence model, at the solid wall a local equilibrium of production and dissipation of turbulence is assumed, as in the relations in (2.24) for the 3D case. In 2D the production of turbulence due to the bed generated shear should also be considered (Hervouet, 2007). With the assumption of equilibrium of turbulence at the bottom described by the following equation (2.45),

$$P_{kv} - \varepsilon = 0 \quad and \quad P_{\varepsilon v} - c_{2\varepsilon}\frac{\varepsilon^2}{k} = 0 \tag{2.45}$$

the boundary conditions for k_w and ε_w at the side wall are given by:

$$k_w = \frac{\widetilde{U^*}^2}{\sqrt{c_\mu}} + \frac{U^{*2}}{c_{\varepsilon\Gamma}\sqrt{c_\mu}\,C_F^{1/4}} \tag{2.46}$$

$$\varepsilon_w = \frac{\widetilde{U^*}^2}{\kappa\,\delta} + \frac{1}{\sqrt{C_F}}\frac{U^{*3}}{h} \tag{2.47}$$

where $\widetilde{U^*}$ is the shear velocity at the side wall and δ is defined as one-third the distance from the wall node to the adjacent node measured along the normal direction to the side wall.

At the liquid boundaries, like in the 3D case, in the case study at the inflow boundary the discharge is imposed. A zero-gradient condition is set for the water depth. The inflow (velocity) direction at the inflow boundary is normal to the boundary segments. At the outflow boundary a zero gradient boundary condition is used for the velocity and a Dirichlet boundary condition for the water depth.

When using the k-ε turbulence model, at the outflow boundary a zero-gradient boundary condition is used for the turbulent kinetic energy k and the dissipation rate ε. At the inflow boundary both turbulent quantities, by default, have a Dirichlet condition. As already described above, equilibrium is assumed between turbulence production generated by bed shear and its dissipation rate which yields the following relations for k_{in} and ε_{in}:

$$k_{in} = \frac{U^{*2}}{c_{\varepsilon\Gamma}\sqrt{c_\mu}\,C_F^{1/4}} \quad \text{and} \quad \varepsilon_{in} = \frac{1}{\sqrt{C_F}}\frac{U^{*3}}{h} \tag{2.48}$$

2.3 Implementation of the depth-averaged Mixing Length turbulence model in Telemac-2D

2.3.1 Motivation

In flows with high transverse velocity gradients, e.g. flows around structures, expansion and contraction flows with strong recirculation flows, the influence of horizontal velocity gradients on the turbulence production can be significant. In such cases the transverse shear may be the dominant turbulence generation mechanism, compared to e.g. straight river applications, where usually most of the river turbulence is generated by bed friction. Hence, the main idea is to combine the depth-averaged parabolic eddy viscosity model with the Prandtl's mixing length theory for the horizontal in order to account for both vertical and horizontal turbulence production. The resulting depth-averaged Mixing Length turbulence model is a zero-equation turbulence model, which, as per this definition, doesn't account for transport of turbulence.

The main characteristic of the Mixing Length model implemented in Telemac-2D is that it accounts for the physical influence of local horizontal velocity gradients on the turbulent eddy viscosity to be computed. The model yields or tends to the parabolic eddy viscosity model if the horizontal depth-averaged velocity gradients vanish or if the turbulence is mainly produced by bed friction, respectively.

The verification of the numerical model development is an important step, since the implemented model should be free of any flaws in the mathematical formulation and computer programming. Furthermore, the model should predict the basic physical mechanisms and provide numerical solutions within physically plausible thresholds. In section 2.3.3 the proposed turbulence model is verified and validated by means of a laboratory experiment concerning the simulation of flow around a spur-dyke (Rajaratnam and Nwachukwu, 1983). In this process it is not intended to perform a sensitivity analysis by varying some physical and numerical parameters with the objective of matching the experimental results. Additionally to the measurements, the numerical results of the simulation by using the depth-averaged k-ε turbulence model are compared, too.

The laboratory experiment cited above has been used previously by other depth-averaged numerical models as validation or comparative test case, like the Coastal Modeling System CMS (US Army Corps of Engineers, 2011), the CCHED2D model (Jia and Wang, 1999) or the numerical model by Wu et al. (2004).

The paper about the implementation of the depth-averaged Mixing Length turbulence model in Telemac-2D and its validation was presented by the author at the Telemac-Mascaret User conference in 2016 (Dorfmann and Zenz, 2016).

2.3.2 The depth-averaged Mixing Length model

In the depth-averaged Mixing Length model the total turbulent viscosity ν_t is split in a vertical ν_t^V and a horizontal ν_t^H component (Cea et al., 2007):

$$\nu_t = \sqrt{(\nu_t^V)^2 + (\nu_t^H)^2} \tag{2.49}$$

The vertical eddy viscosity ν_t^V is generated by the vertical velocity gradient produced by the bed friction. It is computed by the depth-averaged parabolic eddy viscosity model, already derived in section 2.2.3 (equation (2.37). The semi-empirical coefficient α_t also has been discussed thoroughly in section 2.2.3.

$$\nu_t^V = \alpha_t U^* h \quad with \;\; \alpha_t = \frac{1}{6}\kappa \tag{2.50}$$

The horizontal eddy viscosity ν_t^H is computed according to the Prandtl's mixing length theory by means of the depth-averaged horizontal mixing length l_m and the horizontal mean strain-rate tensor S_{ij}:

$$\nu_t^H = l_m^2\sqrt{2S_{ij}S_{ij}} = l_m^2\sqrt{2(S_{11}^2 + S_{22}^2 + S_{12}^2)} \tag{2.51}$$

The horizontal mean strain-rate tensor S_{ij} is computed by means of the depth-averaged velocity derivatives with (i, j = 1, 2)

$$S_{ij} = \frac{1}{2}\left(\frac{\partial U_i}{\partial x_j} + \frac{\partial U_j}{\partial x_i}\right) \tag{2.52}$$

which yields the horizontal turbulent viscosity due to horizontal shear, written in Cartesian coordinates:

$$\nu_t^H = l_m^2 \sqrt{2\left(\frac{\partial U}{\partial x}\right)^2 + 2\left(\frac{\partial V}{\partial y}\right)^2 + \left(\frac{\partial U}{\partial y} + \frac{\partial V}{\partial x}\right)^2} \tag{2.53}$$

Inserting equation (2.53) and equation (2.50) into equation (2.49) yields the depth-averaged Mixing Length model with the total turbulent viscosity ν_t composed of the bed shear generated term and the transverse shear generated term:

$$\nu_t = \sqrt{(\alpha_t U^* h)^2 + \left(l_m^2 \sqrt{2\left(\frac{\partial U}{\partial x}\right)^2 + 2\left(\frac{\partial V}{\partial y}\right)^2 + \left(\frac{\partial U}{\partial y} + \frac{\partial V}{\partial x}\right)^2}\right)^2} \tag{2.54}$$

The depth-averaged mixing length l_m is calculated by integrating equation (2.16) along the water depth:

$$l_m = \frac{1}{h}\kappa \int_0^h z\sqrt{1 - \frac{z}{h}dz} = \frac{4}{15}\kappa h = C_l h \tag{2.55}$$

In equation (2.55) it is assumed that the mixing length l_m depends on the water depth h which restricts the size of the turbulent eddies. However, the assumption l_m as a function of the water depth can lead to an underestimation of ν_t, since l_m may be larger than the water depth (Cea et al., 2007). The dependency of the mixing length l_m on the water depth may be considered as a weakness of the Mixing Length model. Hence, for the implementation in Telemac-2D the theoretical constant $4/15\,\kappa$ in equation (2.55) has been replaced by a selectable calibration coefficient C_l, with $C_l = 4/15\,\kappa \approx 0.107$ as default value.

The literature research regarding the use of the horizontal Mixing Length model in typical open channel flow simulations and the related choice of the mixing length l_m or the coefficient C_l has not given that many results. Wu et al. (2004) use values for C_l from 0.16 to 0.48. Steffler and Blackburn (2002) recommend a C_l coefficient of 0.1 as a typical value which corresponds to the theoretical coefficient. However, they point out, that depending on the type of flow, the factor C_l may be adjusted. Stansby (2003) validated a three-dimensional numerical model against the experimental data for shallow wakes of a conical island. He proposed a two-mixing-length eddy viscosity turbulence model with a vertical mixing length of classical Prandtl form and a horizontal mixing length. In this study Stansby estimated the vertical mixing length l_v to be equal to $0.09h$ by supposing a boundary layer thickness of $\delta = 0.2h$. He assumed the horizontal mixing length l_h to be a multiple of the vertical mixing

length l_v: $l_h = \beta l_v$. Stansby tested this formulation for the replication of either eddy formations or stable wakes. He reports good predictions when using a multiple of $\beta = 6$ which yields a horizontal mixing length l_m of about half the water depth or $C_l \approx 0.5$. Stansby (2006) reduced the 3D approach to the depth-averaged form and investigated the same case by means of a 2D depth-averaged numerical model. The prediction of stable wakes was poor by using a multiple of $\beta = 6$. However, when vortex shedding was prominent, the 2D and 3D model wake structures were similar. Chini and Stansby (2014) implemented the two-mixing-length eddy viscosity turbulence model into the 3D numerical model Telemac-3D. They tested the model against two datasets. The first case was the flow around a conical island with associated wake patterns. The second case was the tidal flow around a headland. Based on Stansby's findings (2003), again the ratio of 6 between the horizontal mixing length and the vertical mixing length was applied. In both case studies the numerical model Telemac-3D with the two-mixing-length eddy viscosity turbulence model was capable to replicate the experimental results.

Near the wall the damping effect of the wall on the turbulence is important and thus, the relation for the mixing length in equation (2.55) may produce too high turbulent viscosities in the wall region. For the mesh nodes at the wall boundaries, instead of using the water depth as the length scale, the distance from the nodes to wall $dist_{wall}$ should be used. This dimension can also be used for limiting the vertical eddy viscosity computed by the parabolic eddy viscosity model. Cea et al. (2007) suggest the condition given in equation (2.56) for the wall boundary treatment:

$$l_{m,w} = min\left(C_l h,\ \kappa\, dist_{wall}\right) \tag{2.56}$$

In their 2D depth-averaged numerical model, Jia and Wang (1999, 2001) use separate limiters for the calculation of the vertical and horizontal eddy viscosities at the wall boundary nodes. The approach is rational as well as innovative. The method is just based on the equations (2.37) and (2.55) by introducing the relative distance $dist_{wall}/h$ in both equations. The relative distances $dist_{wall}/h$ have the limiting numbers of 0.2113 and 0.3245 which express the locations where the parabolic function and the mixing length are equal to their depth-averaged values, respectively. Equation (2.57) yields the condition for the vertical and equation (2.58) for the horizontal eddy viscosity at the wall boundary nodes.

$$\nu_t^V = \kappa U^* dist_{wall}\left(1 - \frac{dist_{wall}}{h}\right) \quad if \quad \frac{dist_{wall}}{h} < 0.2113 \tag{2.57}$$

$$l_{m,w} = \kappa dist_{wall}\sqrt{1 - \frac{dist_{wall}}{h}} \quad if \quad \frac{dist_{wall}}{h} < 0.3245 \tag{2.58}$$

Both options for the wall treatment of the eddy viscosity, option 1 in equation (2.56) as well as option 2 in equations (2.57) and (2.58), have been implemented and tested in Telemac-2D. The correction is applied for the nodes at the wall boundary with $dist_{wall}$ equal to the normal distance between the closest inner mesh points to the wall. Both approaches have been tested in the validation case presented in the subsequent section 2.3.3 and in the main case study of the thesis. In the two case studies both options compute almost identical turbulent eddy viscosity values at the wall boundary nodes and no significant differences in the resulting spatial velocity distributions emerge. Hence, the simpler method in equation (2.56) has been kept as limiter for the mixing length $l_{m,w}$ at the wall boundary nodes.

2.3.3 Validation

Rajaratnam and Nwachukwu (1983) measured the flow velocities around a spur-dyke in a laboratory flume. The experiment is well suitable for testing the Mixing Length model since in the region of a groyne-like structure significant horizontal flow velocity gradients with possible recirculation flows develop, which in turn have an influence on the turbulence production, the computed turbulent eddy viscosities and the resulting velocity distribution.

The experiments were conducted in a straight tilting rectangular flume with the dimensions: 37 m long, 0.91 m wide and 0.76 m deep. The test reach was located in the downstream half of the flume. 13 different experiments were carried out by varying the length or the shape of the spur-dyke, the water depth or the bed roughness. For the validation conducted here the experimental run A1 is used.

In experimental run A1 the spur-dyke used was made by a 3 mm thin and 0.152 m long aluminium plate projecting perpendicular to the vertical side wall. The flow discharge was 0.0453 m³/s and the approach flow depth was 0.189 m. The flume bed and sides were hydraulically smooth. The flume was inclined to establish uniform flow conditions.

The velocity profiles were measured along four cross sections in the locations $x/b = 2, 4, 6\ and\ 8$, with x starting at the spur-dyke station and b the spur-dyke length (0.152 m). The authors measured the flow velocities at two vertical levels $z/h = 0.03$ and $z/h = 0.85$. In the experiment the reattachment length of the eddy zone downstream of the spur-dyke was found to be approximately $12b$.

Numerical model

The computational domain covers 10 m of the flume length. A horizontal flume bed is assumed. The mesh consists of 8780 nodes and 17020 triangular elements with maximal edge lengths of 0.08 m. In the region of the spur-dyke and in the recirculation zone behind the structure a higher mesh resolution with minimal edge lengths of about 0.015 m is used. The spur-dyke is placed 4 m downstream of the inlet and perpendicular to the right wall. Figure 2.2 shows the computational mesh with the spur dyke.

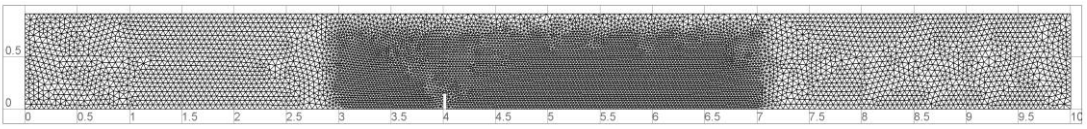

Figure 2.2: Computational mesh with the spur-dyke

Accordingly to the experiment at the upstream inflow boundary a flow discharge of 0.0453 m/³s and for the outflow boundary a constant water depth of 0.189 m are specified. The Strickler roughness coefficient is set to 90 $m^{1/3}/s$ for the whole domain. For the side walls a fully slip condition is applied. As advection scheme for the flow velocity the explicit MURD scheme is used. In the simulation with the k-ε turbulence model the method of characteristics is used for the advective transport of k and ε. In the case of the depth-averaged Mixing Length turbulence model the default values for α_t and C_l equal to 0.0667 and 0.107, respectively, are applied. A simulation time step of 0.02 seconds is used and the simulation is run until steady state flow is reached.

Numerical results

The evaluation of the depth-averaged Mixing Length model is shown in Figure 2.3 by means of the computed turbulent eddy viscosity ν_t. From a verification point of view the new implemented turbulence model doesn't produce any unphysical low or high spikes and the spatial distribution is reasonable. Near the spur-dyke, where higher velocity gradients emerge, the eddy viscosity is accordingly higher than in the surrounding area. Clearly visible is the mode of operation of the limiter for the mixing length l_m in that the eddy viscosity is reduced near the side walls of the flume and the spur-dyke. The comparison with the k-ε turbulence model (Figure 2.4) shows that both turbulence models, in terms of computed eddy viscosities, behave quite differently. The Mixing Length model yields higher turbulent diffusion near the head of the spur dyke, whereas the k-ε model gives much higher eddy viscosity values downstream of the spur dyke.

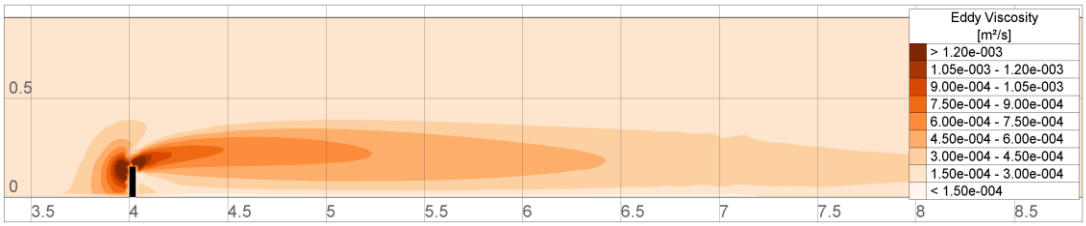

Figure 2.3: Computed turbulent eddy viscosities by the Mixing Length model

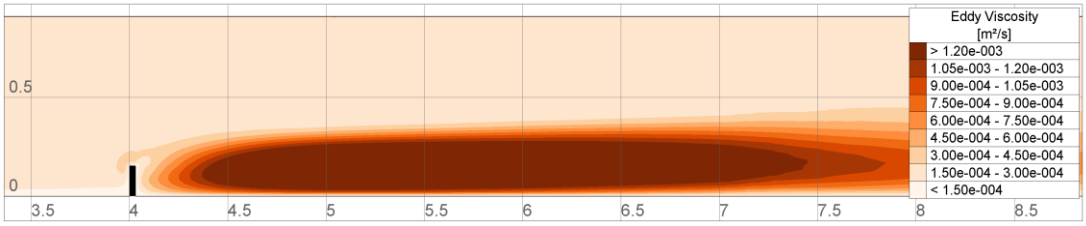

Figure 2.4: Computed turbulent eddy viscosities by the k-ε model

The numerical results in terms of velocity distribution and the locations of the four cross sections are shown in Figure 2.5. Both turbulence models are able to produce the backward-flow region behind the groyne. The Mixing Length model computes a larger recirculation zone downstream of the spur-dyke compared to the k-ε model. In comparison to the measured reattachment length of $x = 12b$ the Mixing Length model (deployed with the standard parameters) slightly overestimates while the k-ε model underestimates the recirculation length. In the other regions upstream and downstream of the spur-dyke both turbulence models produce very similar velocity distributions which confirms also the correct implementation of the depth-averaged Mixing Length model in Telemac-2D.

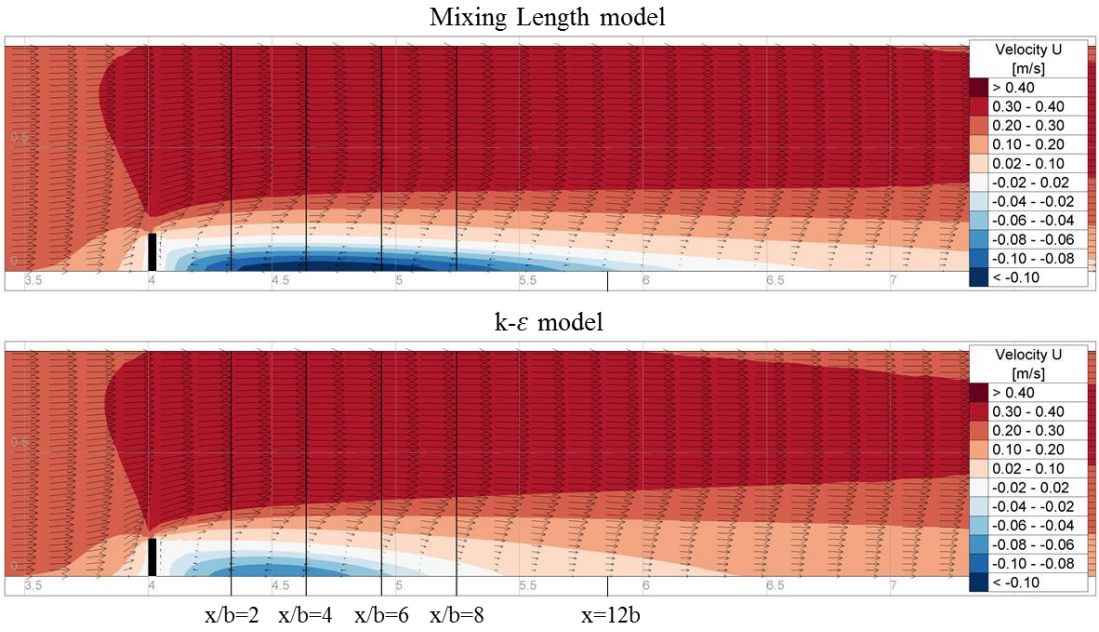

Figure 2.5: Computed flow velocities by the Mixing Length model and the k-ε model

For the comparison of the measured velocity profiles by Rajaratnam and Nwachukwu (1983) with Telemac-2D the data measured at level $z/h = 0.85$ are used. Figure 2.6 shows the measured and the simulated velocities in x-direction at the four cross sections. The measured data reveal significant negative velocities near the wall and the maximum positive velocities arising just outside the shear layer at all the cross sections. In the main flow region the velocity distribution is almost uniform. Compared to the measurements both the turbulence models provide good predictions of the velocity distributions at the four cross sections. The Mixing Length model performs better, especially at the cross sections $x = 6b$ and $x = 8b$, where the k-ε model largely underestimates the magnitude of the negative velocities near the wall. The k-ε model also computes too low flow velocities in the main flow region where the Mixing Length model yields good results. For the quantitative assessment Table 2.1 lists the root-mean-square error (RMSE) between the measured and simulated velocities at the four cross sections. The RMSE values confirm the almost similar performance of both turbulence models at cross section $x = 2b$. With increasing distance from the spur-dyke, at the locations $x = 4b, 6b$ and $8b$ the RMSE values indicate considerably better agreement between the Mixing Length turbulence model and the measurements.

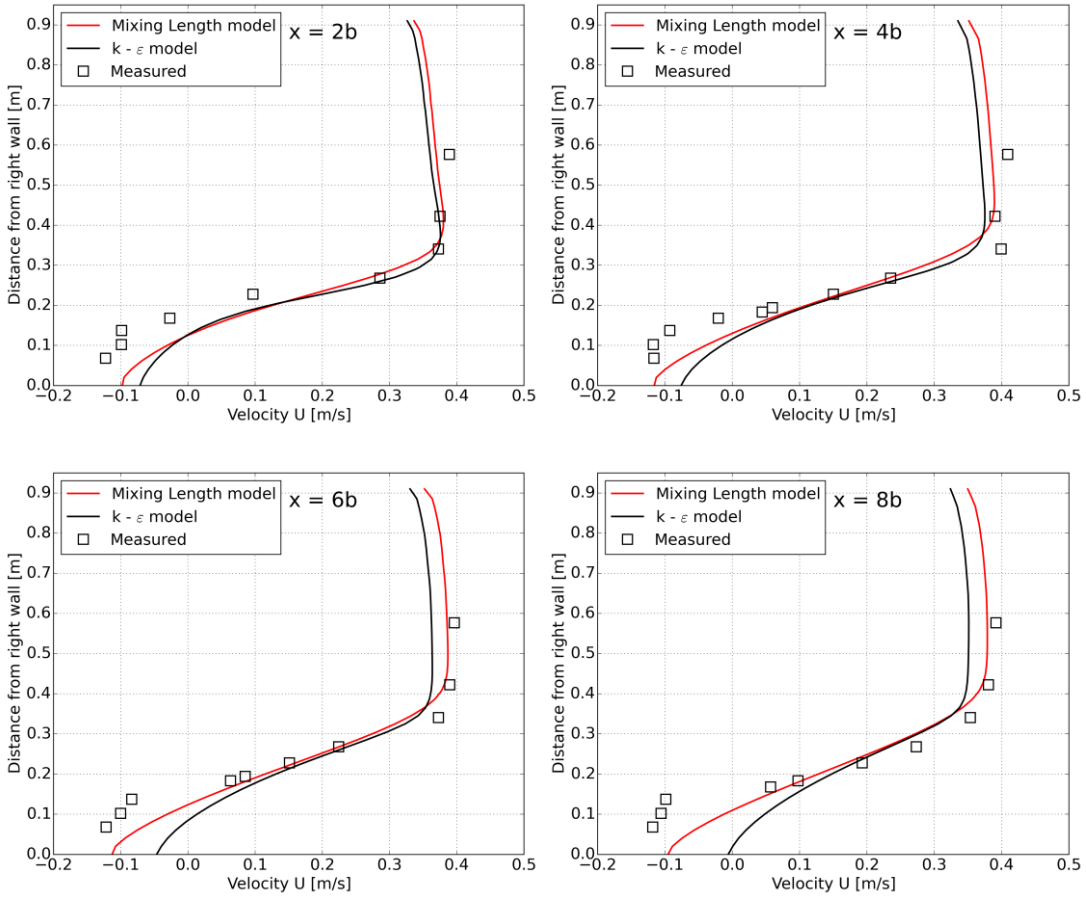

Figure 2.6: Comparison of measured velocities by Rajaratnam and Nwachukwu (1983) and calculated velocities at cross sections $x = 2b, 4b, 6b$ and $8b$

RMSE [m/s] Velocity U **Cross section**	**x = 2b**	**x = 4b**	**x= 6b**	**x = 8b**
***k-ε* model**	0.0687	0.0644	0.0710	0.0929
Mixing Length model	0.0658	0.0539	0.0470	0.0609

Table 2.1: Root-mean-square error (RMSE) values at cross sections $x = 2b, 4b, 6b$ and $8b$

2.3.4 Summary

The main characteristic of the depth-averaged Mixing Length turbulence model implemented in Telemac-2D is, that unlike the constant eddy viscosity or the Elder model, it accounts for the physical influence of the local horizontal velocity gradients on the turbulent eddy viscosity to be computed. The model yields or tends to the parabolic eddy viscosity model if the horizontal depth-averaged velocity gradients vanish or if the turbulence is mainly produced by bed friction, respectively.

The Mixing Length turbulence model is a viable alternative to the already existing zero-equation turbulence models in Telemac-2D, especially in cases in which the transverse shear might be the dominant turbulence generation mechanism. The computations using the Mixing Length model generally are around 20 % faster than with the k-ε model. However, it should be remembered that the Mixing Length turbulence model, unlike the k-ε model,

doesn't account for transport processes of turbulent quantities. In its depth-averaged form the proposed model, like the k-ε model, doesn't account for dispersive transport due to vertical non-uniformities of the mean flow velocities when using the theoretical coefficients for α_t and C_l emerging from the integration. Therefore, depending on the type of flow these semi-empirical coefficients should be considered as tuning coefficients.

The turbulence model has been verified and validated by means of a laboratory experiment concerning the flow around a spur-dyke and by comparison with the two-equation k-ε turbulence model. The validation evidences the correct implementation of the depth-averaged Mixing Length turbulence model in Telemac-2D and its applicability for open channel flow computations.

3 Acoustic Doppler Current Profiler (ADCP) Technique

In open channel flow velocity measurements and water level measurements are of vital importance for the observation and the comprehension of physical hydrodynamic processes. Field measurements play a key role for the calibration of numerical models as well as sometimes of physical laboratory experiments. In numerical models of simple river flow applications it is sufficient to calibrate the friction losses and the roughness values, respectively, by means of water level measurements. However, in the case of complex flow patterns which occur e.g. in expansion flow, in river confluences or diffluences, the measurement of flow velocities is necessary in order to capture and to understand the flow behaviour and furthermore, for the calibration of multidimensional models.

Acoustic Doppler Current Profiler (ADCP) sensors are used to measure flow velocities and discharge in free surface flows by measuring the three-dimensional flow velocities in different water depths. The ADCP technique allows the high-resolution determination of large-scale flow patterns in open channel flow.

The following section introduces the basic principles of the ADCP technique with a special focus on the Teledyne RDI Workhorse Rio Grande ADCP device which was used in the presented research. For further in-depth insights into the ADCP measurement techniques the interested reader is referred to the Teledyne RDI document "Principles of Operation – A Practical Primer" (RDI, 2006a).

3.1 Principles of operation

The ADCP uses ultrasonic sound to measure water velocity. The common frequency range for riverine measurements is between 300 and 3000 kHz (Mueller and Wagner, 2009). Sound consists of pressure waves in air, water or solids. Waves can be classified according to their wavelength which is defined as the distance between successive wave crests and the speed at which waves propagate, namely the speed of sound. The relation between the speed of sound c and the wavelength λ is given by the frequency f in equation (3.1).

$$f = \frac{c}{\lambda} \tag{3.1}$$

The ADCP measures water velocity using a principle of physics discovered by Christian Johann Doppler (1842). An ADCP applies the Doppler principle by reflecting an acoustic signal of small particles of sediment and other material (scatterers) which are present in the water. Doppler's principle relates the change in frequency of a source to the relative

velocities of the source and the observer. The fundamental equation of the Doppler shift can be expressed as follows:

$$f_D = f_S \cdot \frac{v}{c} \tag{3.2}$$

where f_D is the Doppler shift frequency, f_S is the frequency of sound and v is the relative velocity between the sound source and the sound receiver.

A key assumption is that on average the scatterers move at the same horizontal velocity as the water. The velocity measured by the Doppler principle is parallel to the direction of the transducer which emits the signal and receives the backscattered acoustic energy. The ADCP measures the velocity component parallel to the acoustic beams only, which means that the Doppler shift depends on radial motion only (Figure 3.1). In the figure A is the angle between the relative velocity vector and the line between the ADCP beam and the scatterers.

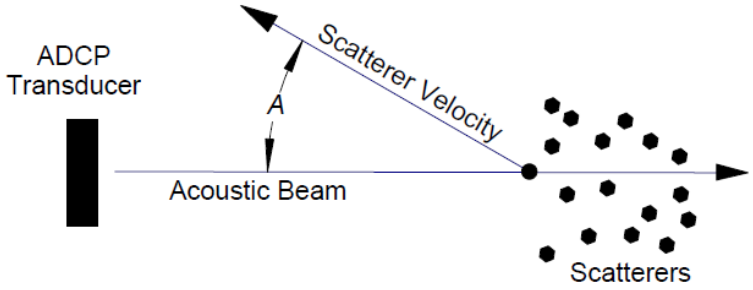

Figure 3.1: Relative velocity vector (source: RDI, 2006a)

When scatterers move away from the ADCP, the sound they hear is Doppler-shifted to a lower frequency proportional to the relative velocity between the ADCP and scatterers. The backscattered sound then appears to the ADCP as if the scatterers were the sound source. The ADCP hears the backscattered sound a second time. Since the ADCP both transmits and receives sound, the Doppler shift is doubled. By limiting the Doppler shift to the radial component only, equation (3.2) becomes (RDI, 2006a):

$$f_D = 2 \cdot f_S \cdot \frac{v}{c} \cdot \cos(A) \tag{3.3}$$

ADCPs have three or four beams arranged in a so called Janus configuration. The beam angle relative to the vertical is between 20 and 30 degrees. The instrument is typically mounted on a boat (downward looking), but can be moored on the river bed (upward looking) or on the river bank (sideways looking). ADCPs require the sensor to be in contact with the water in order to transmit and measure sound pulses directed through the water column. Three beams are required to obtain a three-dimensional velocity measurement. One acoustic beam is required for each current component. As shown in Figure 3.2 the beams

make their measurements in different places. This implies that currents must be uniform (homogeneous) across layers of constant depth, which means they must be the same in all three or four beams. Based on the assumption of horizontal homogeneity, a trigonometric transformation, associated with a Cartesian coordinate system oriented to the instrument, can be used to convert the velocities measured along the beams into the three velocity components. The optional fourth beam obtains an additional vertical velocity. The difference between the two estimates of vertical velocity allows to evaluate the assumption of horizontal homogeneity and hence, data quality.

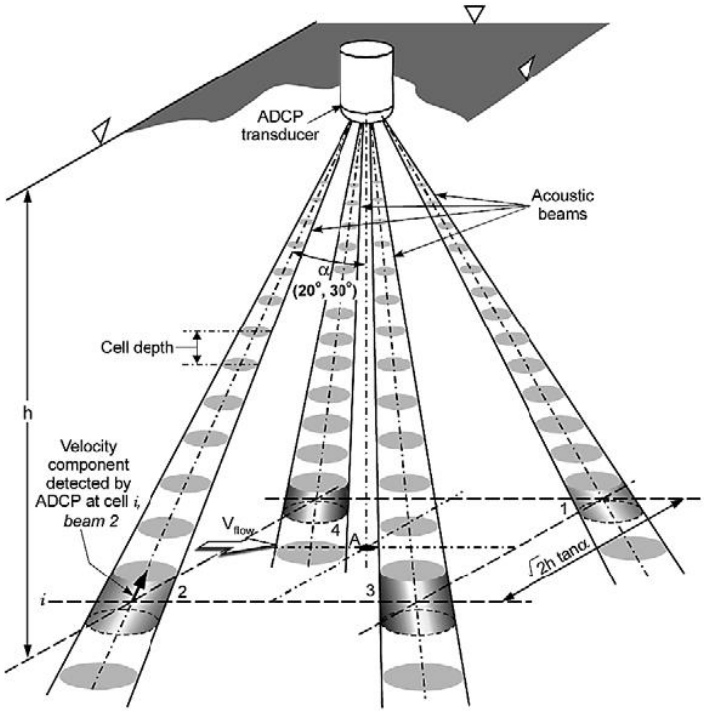

Figure 3.2: ADCP measurement principle (source: Muste et al., 2004)

The most important feature of ADCPs is their ability to measure flow velocities in different water depths simultaneously. The ADCP divides the beam line into equally spaced depth cells (bins). The flow velocities in the different depth cells are recorded by range-gating the echo signal. Range-gating breaks the received signal into successive segments for independent processing. Every segment belongs to a certain time interval (gate) along the timeline. The length of time of the gate is given by the relationship between depth cell size and speed of sound. With reference to Figure 3.3, the transducer sends a transmit pulse which propagates away from the ADCP as the time increases. After the transmit pulse is complete, the ADCP turns off the transducer and waits for a short time, called the blanking period, in which occurring vibrations of the transducer can decay. Afterwards, the ADCP starts the receive mode with the processing of the reflected signals. The reason for the necessary blanking period is the so called ringing effect in which energy from the transmit pulse lingers after the transmit pulse is finished. If there was no ringing, the transducer could receive echoes immediately after transmitting. However, the reflected signals are weak and already a small ringing effect could contaminate the echoes. Consequently, the ADCP must wait for the ringing to cease before it can listen to the echoes and process them. The ADCP

operation is subjected also to interference with unwanted signals near the bottom of the water column. The ADCP velocity measurement data in the first 6 % (for RDI Rio Grande ADCP) water column above the bottom have to be disregarded because they are contaminated by the much stronger echo signal coming from the hard bottom. Generally the size of the 'contaminated velocity' region near the bed depends on the beam geometry and the depth cell size (RDI, 2006a).

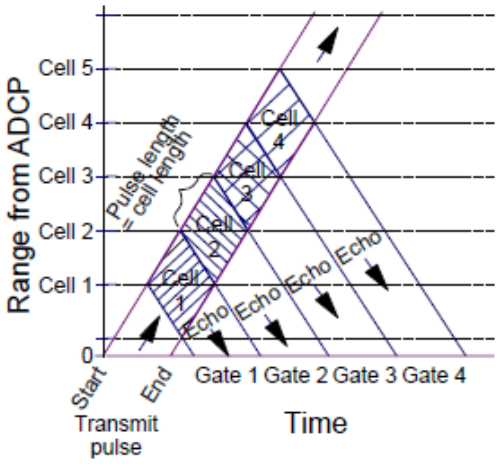

Figure 3.3: Range-time plot (source: RDI, 2006a)

3.1.1 ADCP in moving-vessel deployment

The collection of velocity data with an ADCP sensor along a predefined transect (cross section), operated from a moving vessel, allows the determination of the velocity distribution and further the calculation of the discharge at a cross section. This technique has gained great popularity especially by hydrographic services for the measurement of discharges in riverine environment because of its time-effective and robust determination.

ADCP measures velocities in the water column relative to the boat to which it is attached. Therefore, if the boat moves, its velocity relative to the channel bed needs to be measured to calculate the actual water velocity. The determination of the relative velocity between vessel and river bed is called bottom tracking. While water-profiling uses short transmit pulses to obtain vertical resolution, bottom tracking requires long pulses. Long pulses are used to allow the sound beam to ensonify the bottom over the entire beam all at once, which, associated with usually strong reflections from the river bed, allows the accurate measurement of the ship velocity. The conversion of the ADCP radial (beam) velocities to earth autonomous coordinates is generally accomplished using internal pitch/roll (inclinometers or vertical gyro) and heading (fluxgate compass or gyrocompass) sensors. Via the compass and the bottom tracking signal the ADCP computes the local orientation which implies the determination of the local profile path and its direction. The compass is sensitive to horizontal accelerations as well as far- and near-field environmental conditions, which e.g. could induce local compass errors. Furthermore, the magnetic declination has to be considered especially when measuring at cross sections with large widths.
The water velocity measurement from moving-vessel deployment and by means of the bottom tracking method works only at fixed river bed conditions and if water-mass echoes

are weak relative to the bottom echo (RDI, 2006a). If the river bed is in motion or in conditions with high suspended sediment concentrations the recorded ship velocities are biased which results in the estimation of erroneous water velocities. In such situations the local path of the vessel (ADCP course) has to be determined by means of a Global Positioning System (GPS) sensor.

3.2 ADCP in the research

ADCP flow velocity measurements are valuable source data for the determination and analysis of two- and three-dimensional flow patterns in free surface flows. Furthermore, ADCPs produce a large amount of secondary data by the measurement of echo intensity or temperature data. Dinehart and Burau (2005) show the high potential of the so called flow velocity and echo intensity mapping by the 2D and 3D visualization of measured ADCP data in an entire river reach. Along with such mapping techniques the bottom tracking data can be used for the generation of digital elevation models and their visualization. The study of secondary currents in open channel flow using ADCP measurements is a main topic in the recent literature, e.g. Rhoads et al. (1998). For the analysis of secondary circulation various methods were developed, like the most famous approach by Rozovskii (1954). A good summary and discussion of the different methods can be found in Lane et al. (2000). Rennie et al. (2002) investigated the possibility of measuring the bed load transport velocities using an ADCP under moving river bed conditions. They estimated the bed load transport velocity by calculating the difference between the bottom profile path recorded by the ADCP compass and the profile path measured by an external differential GPS. Single point ADCP measurements were used by Gonzales et al. (1996) to estimate bed shear stress and roughness height by means of the logarithmic wall law. Kim et al. (2000) compared different methods for estimating bed shear stress in an estuary from ADCP data. Carr and Rehmann (2007) and Shen et al. (2010) investigated the calculation of dispersion coefficients from ADCP velocity data. The knowledge of the spatially distributed dispersion coefficients can be valuable for the estimation of the dispersion coefficients in suspended load or tracer transport models as well as for the calibration of the turbulent eddy viscosities in 2D depth-averaged and 3D numerical models. Stacey et al. (1999), Williams and Simpson (2004) and USGS (2006) estimated turbulent quantities such as Reynolds stress and turbulent kinetic energy as well as bed shear stress from ADCP field data. In their research they investigated different procedures for the estimation and removing of instrument noise which is inherent in the velocity data. Nystrom et al. (2007) compared two ADCP devices from different manufacturers with an Acoustic Doppler Velocimeter (ADV) in the estimation of mean velocity and turbulence in a laboratory flume. The technique of using acoustic sensors to estimate suspended solids concentration from acoustic backscatter intensity has gained growing interest over the recent years. In fundamental studies Thorne et al. (1991), Deines (1999) or Gartner (2002) explain the theoretical background and the necessary calibration steps in the estimation of backscatter values from recorded ADCP echo intensity data. The conversion of the recorded echo intensities to normalized backscatter data allows the evaluation of the spatially distributed suspended load concentrations in a cross section by calibrating the backscatter data with in-situ measurements of suspended load concentration. Combined with the ADCP flow velocity data the suspended load flux in a cross section can

be computed. Gartner (2004), for instance, compared estimated suspended solids concentrations from ADCP measurements with an optical backscatter sensor in San Francisco Bay, California. Latosinski et al. (2014) found acceptable differences in the correlation between ADCP backscatter data and suspended load concentration from a depth-integrated sampler in the Parana River (Argentina). Furthermore, they estimated the suspended load fluxes using moving-boat ADCP measurements. Dorfmann et al. (2014) did ADCP velocity measurements and in-situ measurements of suspended load concentrations in the high altitude reservoir Wasserfallboden. Within this project, in his master thesis, Steidl (2014) investigated different methods for the correction of backscatter data, the evaluation of suspended load concentrations and the mass transport of suspended load.

At the Institute of Hydraulic Engineering and Water Resources Management of the Graz University of Technology ADCP field measurements were carried out within various research projects. The projects were related to sediment management in reservoirs of hydro power plants at the river Drau and the river Mur. The ADCP measurements served as basis for decision making based on the analysis of the measured flow fields. Furthermore, the measurements provided the source data for the calibration of 2D and 3D numerical models of the reservoirs Feistritz (Dorfmann et al., 2009) and Edling (Dorfmann et al., 2013a) at the river Drau, of the reservoirs Leoben (Harb et al., 2012) and Fisching (Dorfmann et al., 2012) at the river Mur and, as mentioned above, for the analysis of suspended load fluxes in the high altitude reservoir Wasserfallboden (Dorfmann et al., 2014; Steidl, 2014).

3.3 Development of the postprocessing software ADCPtool

3.3.1 Motivation

Nowadays, the ADCP technique is used by hydrographic services regularly and successfully for measuring discharges in rivers. The manufacturers' data collection and post processing software, like the WinRiver software by RDI (2014), provide different methods for accurate discharge measurements and discharge estimation in unmeasured areas in a cross section.

The analysis of the spatially distributed flow velocities and developing flow patterns in rivers and reservoirs still belongs mainly to research topics as described in section 3.2. An essential reason for this circumstance is the fact that for practical engineering applications the postprocessing of measured ADCP velocity data is a challenging task, like the depth-averaging of velocity data or the detection and filtering of outliers, as Muste et al. (2004) explain. For the in-depth analysis of ADCP data only a few postprocessing software are available, such as the Velocity Mapping Toolbox VMT (Parsons et al., 2013) which is a Matlab-based software and which works only with GPS equipped ADCPs or the free software AdcpXP (Kim et al., 2007).

The author’s project involvements in ADCP measurement campaigns led to the development of the ADCP postprocessing software ADCPtool with the aim to provide specialized and concurrently flexible as well as fast methods to process ADCP measurement data. The program has been released as open source software. The high modular concept of the

software allows the easy implementation of new functions and the adaption of existing parts of code for special requirements. In the ADCPtool some predefined functions for exporting the processed and georeferenced data are provided, e.g. for the freeware software tool for hydraulic modellers BlueKenue™ (CHC, 2011), the open source visualization software Paraview (Henderson, 2007) and for the CAD drawing exchange format dxf, too. Furthermore, every raw or processed measurement data can be connected and exported as ASCII tables via a modular assembled ASCII export function.

The further intention of this software project has been the enhancement of the program's capabilities with the involvement of the interested research community and students as well as the adoption of the software for the use in practical engineering applications. The postprocessing framework ADCPtool has been developed in part within supervised bachelor and master projects and in collaboration with the Verbund Hydro Power company (Austria) who supported the project financially. The first version of the open source software was presented to the international hydraulic community at the 35th IAHR World Congress in Chengdu (Dorfmann et al., 2013b).

3.3.2 Program overview

The ADCPtool has been written in the open source multiplatform programming language Python (Van Rossum, 2013) which allows the ADCPtool to run on any operating system. For facilitating the processing operations the program uses the Python site packages NumPy (Oliphant, 2006) and SciPy (Jones et al., 2001). The site packages provide convenient and fast n-dimensional array manipulation as well as user-friendly and efficient numerical routines. For the purpose of visualization of intermediate results and the continuous control of the processed steps the Python 2D plotting library Matplotlib (Hunter, 2007) is used.
As per February 2017, the ADCPtool supports the RDI Teledyne ADCP devices RDI Rio Grande 600 kHz and 1200 kHz, the RDI StreamPro 2000 kHz and the RDI RiverRay 600 kHz.

3.3.3 Georeferencing methods and projection methods

Generally an ADCP device for moving-vessel deployment is equipped with a compass for the determination of the local orientation. Via the bottom tracking and the compass the ADCP can compute the local profile path and its direction unless moving bed conditions occur. The geo-mapping procedure allows the adding of geographical coordinates to the profile and hence, its georeferencing, if the geographical coordinates of the start or end point of the measured transect are known. For further fine tuning, e.g. to account for magnetic deviation bias or an incorrect calibrated compass, the direction angle of the profile and of the measured flow velocities can be adjusted. In most cases the measured transect path (boat course) doesn’t follow a straight line but has some deviation from the ideal predefined cross section profile. The magnitude of the deviation mainly is related to the existing flow velocities which let the ADCP boat drift away from the predefined cross section profile. In the ADCPtool program three different projection methods are implemented in order to align the measured profile with the ensembles to a user-defined profile. In projection method 1 the

measured ensembles are georeferenced and projected on a user-defined profile according to their relative measured boat distances. This method is set as the standard projection procedure. Projection method 2 doesn't change the boat course but does only a translation by adding geographical coordinates to the locations of the ensembles or cells. In projection method 3 a planar projection of the ensembles on a user-defined profile is performed. Figure 3.4 illustrates some definitions of ADCP related technical terms and the three implemented projection methods.

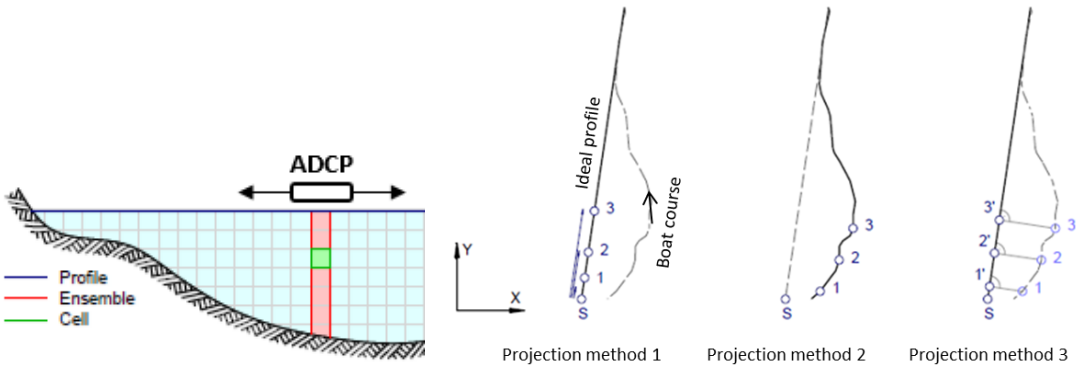

Figure 3.4: left: definition of profile, ensemble and cell at a cross section; right: projection methods in plan view

3.3.4 Detection of outliers and averaging

In many cases the measured flow velocity data in highly turbulent flow or in low flow velocity conditions have some undesirable velocity peaks and random measurement errors. The detection of outliers and the additional averaging of data can be useful to reduce or eliminate such errors. The outlier detection algorithm is based on the analysis of the relative deviation between the measured velocity component u_i in a cell and the computed mean value μ_i comprising the surrounding cells. The procedure combines adjacent cells into a larger grid cell by defining a certain horizontal width r_h and a vertical height r_h of the grid cell. In every grid cell for each velocity component u_i the mean value μ_i and the standard deviation σ_i are calculated. The relative deviation d_i of each velocity component u_i is computed according to equation (3.4). If the deviation d_i is greater than the user-defined limit α, the velocity component u_i in a cell is marked as bad and replaced by the mean value μ_i.

$$d_i = \frac{|u_i - \mu_i|}{\sigma_i} \tag{3.4}$$

The averaging procedure is implemented as moving average processing. The algorithm walks through every velocity component and, depending on the user-defined filter window n for how many ensembles to average, the averaging method smooths the measurement data. The operation of the outlier detection algorithm and the moving average method is illustrated in the following two figures. Figure 3.5 shows raw and processed velocity data in terms of

velocity magnitudes in a cross section. The result from processing of depth-averaged flow velocities is presented in Figure 3.6.

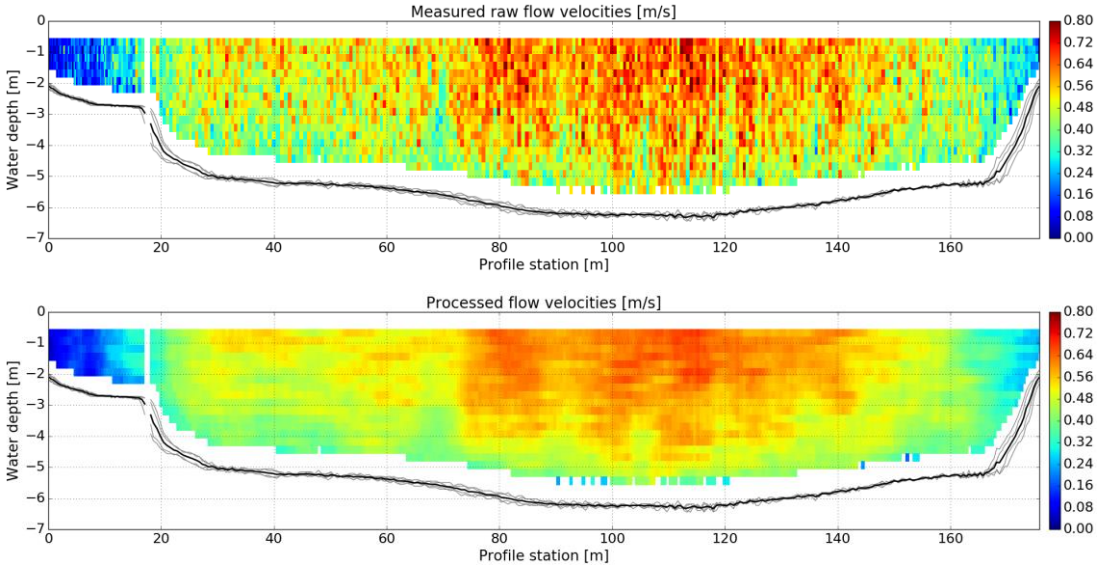

Figure 3.5: up: measured raw flow velocity magnitudes in a cross section; down: processed velocity magnitudes after outliers removal and moving averaging (filter window $n = 11$)

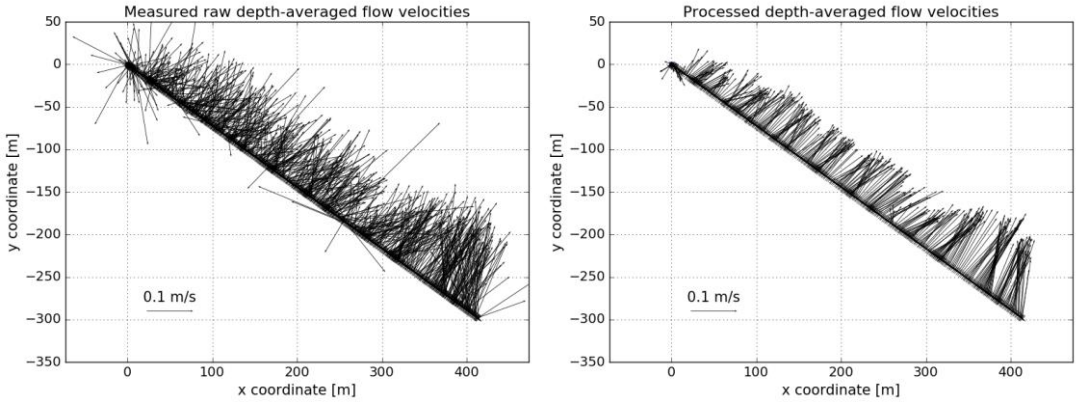

Figure 3.6: left: plan view of measured raw depth-averaged flow velocities at a cross section; right: depth-averaged velocities after outliers removal and moving averaging (filter window $n = 11$)

3.3.5 Estimation of bed shear stress and roughness height

The bottom roughness height and the bed shear stress are important parameters in river hydraulics. The knowledge of those parameters is crucial for planning water works, for the evaluation of the sediment transport processes or for the calibration of numerical models. Up to now, the determination of roughness height and bed shear stress from field measurements is still a difficult task, especially in reservoirs or in general in the backwater of rivers. One way to deduce the bed shear stress and the roughness height is the application of the logarithmic law of the wall for turbulent flows (Chow, 1973):

$$\frac{u(z)}{U^*} = \frac{1}{\kappa} ln \frac{z}{z_0} \tag{3.5}$$

where $u(z)$ is the flow velocity at a distance z above the river bed, z_0 is the height above the river bed where $u = 0$, U^* is the shear velocity and κ is the von Kármán constant equal to 0.40. In rough wall turbulent boundary layers the constant z_0 depends on the roughness height k_s (Schlichting, 1979):

$$z_0 = \frac{1}{30} k_s \tag{3.6}$$

With equations (3.5) and (3.6) and the measured flow velocities in the water column, the unknowns k_s and U^* can be determined by means of the method of least squares. By the linearization of equation (3.5) to $y = ax + b$ and the application of the linear least square method, the shear velocity U^* and the roughness height k_s are calculated as:

$$U^* = \frac{\kappa}{a} \;\; and \;\; k_s = 30e^b \tag{3.7}$$

The bed shear stress τ_b is calculated according to equation (3.8), in which ρ is the density of water.

$$\tau_b = \rho U^{*2} \tag{3.8}$$

The algorithm implemented in the ADCPtool computes the bed shear stress and the roughness height in every ensemble based on the equations (3.5) - (3.8). The Pearson correlation coefficient is calculated as a side product in order to evaluate the linear correlation. The correlation coefficient gives feedback about the quality and suitability of the data for this processing step. The logarithmic layer, and thus the application of the logarithmic wall law, is valid only in the first 20 % water column above the bottom. Strictly speaking, the calculation should be performed with measurement data from this zone only. However, the ADCP velocity data measured in the first 6 % (for RDI Rio Grande ADCP) water column above the bottom must be disregarded, as explained in section 3.1. Depending also on the selected depth cell size and flow conditions the algorithm possibly wouldn't find any or too few valid cells in the logarithmic layer. For this reason a procedure was implemented so that the user can vary the normalized distance from bottom to water surface where the logarithmic wall law can be applied. For illustration purposes Figure 3.7 demonstrates the application of the log-law and the method of linear least squares for ADCP

velocity data. In this example in the layer between 6 % and 20 % of the water depth only four data points are available for the linear regression analysis, which should be critically reviewed. The analysis with the velocity data from the whole water column yields a similar regression line in this case.

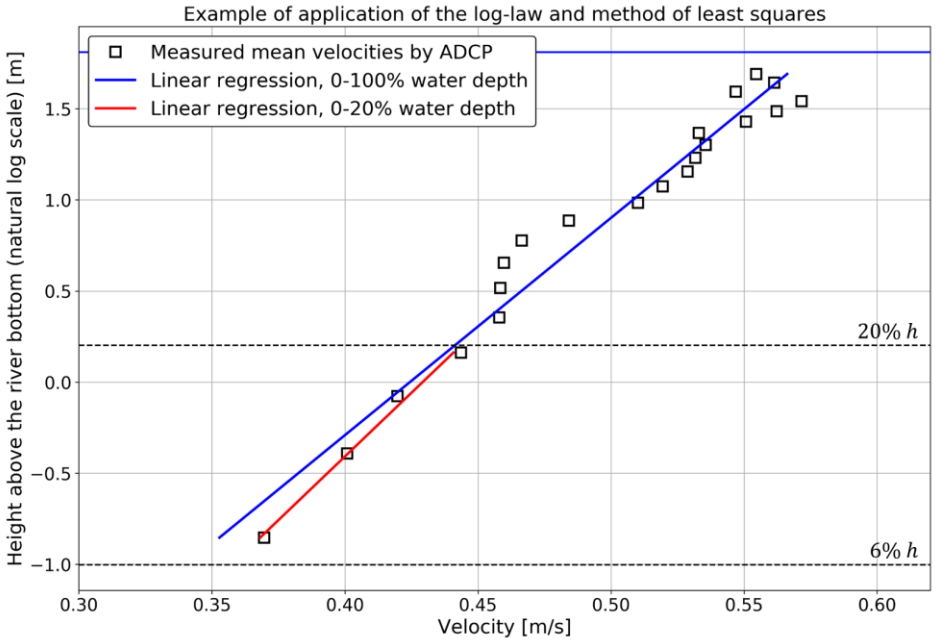

Figure 3.7: Example of application of the log-law and the method of linear least squares

The calculation of bed shear stresses and roughness heights at a cross section from measurement data obtained in moving-vessel deployment should be performed with caution. In moving-vessel measurements the recorded flow velocities in the ensembles could severely scatter and a prior velocity averaging should be carried out. The computed value for roughness height obeys an exponential function which implies that small differences in the calculated regression coefficients could generate big variations in the estimated roughness heights between the different ensembles. Depending on the soil composition of the river bed, the estimated roughness height also may contain the contribution of form roughness due to bed forms. Thus, the computed roughness height shouldn't be used uncritically for the determination of the local prevailing grain size. Figure 3.8 shows example results from moving-vessel ADCP measurement data. The calculated roughness heights k_s differ significantly at this cross section, whereas the bed shear stresses are in a reasonable range.

For the main research in this thesis some initial attempts at estimating the distribution of bed shear stresses and roughness heights along cross sections by means of ADCP data from moving-boat deployment were not successful. Despite several tests, e.g. by trying different methods for averaging ADCP data, the logarithmic wall law couldn't be adopted for obtaining physically reasonable results. The main reasons are the very low flow velocities in the reservoir and the related distinct scattering of the measured velocities along the water depth and across the ensembles.

In section 5.8, based on the implementations explained above, the estimation of bed shear stresses and roughness heights by means of stationary ADCP measurements is presented and discussed.

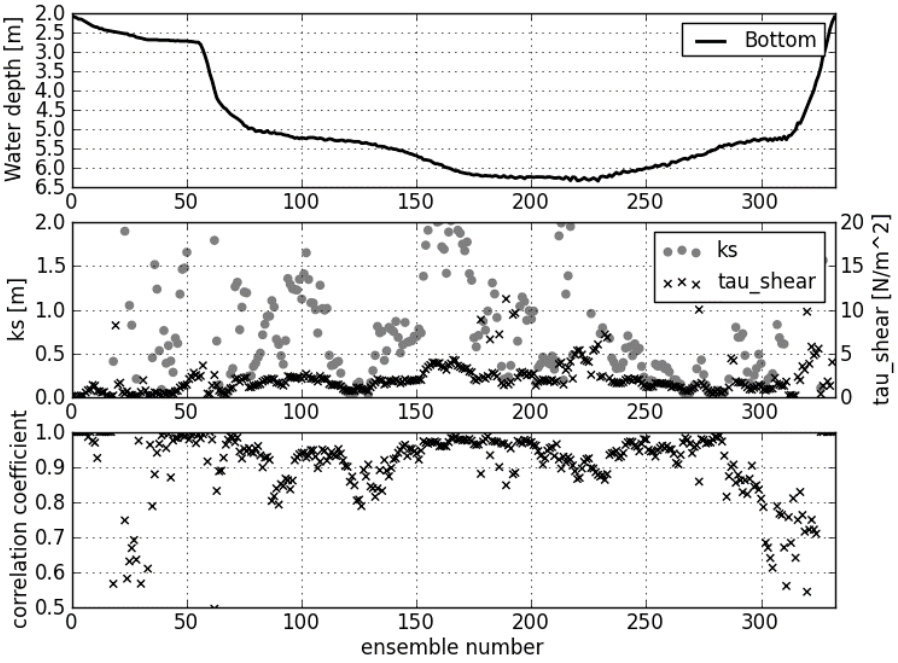

Figure 3.8: Example of estimation of bed shear stresses and roughness heights at a cross section

4 Physical Model Experiments

In this chapter the physical model experiments on the flow behaviour in a reservoir of a run-of-river hydro power plant are presented. The physical model of the case study and the implementation of the experimental results in the prototype have been the basis for the research presented in this thesis.

The physical model study was carried out at the Institute of Hydraulic Engineering and Water Resources Management of the Graz University of Technology within the research project "Sediment management of the reservoir of the hydro power plant (HPP) Feistritz - Ludmannsdorf". The project was funded by the Verbund Hydro Power company.

Purpose of the physical model experiments was the analysis of the developing hydrodynamic flow conditions in the reservoir. The experiments aimed at developing the design of one or more training structures and identifying their optimal positioning, with the objectives to reduce the reservoir sedimentation and to increase the flushing efficiency in the study area. In the physical model study a solution was found by the installation of a non-submerged groyne. Accordingly, the groyne was implemented in the prototype.

4.1 Case study reservoir HPP Feistritz

The run-of-river hydro power plant (HPP) Feistritz-Ludmannsdorf is part of a chain of ten hydro power plants at the river Drau (province Carinthia, Austria). The construction in 1968 and the associated impoundment created a 15 km long reservoir with water depths of up to 22 m. The annual sediment transport of the middle reach of the river Drau amounts to approximately 10^6 m³, 90 % of which are deposited in the reservoir of the HPP Feistritz. Echo sounding measurements of the bottom have revealed the formation of extensive areas of deposition. As a counter measure, every year dredgings of about 150000 m³ have been carried out in the reservoir.
For an introductory overview, Table 4.1 lists the key data of the hydro power plant. Figure 4.1 shows an aerial photo of the hydro power plant and the upstream part of the reservoir.

Commissioning	1968
Turbines: number and type	Two Kaplan turbines
Type of spillway	Stop log weir with sector gates and gate flaps
Number of weir fields	Three with width of 15 m, respectively
Bottleneck capacity / Annual energy output	88 MW / 354 GWh
Design capacity Q_A	440 m³/s
Normal operating water level / Gross head	461.5 m a.s.l. / 23.5 m

Table 4.1: Technical specification of the HPP Feistritz-Ludmannsdorf (Verbund VHP, 2007)

Figure 4.1: Aerial photograph of the reservoir HPP Feistritz (Verbund VHP, 2007)

4.1.1 Study site

In the physical model the study area of the reservoir extended to approximately 3150 m upstream of the hydro power plant. At the upstream boundary the area is marked by an approximately 170 m wide gorge portion. Downstream of the gorge portion, over a distance of around 1500 m the reservoir expands gradually and nearly symmetrically to a 900 m wide area. At both sides the expansion angle has an average value of about 15° deg. The wider area has a length of about 700 m. Downstream of the wider area, within a distance of 400 m, the reservoir contracts to a cross section width of around 470 m. From there, the reservoir within a distance of around 550 m contracts gradually to the hydro power plant. Figure 4.2 shows the reservoir Feistritz with the delineation of the here investigated study area. It outlines also the dimensional difference between the impounded reservoir and the original bed of the river Drau which took course at the orographic right river bank in the study area. The plan view in Figure 4.3 depicts in detail the above described geometric characteristics of the study area.

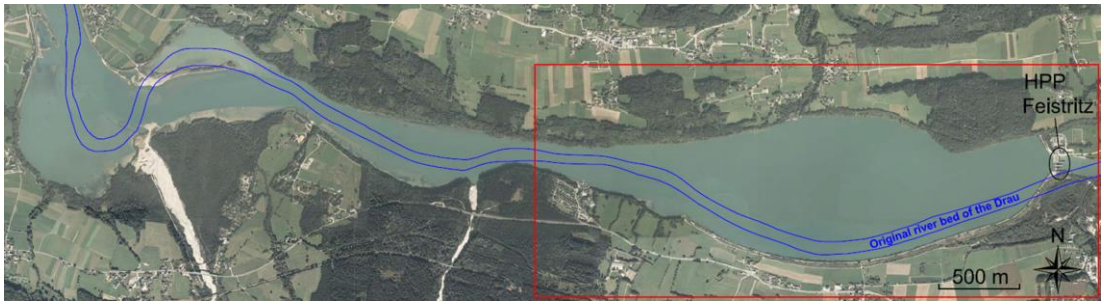

Figure 4.2: Plan view of the reservoir Feistritz with delineation of the study area (red)

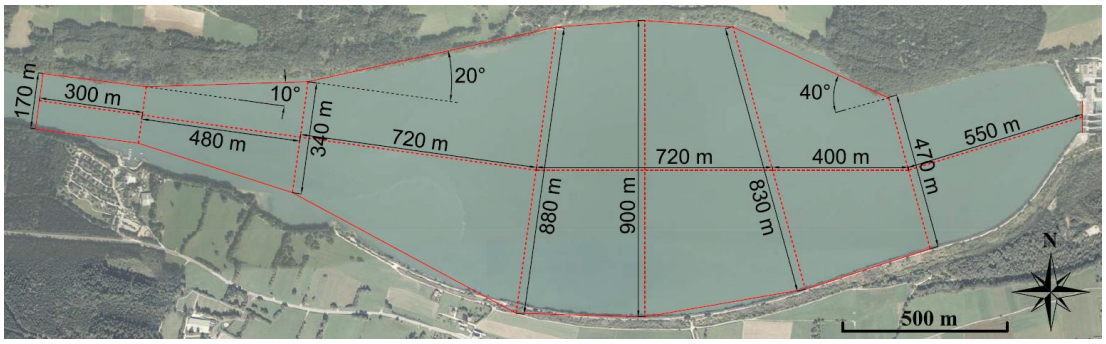

Figure 4.3: Plan view of the study area with geometric dimensions

4.1.2 Bathymetry and sedimentation data

In 2007 echo sounding measurements were carried out in the study area. The surveys provided the basis for the construction of the elevation model in the physical model as well as in the numerical models. The average distance between the measured cross sections was approximately 150 m. Figure 4.4 shows the generated digital elevation model and the location of the surveyed cross sections.

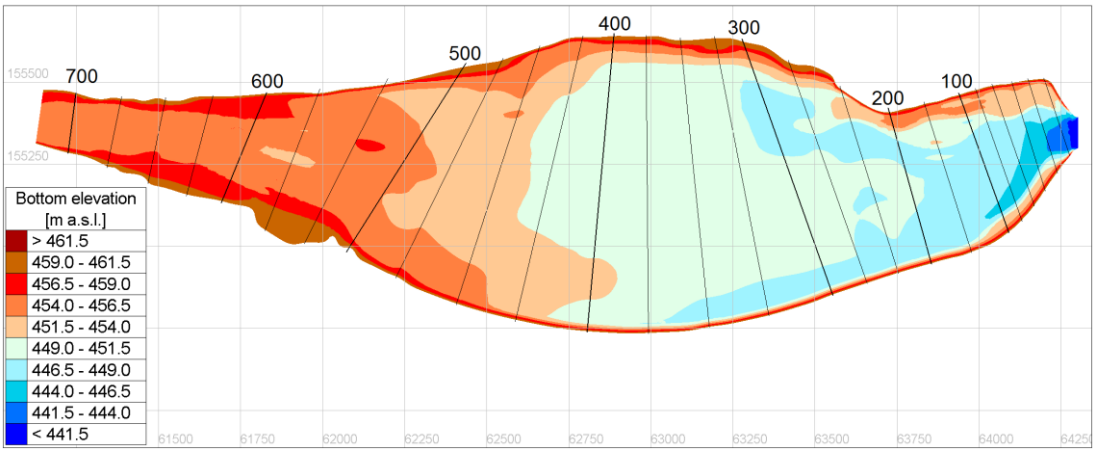

Figure 4.4: Plan view of the digital elevation model 2007 and the cross sections

The sedimentation behaviour in the area of interest has been analysed by the comparison of the bed levels from the initial state (1968) and from 2007. Figure 4.5 demonstrates, by means of the cross sections 300 and 500, the disordered sedimentation behaviour. The sediment is deposited almost homogeneously in the crosswise direction. In the plan view (Figure 4.6), which shows the bed level differences between the initial state and 2007, the original river bed of the Drau is clearly visible. In the period from 1968 to 2007 the original bed has undergone complete aggradation with sedimentation heights of up to 15 m. The average sedimentation height is around 5.0 m. The accumulated sedimentation volume amounts to approximately $12 \cdot 10^6$ m³ which yields an annual sedimentation rate of about $3 \cdot 10^5$ m³ in the study area.

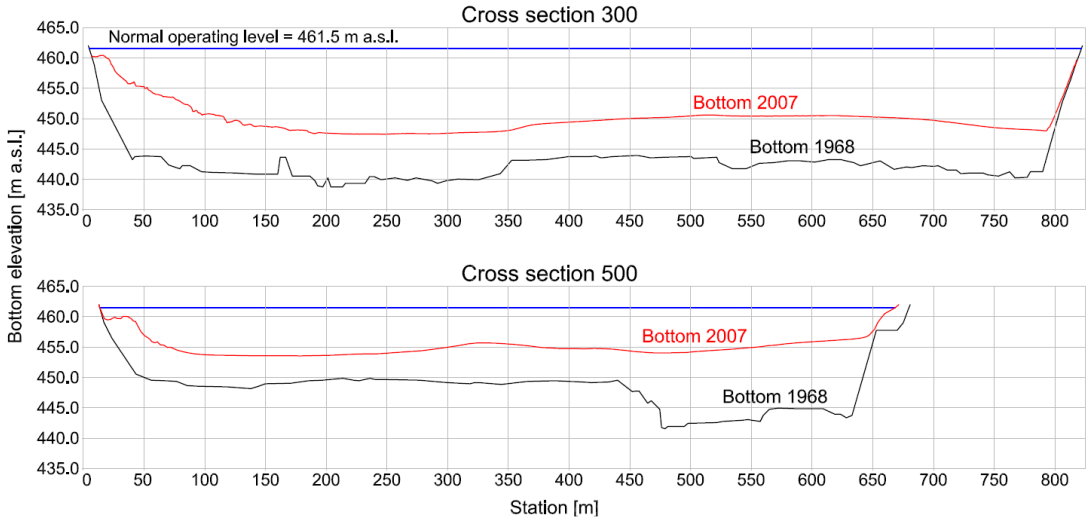

Figure 4.5: Bed levels at the cross sections 300 and 500, initial state (1968) and 2007

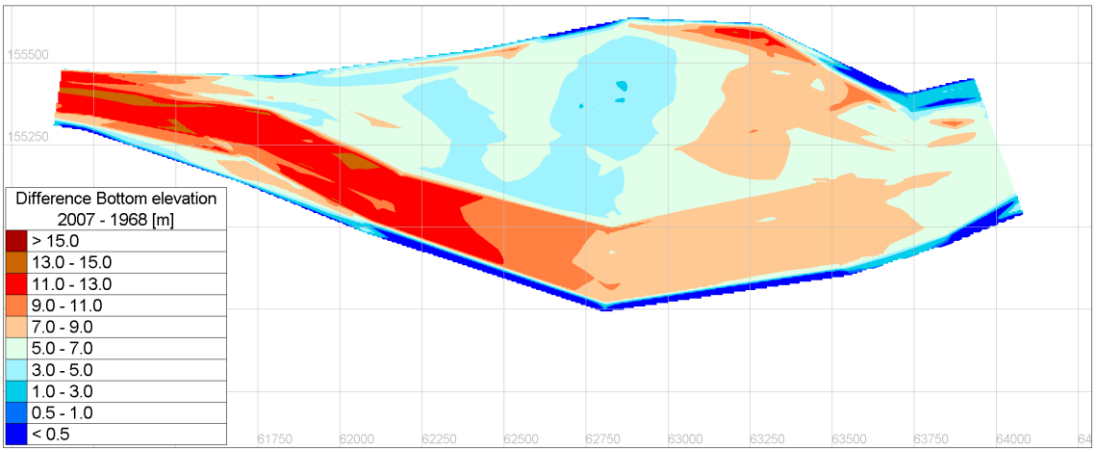

Figure 4.6: Plan view of the bed level differences, 2007 - 1968

The grain size distributions measured in 2005 in the study area demonstrate the typical graded sedimentation processes occurring in reservoirs of run-of-river hydro power plants (Figure 4.7). At the first three cross section upstream of the weir (CS 100 - 300) the sediment is mainly cohesive with the mean grain diameters d_{50} having values between 0.02 mm (medium silt) and 0.1 mm (very fine sand). At the upper cross sections d_{50} varies between 0.15 mm (fine sand) and 0.25 mm (medium sand).

Besides the difficult hydrodynamic setup of the case study, the high uncertainty in the scaling of such very fine grain size distributions was the main reason for not including the sediment transport modelling in the physical model study.

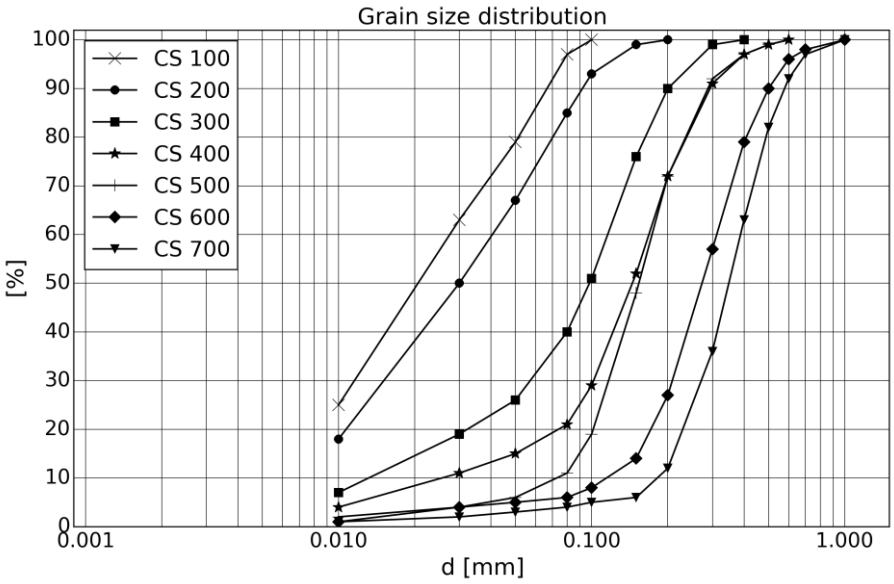

Figure 4.7: Measured grain size distributions at the cross sections (CS) 100 - 700

4.2 Hydraulic load cases

In the physical model experiments two for the hydro power plant characteristic hydraulic load cases have been investigated for the status quo and the variant with the installation of the non-submerged groyne, respectively.

The hydraulic load case LC 1 represents turbine operation with the discharge equal to the design capacity and the water level at the weir corresponding to the normal operating level. LC 1 should characterize the regular normal turbine operation. The second load case LC 2 simulates a smaller flood event by replicating a reservoir flushing scenario for the purpose of reservoir desedimentation. In the flushing scenario the flood discharge is 700 m³/s which corresponds to 70 % of a·1-year-flood and the water level at the weir is lowered by 2.5 m.

In the zone of the upstream boundary during normal turbine operation the average flow velocity amounts to 0.45 m/s and the corresponding Froude number is in the range of 0.06. In the flushing case the higher discharge in combination with the lowered water level considerably increases the inflow velocity to 1.15 m/s and correspondingly the inflow Froude number to 0.20 (Table 4.2). In both load cases the inflow velocity and the inflow Froude number represent the largest values emerging in the whole study area.

Hydraulic load case	**LC 1**	**LC 2**
Discharge [m³/s]	440	700
Water level [m a.s.l.]	461.5	459.0
Mean inflow velocity v_{in} [m/s]	0.45	1.15
Mean inflow Froude number [-]	0.06	0.20

Table 4.2: The two hydraulic load cases operated in the physical model

4.3 Definition of the physical model scale

The geometrical horizontal scale of the physical model was set a priori to 1:100 because of the considerable size of the study area and the space availability in the laboratory. For the vertical scale a lower scale factor was selected based on the subsequent explanations.

In physical model studies dealing with free surface flows generally the Froude similarity law is adopted. This law states that the ratio between inertia forces and gravity forces has to be equal in the physical model and the prototype. The application of the Froude similarity law implies that the discrepancy between the ratio of inertia forces and viscous forces in the prototype and in the model has to be disregarded. This assumption can be safely made if both the flows in the prototype and the physical model are fully turbulent, that means the Reynolds number in the prototype and the scaled Reynolds number in the model are well above the critical Reynolds number of approximately a value of 500 (Kobus, 1984). If this criterion is not fulfilled, then either the horizontal scale factor or the vertical scale factor has to be lowered. The latter option leads to a distorted physical model with unequal horizontal and vertical scale factors.

The Froude similarity law can be deduced by equalizing the Froude numbers of the prototype Fr_{prot} and the physical model Fr_{mod}:

$$Fr_{prot} = \frac{v_{proto}}{\sqrt{g \cdot h_{proto}}} = Fr_{mod} = \frac{v_{mod}}{\sqrt{g \cdot h_{mod} \cdot n}} \tag{4.1}$$

where v is the flow velocity, g is the gravity (=9.81 m/s²), h is the water depth and n is the vertical distortion factor. The subscripts $prot$ and mod represent prototype and model values, respectively.

The preliminary analysis of the Reynolds numbers emerging in the physical model by assuming a scale factor of 100 for both the horizontal and vertical lengths partially has revealed very low values. In zones with low flow velocities the Reynolds numbers would recede to values less than the critical number of 500 which indicates laminar flow. Consequently, the distorted scaling has been applied by defining the vertical distortion factor n = 4 which yields a vertical scale of 1:25. The vertical exaggeration has some positive side effects especially for the here presented case, namely the better measurement handling because of the higher water depths and the improved measurement accuracy due to the higher flow velocities.
The higher side walls in the distorted model reduce the ratio between river width and water depth and may induce artificial three-dimensional flow effects. Kobus (1984) gives the criterion that the factor n should be less than one-tenth of the ratio between river width and water depth in order to prevent these artificial effects. In the present case with an average reservoir width of 400 m and an average water depth of 9.0 m (based on the normal operating water level) this criteria is fulfilled sufficiently.

By the use of equation (4.1), the horizontal scale factor $L_R = 100$ and the vertical distortion factor n = 4, the following hydrodynamic related conversion factors can be deduced:

- Flow velocity: $(L_R / n)^{1/2}$ = 5
- Flow time: $(L_R \cdot n)^{1/2}$ = 20
- Reynolds number: $(L_R / n)^{3/2}$ = 125
- Discharge: $L_R^{5/2} / n^{3/2}$ = 12500

Table 4.3 lists the most characteristic geometrical and hydraulic parameters of the physical model test. For comparison reasons the values for a non-distorted model are shown as well.

	Prototype	**Model Scale 1:100**	**Model Scale 1:100 / 1:25**
Length [m]	3500	35.0	**35.0**
Width max [m]	1000	10.0	**10.0**
LC 1: Q [m³/s]	440	0.0044	**0.035**
LC 2: Q [m³/s]	700	0.007	**0.056**
Inflow velocity v_{in} [m/s]	0.45 / 1.15	0.045 / 0.115	**0.09 / 0.23**
Water depth mean [m]	9.0 / 6.5	0.09 / 0.065	**0.36 / 0.26**
Water depth max [m]	22.0	0.22	**0.88**

Table 4.3: Prototype and model values

4.4 Design of the model

4.4.1 Location and definition of the hydraulic boundaries

Inlet boundary

The gorge portion located 3150 m upstream of the weir (cross section 700) was defined as upstream hydraulic boundary. From the ADCP data at cross section 700 (first measurement campaign, section 5.2) a mean inflow angle was determined. Since the inflow angle is not perpendicular to cross section 700, an additional cross section 700' perpendicular to the inflow direction was defined between cross section 700 and the inflow basin. Furthermore, the shape of the basin was aligned to the measured mean inflow angle. The discharge coming from the pumps was measured by means of an electromagnetic flow meter.

Outlet boundary

The location of the downstream hydraulic boundary was defined at the location of the weir and the turbines, respectively. The distorted model doesn't allow the accurate geometrical downscaling of the gates and the turbine outlet. The overflow flap gates, the radial sluice gates as well as the turbine outlets were modelled as vertical movable gates. Of course such simplified modelling triggers considerable deviations e.g. in the weir coefficients with the effect of producing false weir capacities. For this investigation these modifications were not of vital importance since the flow behaviour in the zone of interest, sufficiently away upstream of the outlet, is not influenced by the type of gates. The water level at the outlet was regulated by acrylic glass orifices in which the openings were adjusted according to the selected discharge.

4.4.2 Installation of the river bed and the non-submerged groyne

The river bed was constructed according to the cross section bottom recordings from 2007. Figure 4.8 shows the general layout of the physical model, the used cross sections for building the river bed geometry as well as the location of the tested 70 m long non-submerged groyne at cross section 600 at the orographic right bank. The shape and location of the groyne was identified based on extensive preliminary model experiments.
The physical model during the construction phase is illustrated in Figure 4.9.

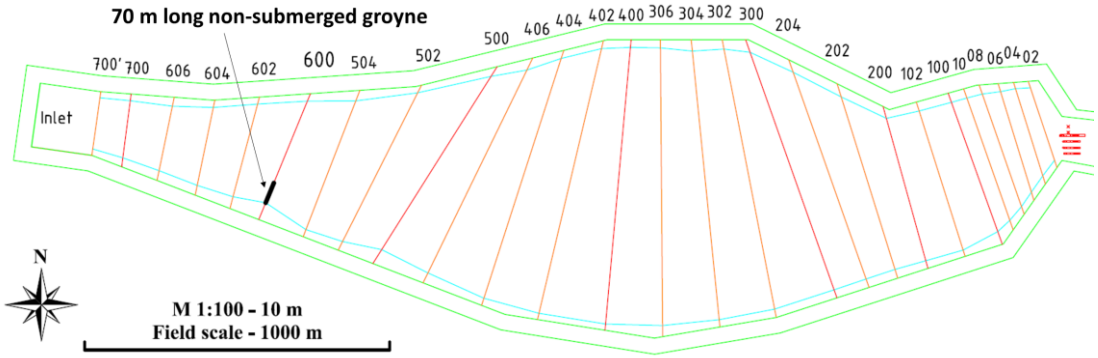

Figure 4.8: Plan view of the physical model

Figure 4.9: Photograph of the physical model under construction in the laboratory

For the bottom filling conventional sand material was used. The bottom surface was made of a thin concrete layer with the help of synthetic mat reinforcements in order to avoid possible bottom breaches due to the large model width and the high water loads (Figure 4.10, left). The outlet zone including the weirs and turbines was constructed based on implementation plans using concrete, plastic material and acrylic glass (Figure 4.10, right).

The tested non-submerged groyne at cross section 600 consisted of a 70 cm long simple wooden board which was tailored based on the shape of cross section 600 and the local bed levels (Figure 4.11).

Figure 4.10: Physical model; left: installation of the river bed; right: detail view of the model outlet

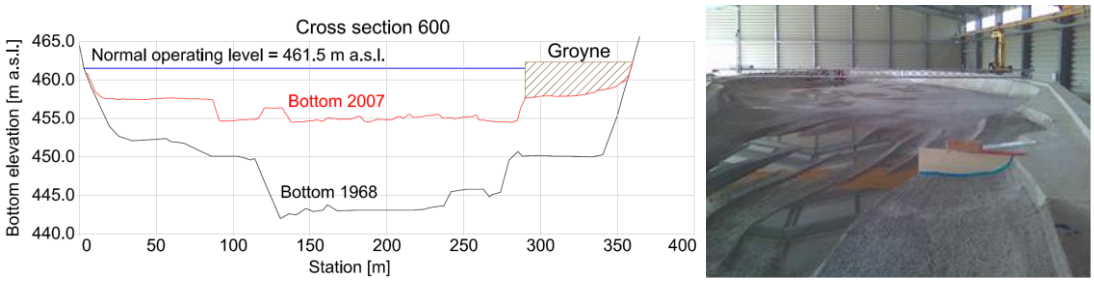

Figure 4.11: Groyne installation; left: cross section 600; right: photograph of the installed groyne in the physical model

4.5 Measurement methodology with the ADCP StreamPro Sensor

The ADCP StreamPro sensor has been developed by the company Teledyne RD Instruments for discharge measurements in shallow water flow conditions in small rivers. The measurement principle is the same as for the RDI Rio Grande ADCPs described in chapter 3. Table 4.4 lists the most important technical specifications of the ADCP StreamPro. Figure 4.12 (left) shows the standard setup with sensor and boat for the use in rivers. The implementation of the sensor in the here presented physical model is depicted in Figure 4.12 (right). Intensive literature review didn't yield any studies on the use of ADCP measurements for determining spatially distributed flow fields in physical models.

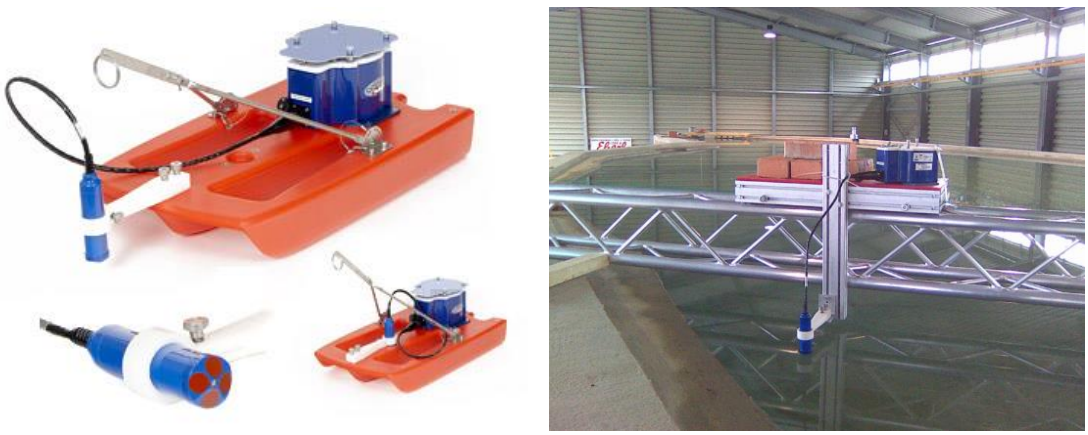

Figure 4.12: RDI ADCP StreamPro; left: sensor with vessel (source: http://www.rdinstruments.com); right: implementation of the sensor in the physical model

Transducer	Frequency Configuration	2 MHz Janus, 4 beams at 20° beam angle
Water Velocity Profiling	Profiling range Velocity range Accuracy Resolution (output) Number of cells Cell size Blanking distance Sampling frequency	0.10 - 6.0 m ± 5 m/s ± 1 % of water velocity 1 mm/s 1 - 30 cells 2 - 20 cm 3 cm 1 Hz

Table 4.4: Technical specifications of the ADCP StreamPro (RDI, 2006c)

ADCP configuration

For the present investigations the so called low noise water profiling mode 13 was applied. This water mode is the recommended configuration for water depths less than 1.0 m and flow velocities less than 0.25 m/s (RDI, 2011). Contrary to the standard water modes, with water mode 13 the transmitter sends one pulse and waits to receive the echo from the pulse before sending the next pulse. This results in a larger time lag between two consecutive pulses. Therefore, this water mode can be used only in shallow water flow if a rapid round trip travel of the sound signal can be guaranteed. With this method the noise is reduced because there is less important level of sound in the water at the same time. The larger time lag between the pulses improves the resolution and the calculation of the phase shift (RDI, Personal communication, 12.10.2009).

In the physical model experiments the ADCP was operated in moving-boat deployment in order to measure the velocity distributions in the entire cross section. For higher measurement quality, the movement of the ADCP vessel along a cross section was controlled by an electric motor. Almost constant vessel velocities of about 1 cm/s were attained with this method. The sensor was positioned vertically with a submersion depth of 2 cm. The depth cell size was set to a value of 5 cm which resulted in a blanking distance of 7 cm at the water surface.

Figure 4.13 illustrates exemplary results of the ADCP test measurements in the physical model for the load case of normal turbine operation. The cross sectional view indicates a severe scattering of the flow velocities in the individual cells in the horizontal as well as in the vertical direction. However, a core of higher flow velocities at the orographic left side can be clearly distinguished, whereas low flow velocities prevail at the orographic right side. The plan view in Figure 4.13 shows the corresponding depth-averaged flow velocities at the cross section. It is remarkable that the process of depth-averaging the velocities in the ensembles has a significant smoothing effect which results in a reasonable shape of the depth-averaged velocity distribution along the cross section. The raw depth-averaged velocity distribution is affected only by some outliers which can be filtered out in the postprocessing analysis.

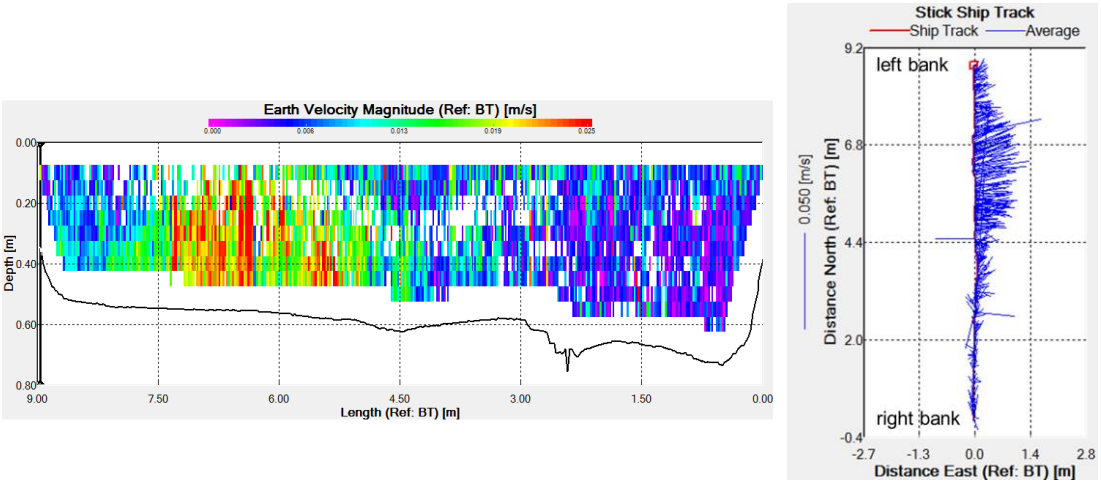

Figure 4.13: ADCP test measurements; left: flow velocity magnitudes in a cross section (raw data); right: plan view of depth-averaged flow velocities at a cross section, (raw data)

The test measurements with the ADCP StreamPro have shown the high potential of using this sensor, within limits, for flow studies in physical models. The velocity measurement in a single cell may have a high uncertainty since the ADCP in moving-boat deployment measures the instantaneous velocity, though, the calculation of the depth-averaged velocities has an effective filtering effect.
The test measurements evidenced the applicability of the ADCP StreamPro sensor in measuring the flow velocities in this physical model. Therefore, this sensor was used for determining the flow patterns in the main physical model experiments.

4.6 Physical model experiments

In the physical model experiments the two hydraulic load cases LC 1 and LC 2 (Table 4.2) have been investigated. The physical model was run to steady state flow condition by keeping constant the inflow discharge as well as the water level at the outlet boundary. The large-scale steady state condition of the flow field was checked by tracer injections and repetitive ADCP measurements. Only some minor unsteadiness of localized flow fields could be observed which didn't affect the developing large-scale flow behaviour. Most likely, the reason was the slightly varying inflow due to the pump operation. The time needed for reaching steady flow conditions was about 24 hours in the turbine load case LC 1. The required long time is reasonable when bearing in mind the very low prevailing Froude numbers in the reservoir (Table 4.2). The ADCP results in terms of the projected flow velocities in model scale in the cross section 500 are shown in Figure 4.14. It demonstrates that from the results the overall flow behaviour can be deduced, even though there exist considerable unmeasured areas near the water surface and the bed.
For the comprehensive analysis of the developing flow fields in the study area, the local measured flow velocities in the ensembles have been averaged over the water depth and scaled up to prototype scale.

The experimental results of the hydraulic load case of turbine operation (LC 1), with and without installation of groyne, are compared with ADCP field measurements in section 5.7.

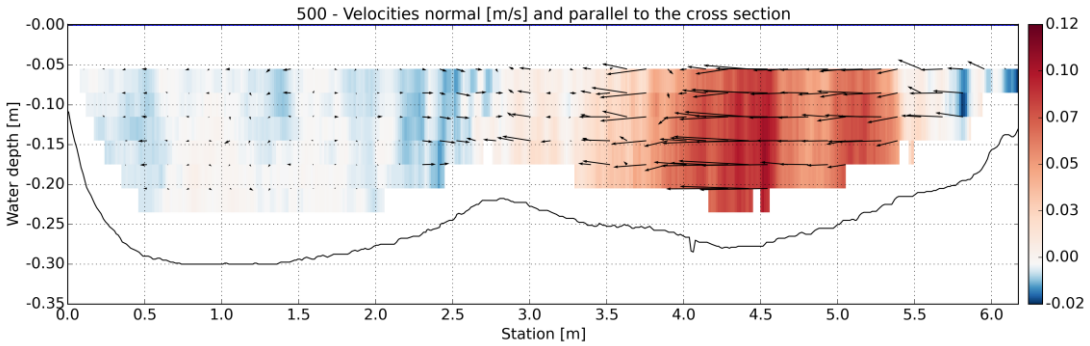

Figure 4.14: Physical model results, LC 1 (turbine operation), normal (coloured) and crosswise (vectors) flow velocities at cross section 500

4.6.1 Experimental results, without groyne

The measured depth-averaged velocity distributions for the case of normal turbine operation (LC 1) are shown in Figure 4.15. NB: the vector scale is 0.5 m/s. The measurements demonstrate the complicated developing flow pattern. In the wider area of the reservoir the main stream towards the hydro power plant is located at the orographic right bank while expanded zones of backflows and still water appear at the orographic left side. Sharp horizontal shear layers emerge which can possibly be attributed to the very slight unsteady meandering behaviour of the internal flow field, despite of the overall steady flow existence. It is remarkable that in the wider area the cores of high velocity zones are very compacted compared to the widths of the cross sections.

The measured flow field for the flushing case (LC 2) is presented in Figure 4.16. NB: the vector scale is 1.0 m/s. The main stream is located at the orographic left bank with the backflow appearing at the right bank. Evidently it can be observed that the flow field under those hydraulic boundary conditions behaves completely different compared to the case of normal turbine operation. The reason for the shifted flow field in LC 2 is the decreased water level in the area between cross section 600 and 500 due to the lowered water level at the outlet. In the zone between cross section 600 and 500 shallow water or almost dry areas develop which cause the effective flow cross section to get shifted away from the right bank (see cross section 600 in Figure 4.16).

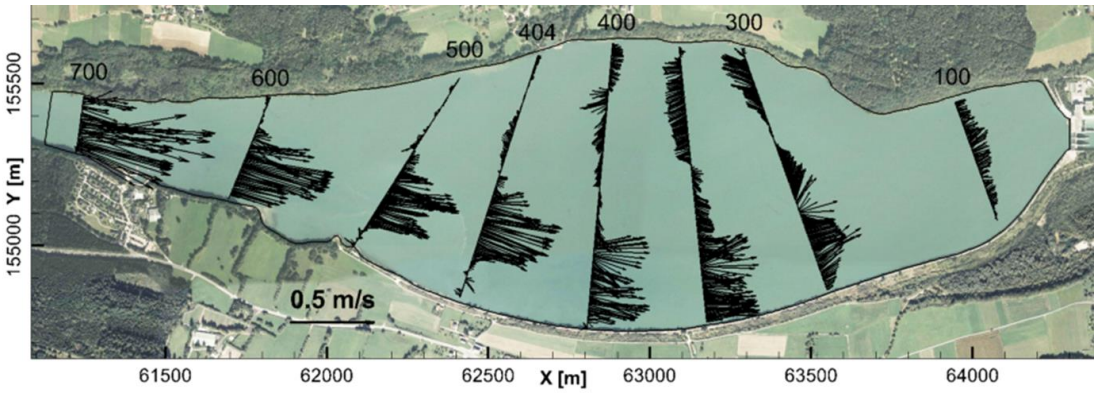

Figure 4.15: Physical model results, LC 1, depth-averaged flow velocities (vector scale: 0.5 m/s)

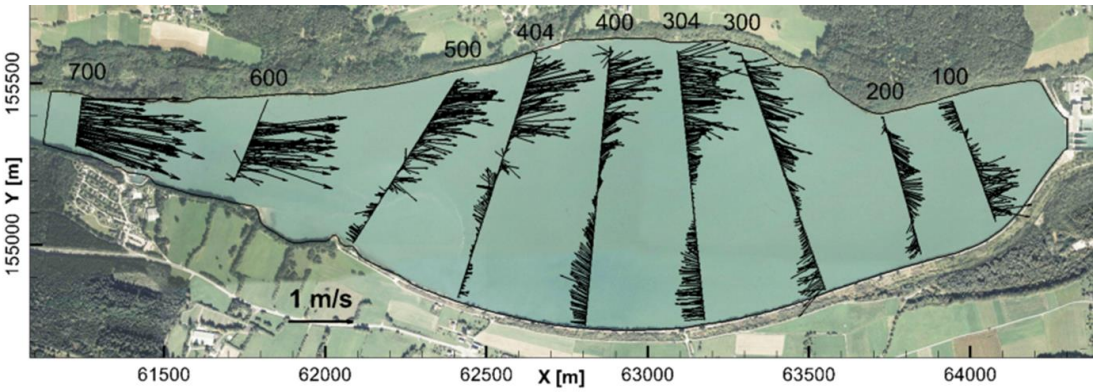

Figure 4.16: Physical model results, LC 2, depth-averaged flow velocities (vector scale: 1.0 m/s)

4.6.2 Experimental results, with installed groyne

The 70 m long non-submerged groyne was installed in the physical model at cross section 600, as explained in section 4.4.2.

The measured flow field for the case of normal turbine operation (LC 1) is shown in Figure 4.17. The comparison with the results for the case without groyne (Figure 4.15) reveals the high impact of the groyne on the developing flow field. The groyne has the effect of shifting the main stream from the orographic right river bank to the left bank in the wider area of the reservoir. In the flushing scenario (LC 2) the location of the main stream is unaltered, with the main stream again developing at the orographic left bank (Figure 4.18).

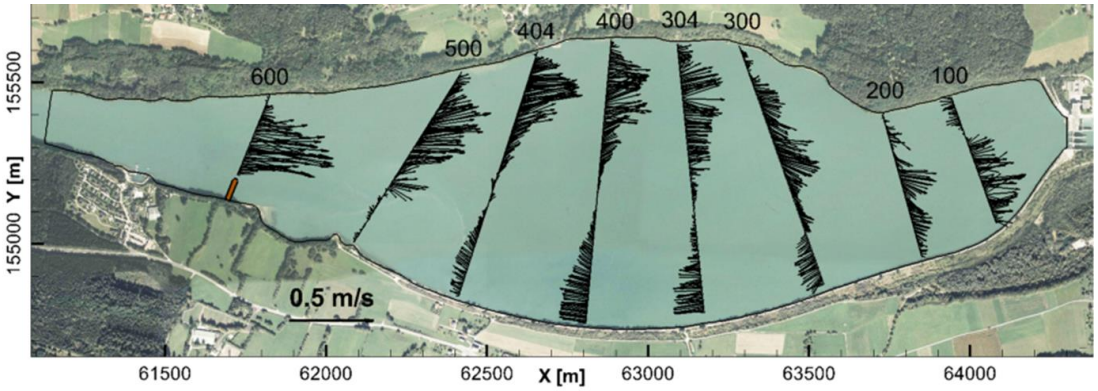

Figure 4.17: Physical model results, installation of the groyne, LC 1, depth-averaged flow velocities

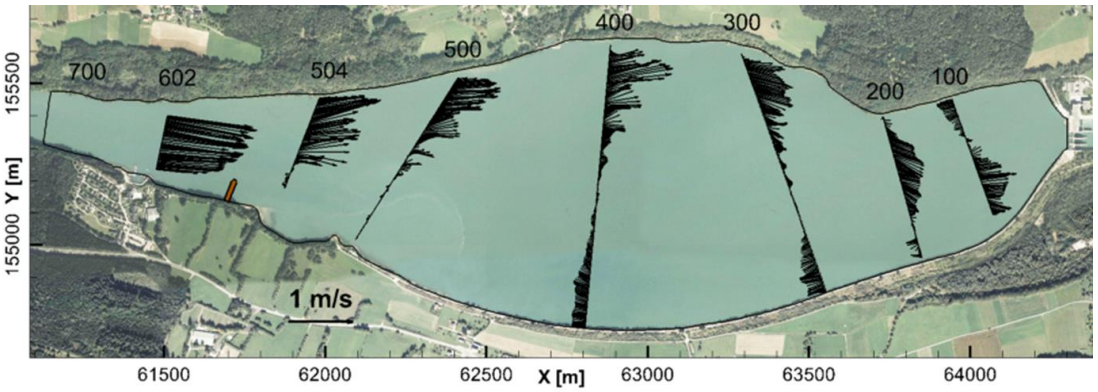

Figure 4.18: Physical model results, installation of the groyne, LC 2, depth-averaged flow velocities

4.7 Summary

The physical model study dealt with the optimization of the sediment management in the reservoir. Purpose of the experiments was the analysis of the developing flow fields in the reservoir under different hydraulic flow conditions. The large-scale flow fields in the physical model were investigated by means of moving-boat Acoustic Doppler Current Profiler (ADCP) velocity measurements.

The physical model investigations of the original state revealed a first explanation for the disordered sedimentation behaviour in the reservoir. Depending on the existing hydraulic boundary conditions, the main stream course changes from the orographic right bank to the left bank and vice versa with the potential development of intermediate states. Hence, the measurements revealed a first explanation for the disordered sedimentation behaviour in the reservoir. The installation of the non-submerged groyne in the physical model of the reservoir has a high impact on the developing flow field in the case of normal turbine flow operation. The groyne has the effect to align the flow fields in terms of the main stream location under the two investigated steady hydraulic flow conditions. In both hydraulic load cases, turbine operation and reservoir flushing, the main stream develops at the orographic left bank with backflow zones at the right bank. The comparison with the original state demonstrated, that the implementation of the groyne effectuates a less scattering of the depth-averaged velocities in both hydraulic load cases. This second finding indicates that the groyne has additionally a stabilizing effect on the developing flow fields. The realization in the physical model study of aligning the flow fields for different hydraulic flow conditions should lead to a reduction of the disordered reservoir sedimentation and increase of the flushing efficiency.

4.8 Implementation of the non-submerged groyne in the prototype

In 2011, based on the physical model results (section 4.6), in the prototype the 70 m long non-submerged groyne was implemented at the orographic right bank of cross section 600 (Figure 4.19). The main objective was the alignment of the flow fields by preserving the main stream at the orographic left bank and the backflow zones at the right bank for a variety of flow conditions, which should lead to the improvement of the sediment management.

The installation of the groyne in the field has provided a unique opportunity to measure the impact of the groyne on the developing flow fields in prototype scale as well as to compare the field measurements with the physical model results and to investigate it numerically.

Figure 4.19: Photograph of the non-submerged groyne at cross section 600 (source: Verbund VHP)

5 ADCP Measurements

In this chapter the results from five ADCP measurement campaigns are presented. The ADCP campaigns aimed at investigating the developing flow fields in the prototype before and after the implementation of the groyne and under different hydraulic boundary conditions in terms of discharge and operating water level.
Two campaigns were performed before the installation of the non-submerged groyne which are described in the sections 5.2 and 5.3. In the sections 5.4, 5.5 and 5.6 the results from the three measurement campaigns after the installation of the groyne are presented.

In section 5.7 two ADCP field campaigns are compared with the results from the physical model experiments.

Section 5.8 discusses two single-point measurements in the estimation of bed shear stress, roughness height and turbulent kinetic energy. The results are compared with approaches from the literature.

5.1 Methodology

The ADCP measurements were carried out in moving-vessel deployment at predefined cross sections using a jet engine boat and by assessing one or more transits per cross section. The continuous position of the boat was determined via a locally corrected global positioning system (RTK GPS) and the internal ADCP compass. The boat velocity was kept as low as possible with boat velocities ranging from 0.5 to 1 m/s. The maximum measurement time per one transect at a cross section was around half an hour. For an optimal measuring performance the power plant operator of the HPP Feistritz provided almost steady turbine discharge and constant operating water level during the respective measuring phase.

The ADCP device RDI Rio Grande 1200 kHz was used. This sensor offers different water profiling modes for different water flow conditions. In all the measurement campaigns Water Mode 12 was used which is an improved version of the default Water Mode 1. Contrary to the standard Mode 1, in Water Mode 12 the device transmits and receives a series of sub-pings. The system then averages the sub-pings to produce ping velocity values. In Water Mode 12 the nominal standard deviation amounts to 6.95 cm/s which is twice as low as in Water Mode 1 (RDI, 2011). The measurement configuration was additionally improved by fine-tuning the maximum bottom tracking depth and the depth cell size for every cross section, based on the available echo sounder surveys. The former setting prevents the ADCP from searching too long and too deep for the bottom, allowing a faster ping rate when the ADCP loses track of the bottom. The default depth cell size was set to a minimum value of 25 cm. This value was increased according to the expected maximum water depth at a cross section in order to account for the recommendation of using maximal

60 depth cells and thus, to achieve higher sampling rates (RDI, 2011). Table 5.1 lists the most important technical specifications of the ADCP Rio Grande 1200 kHz. The photographs in Figure 5.1 show the ADCP and the jet engine boat in operation during a measurement campaign in the reservoir of the HPP Feistritz.

Transducer	Frequency Configuration	1200 kHz Janus, 4 beams at 20° beam angle
Water Velocity Profiling	Profiling range Velocity range Accuracy Resolution (output) Number of cells Cell size Blanking distance Sampling frequency	0.30 - 25.0 m ± 5 m/s ± 0.25 % of water velocity 1 mm/s 1 - 128 cells 0.05 - 2.0 m 0.05 m 1 - 2 Hz

Table 5.1: Technical specifications of the ADCP Workhorse Rio Grande 1200 kHz (RDI, 2006b)

Figure 5.1: ADCP in action in the reservoir of the HPP Feistritz

The analysis of the ADCP measurements has included the following processing steps:

- Correction of the direction angle of the transect (ADCP course) due to compass deviation and magnetic declination with the help of the RTK GPS recording. The measured deviation between ADCP course and GPS course could reach up to 20°deg.
- Evaluation of data quality by comparison of the measured ADCP discharges with the provided turbine discharges (HPP discharges)
- Detection and optional elimination of flow velocity outliers mainly in the zones of the starting and ending points of the transect
- Averaging of velocity data with moving average method
- Calculation of the depth-averaged velocities and projected velocity components at the cross sections
- Georeferencing of the ADCP data

5.2 Campaign 1

5.2.1 Measurement setup

In the first ADCP measurement campaign, conducted on 29.05.2008, the flow velocities were measured at 10 cross sections by performing one transect per cross section. During the measuring phase the HPP discharge and the operating water level were nearly constant with average values of 440 m³/s and 461.35 m a.s.l., respectively. The hydraulic conditions correspond approximately to the design discharge (440 m³/s) and the normal operating water level (461.5 m a.s.l.). The HPP discharge and the water level were held approximately constant for a period of more than three hours before the start of the measurement campaign with the intention to reach almost steady flow conditions in the reservoir.

The comparison between the HPP discharges and the measured ADCP discharges, shown in Figure 5.2, reveals a generally excellent agreement. The time-dependent discharge and operating water level are plotted on the left and right ordinate, respectively. At most of the cross sections the relative errors of the ADCP discharges in relation to the HPP discharges are below the recommended threshold value of 5 % (RDI, 2011). The measured ADCP discharges at cross sections 01, 400 and 500 have a higher deviation with relative errors of up to 9 % (Table 5.2). At cross sections 400 and 500 the reason for the discrepancies can be related to the presence of weak unsteady oscillating flow, which implies that at these cross sections the assumption of steady flow conditions during the boat transits could not be met.

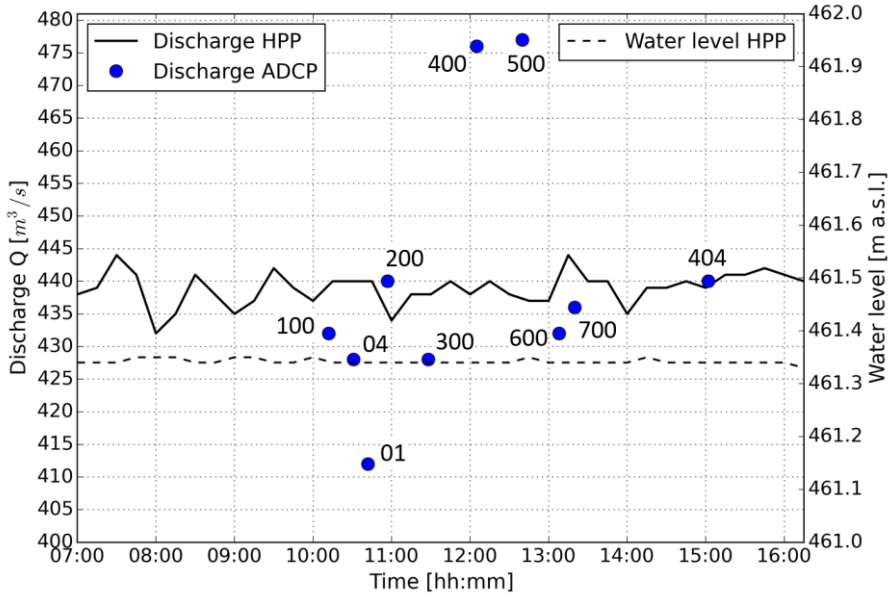

Figure 5.2: Campaign 1 (29.05.2008): comparison of the ADCP discharges with the HPP discharges

Cross section	**01**	**04**	**100**	**200**	**300**	**400**	**404**	**500**	**600**	**700**
Relative error [%]	-6.4	-2.7	-1.8	1.4	-2.3	8.7	0.2	9.2	-1.8	-1.1

Table 5.2: Campaign 1: relative errors of the ADCP discharges in relation to the HPP discharges

5.2.2 Results

The analysis by means of the depth-averaged velocity distributions and the cross sectional velocities manifests a complex developing flow pattern in the reservoir. Figure 5.3 shows the flow field by means of the depth-averaged flow velocities. Downstream from the gorge portion (cross section 700) the main stream of the flow is moving to the orographic right side of the reservoir. Expanded zones of backflows and still water develop at the orographic left side. At the orographic right side between cross sections 600 and 404 the measurements indicate backflow zones as well. In the wider area of the reservoir the cores of high velocity zones are very compacted compared to the widths of the cross sections, as exemplary shown for cross section 500 by means of the velocity magnitudes (Figure 5.4). Downstream from cross section 200 the depth-averaged velocity distributions are again uniform over the cross sections until directly upstream from the turbine inlets.

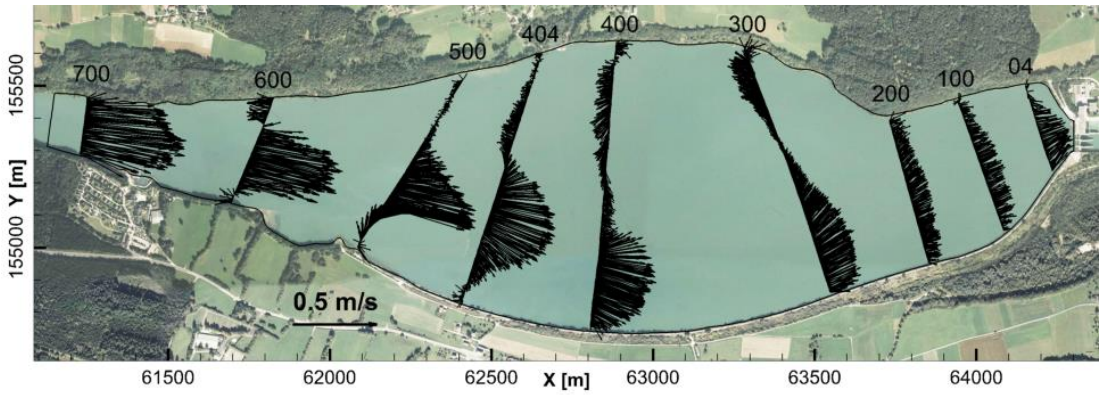

Figure 5.3: Campaign 1: plan view, depth-averaged flow velocities

Focusing on cross section 500, the analysis of only the depth averaged velocity distribution for the zone between cross section stations 0 and 300 m would indicate a still water zone in which the velocities fluctuate around an average value of zero m/s. However, as Figure 5.5 shows, the analysis of the projected velocities by means of the normal (coloured) and crosswise (vectors) velocity components reveals a streamwise vertical recirculation flow in the left part of the cross section. Between the water surface and a water depth of about 4 m the flow moves upstream, whereas the flow moves downstream near the bed. At no other cross section such an evident vertical recirculation flow along the main stream direction could be detected.

In summary, the developing depth-averaged flow field consists of one big counter-clockwise vortex. Abrupt transitions between downstream and upstream flow emerge locally, resulting in very sharp horizontal shear layers. The projected flow velocities shown for the cross sections 500 and 400 in Figure 5.5 and Figure 5.6, respectively, demonstrate the crosswise recirculations and flow redistributions. They indicate the presence of strong secondary currents.

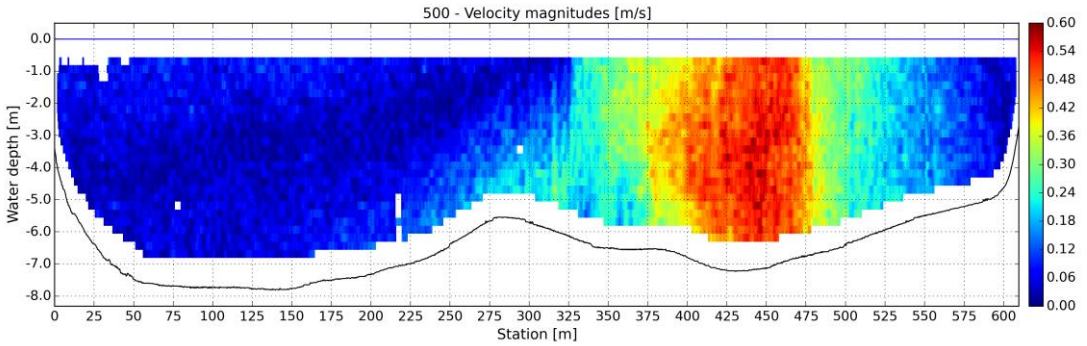

Figure 5.4: Campaign 1: cross section 500, flow velocity magnitudes

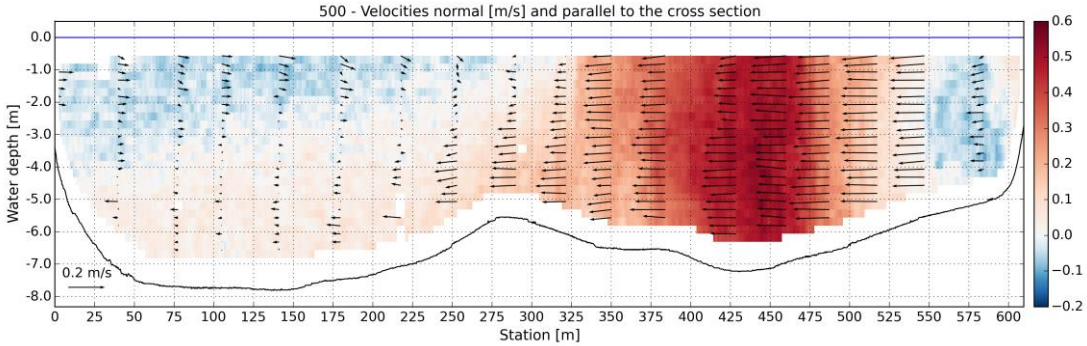

Figure 5.5: Campaign 1: cross section 500, projected flow velocities, normal (coloured) and crosswise (vectors) to the cross section

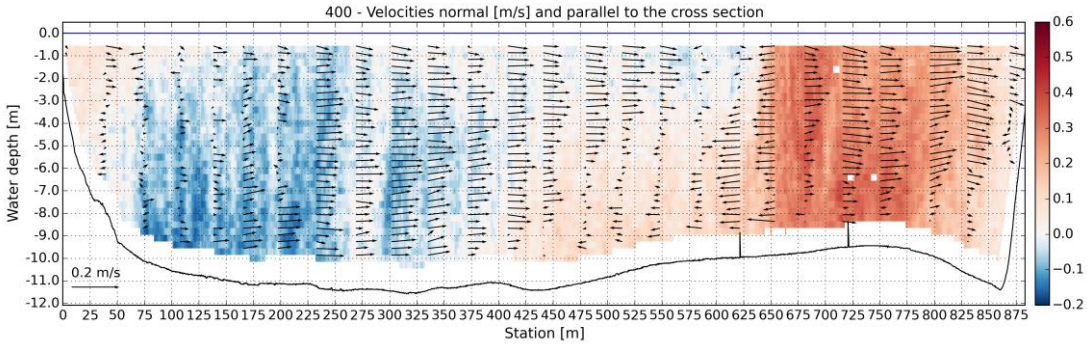

Figure 5.6: Campaign 1: cross section 400, projected flow velocities

As a side product of measurement campaign 1, the flow velocities also were measured at cross section 01 which is located around 25 m upstream from the turbine inlets. The evaluation of the depth-averaged velocities demonstrates the applicability of the ADCP measuring technique for the investigation of turbine approach flow (Figure 5.7). The analysis of the projected flow velocities in cross section 01 evidences the presence of spiral flow in front of the turbine inlets (Figure 5.8).

Figure 5.9 shows a 3D view of the developing flow field in the reservoir by means of the measured normal flow velocities to the cross sections and the digital elevation model.

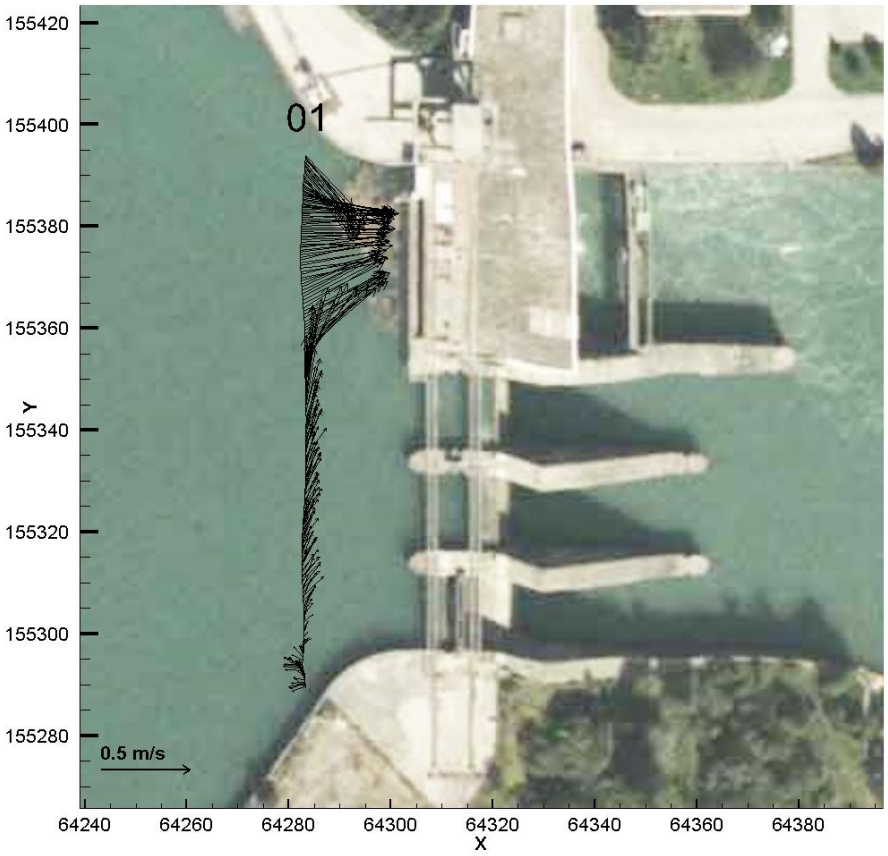

Figure 5.7: Campaign 1: plan view detail, depth-averaged flow velocities at cross section 01

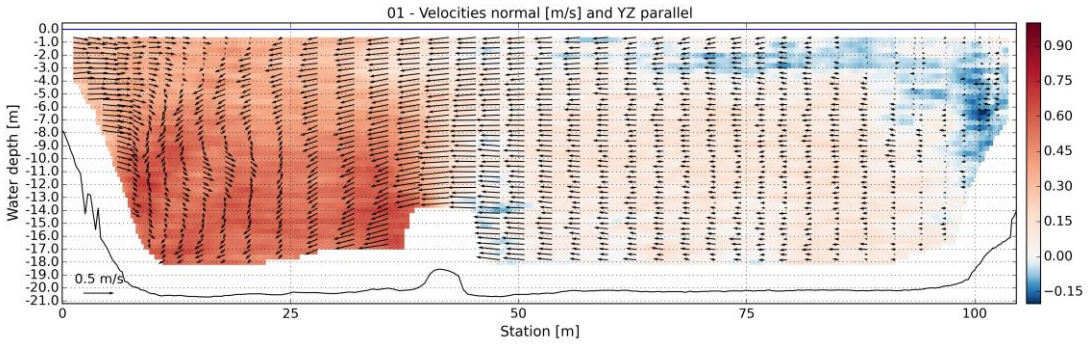

Figure 5.8: Campaign 1: cross section 01, projected flow velocities

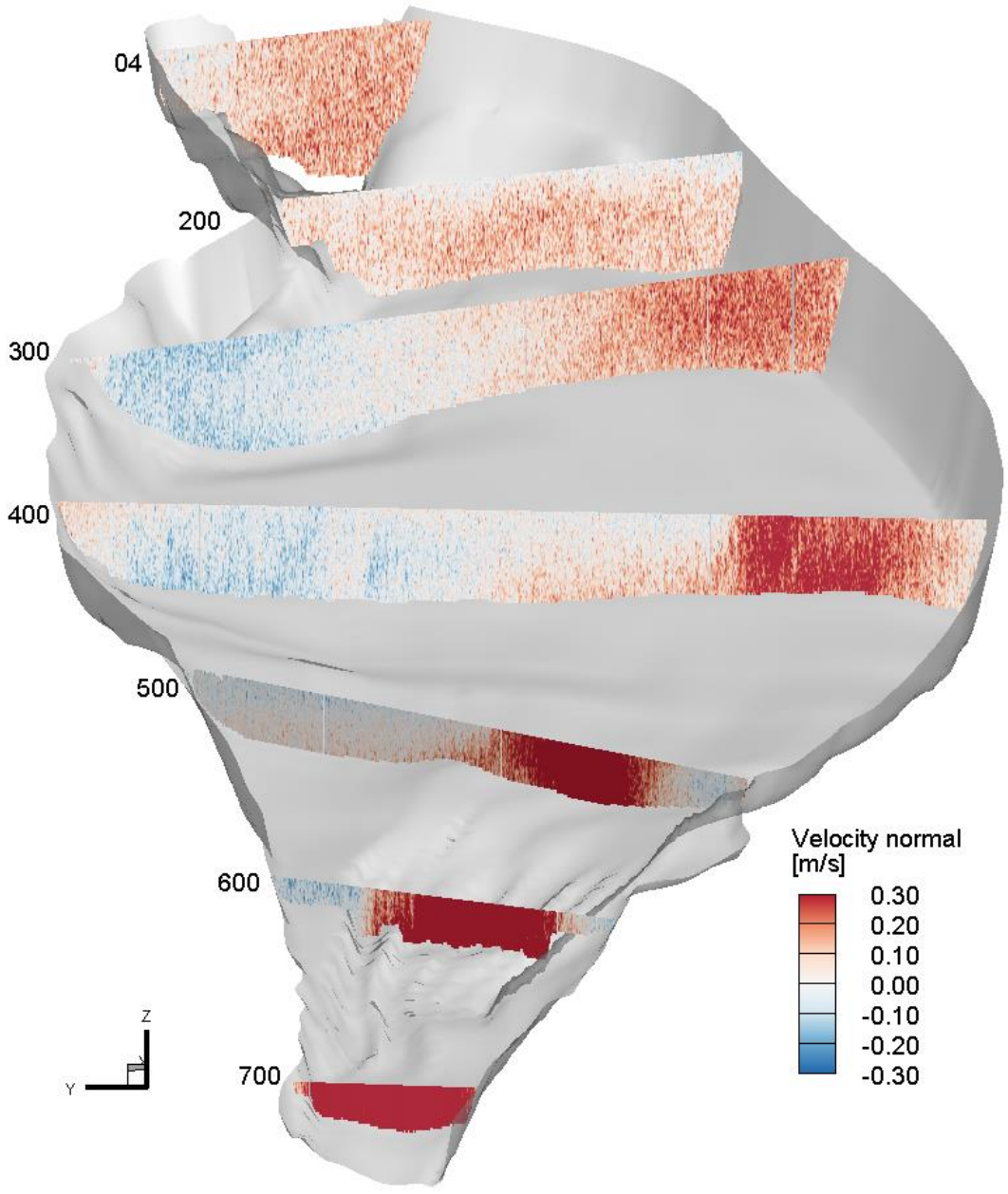

Figure 5.9: Campaign 1: 3D view (4x vertical exaggeration), normal flow velocities and digital elevation model

5.3 Campaign 2

5.3.1 Measurement setup

In this measurement campaign, conducted on 24.06.2009, the focus was on the investigation of the developing flow field under different hydraulic boundary conditions, compared to the measurement campaign 1. The a priori hypothesis was that at lower operating water levels in the shallow water areas at the orographic right side between cross sections 600 and 500 the submergence decreases. Due to the decreased overflow this zone acts as a submerged

headland which, compared to campaign 1, causes the main stream to be shifted from the right orographic bank to the center. For the verification of this assumption the hydro power owner provided a constant water level of 460.50 m a.s.l. for the measuring phase which is 1 m below the normal operating water level. The average HPP discharge was 365 m³/s which corresponds to around 80 % of the design turbine discharge. The preliminary lead time with approximately constant HPP discharge and water level until the start of the measurements was around one hour. The flow velocities were measured at 9 cross sections. At cross sections 500 and 304 two ADCP transects were carried out. At cross section 500 the time difference between the two transits was around half an hour, whereas at cross section 304 it was around three hours. At cross section 400 the transect had to be interrupted due to a measuring fault and therefore, the ADCP discharge was extrapolated based on the last valid measured data.

The comparison between the HPP discharges and the ADCP discharges is shown in Figure 5.10. Table 5.3 lists the relative errors. The ADCP discharges in overall agree well with the HPP discharges. However, at the cross sections 400_{corr}, 304_1 and 300 the ADCP discharges are overestimated by around 10 %.

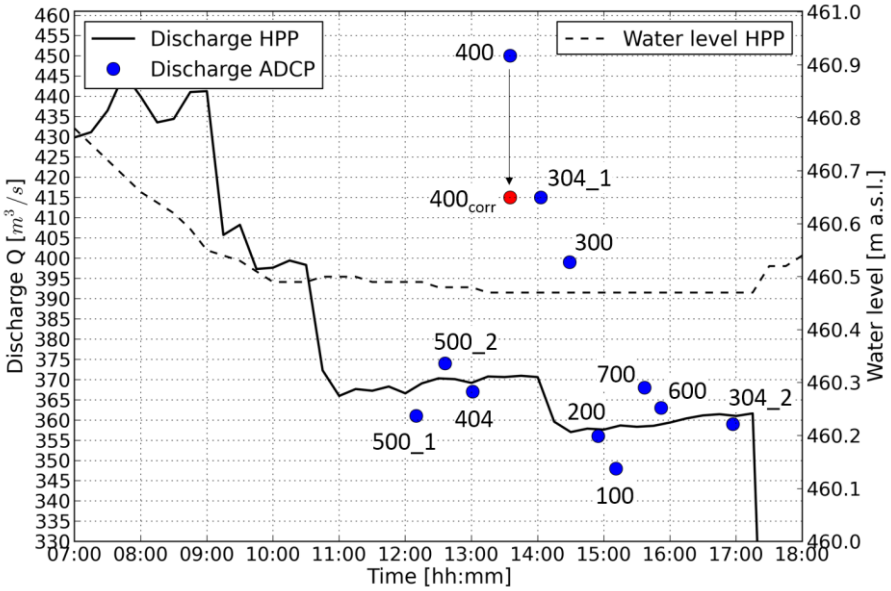

Figure 5.10: Campaign 2 (24.06.2009): comparison of the ADCP discharges with the HPP discharges

Cross section	**100**	**200**	**300**	**304_1**	**304_2**	**400_{corr}**	**404**	**500_1**	**500_2**	**600**	**700**
Relative error[%]	-2.8	-0.6	11.8	12.8	-0.6	11.9	-0.5	-1.9	1.1	1.1	2.5

Table 5.3: Campaign 2: relative errors of the ADCP discharges in relation to the HPP discharges

5.3.2 Results

The measured depth-averaged flow field in the reservoir is shown in Figure 5.11. Compared to the results from campaign 1, in the wider area the main stream is distinctively shifted from the right orographic bank to the center with the presence of backflows at the left and right

side. These results prove the assumption of the altered developing flow pattern emerging under other hydraulic conditions. The repeated measurements at the cross sections 500 and 304 demonstrate the meandering flow behaviour. Especially the results from the transits 500_1 and 500_2 prove the unsteady flow behaviour, when considering the short time difference of only half an hour between the two measurements. In the two transits the developing depth-averaged velocity distributions are rather different in terms of velocity magnitudes and flow directions. In the two transits 304_1 and 304_2 the depth-averaged velocity distributions agree fairly well, though, the unsteadiness is also visible. In the contraction zone downstream from cross section 200 the approach flow to the turbines is considerably different to the measurement results from campaign 1.

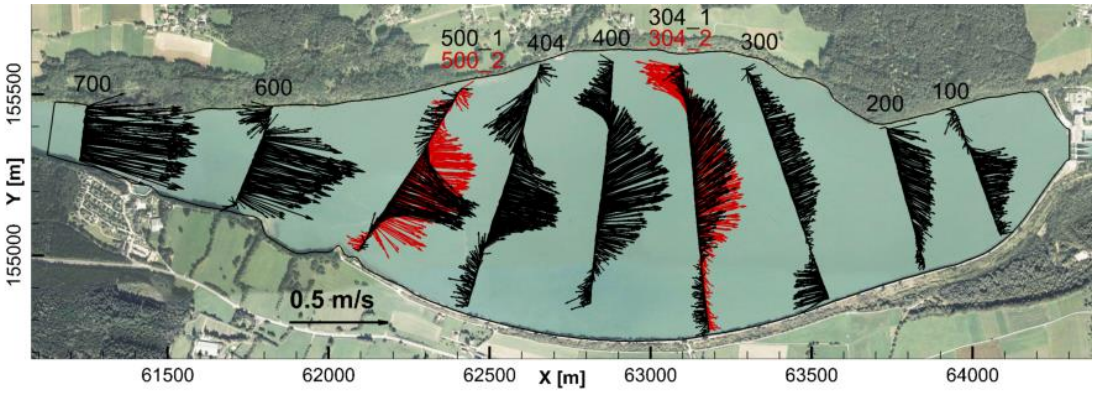

Figure 5.11: Campaign 2: plan view, depth-averaged flow velocities

The projected velocities for the cross sections 500 and 304 are shown in Figure 5.12 and Figure 5.13, respectively. In cross section 500_1 the main stream is more compact compared to the results from transit 500_2. In the two transits, around cross section station of 250 m the crosswise velocities are reversed which indicates large flow redistributions. At cross section 304, the results from both transects 304_1 and 304_2 show similar distributions of the projected flow velocities. However, the comparison reveals a slight meandering of the main stream. At the orographic right bank, over a width of approximately 150 m, in the two transits the main flow directions are inverted. Moreover, it can be noted that in transit 304_2 the backflow at the orographic left bank is much more pronounced compared to transit 304_1.

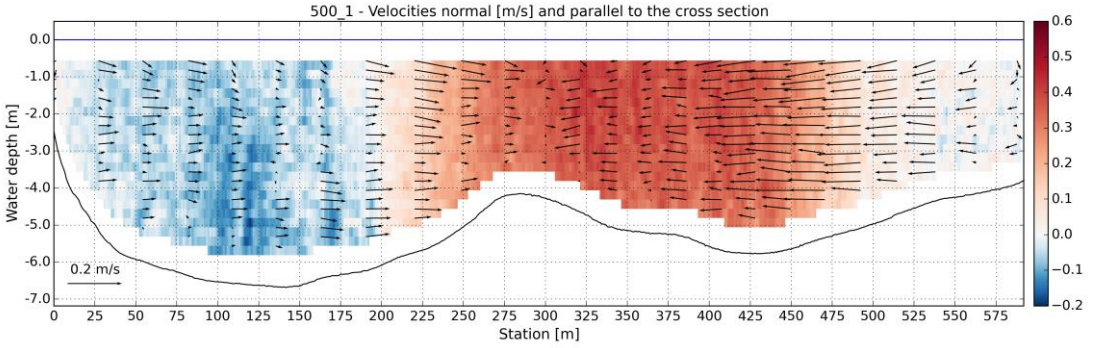

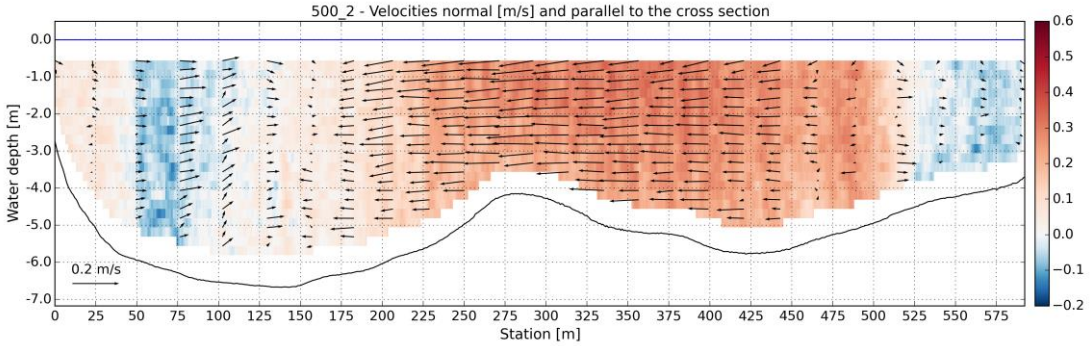

Figure 5.12: Campaign 2: cross section 500, transects 500_1 and 500_2, projected flow velocities

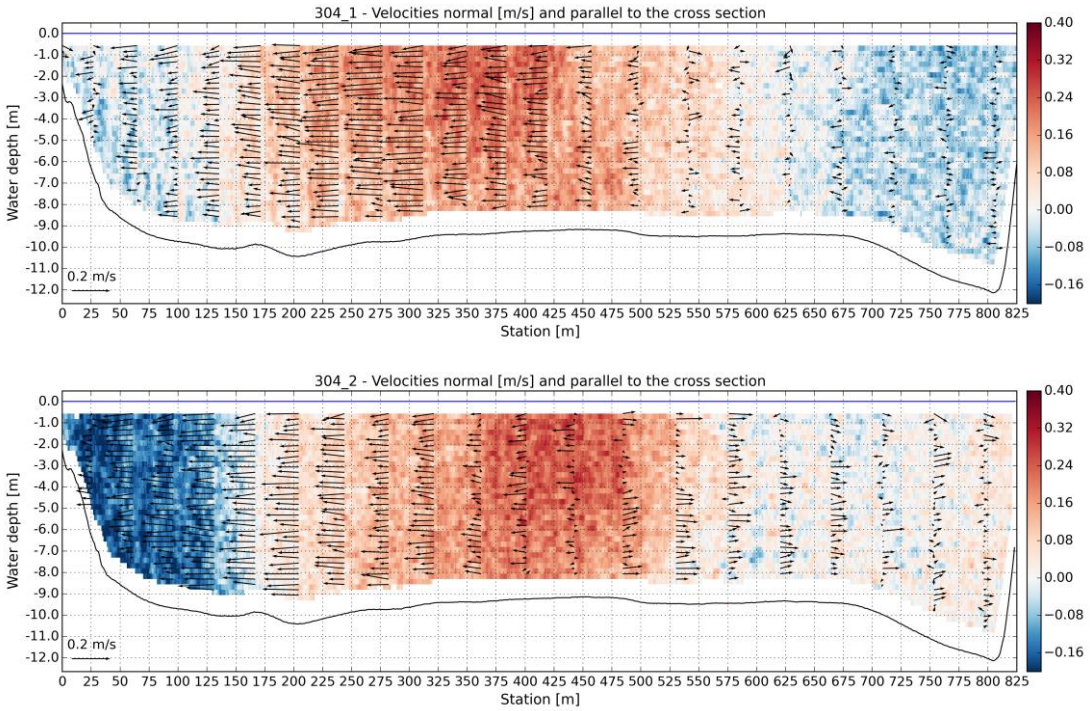

Figure 5.13: Campaign 2: cross section 304, transects 304_1 and 304_2, projected flow velocities

5.4 Campaign 3, after installation of the groyne

5.4.1 Measurement setup

The measurement campaign 3, conducted on 22.05.2013, represents the first ADCP velocity measurements after the installation of the non-submerged groyne at the orographic right bank at cross section 600. The HPP discharge and the operating water level were almost perfectly constant with average values of 435 m³/s and 461.20 m a.s.l., respectively. The flow velocities were measured at 10 cross sections by performing one transect per cross section. As in campaign 1, the HPP discharge and the water level were held almost constant for a period of more than three hours before the start of the measurement campaign.

The comparison of the ADCP discharges with the HPP discharges, shown in Figure 5.14 and Table 5.4, illustrates a good agreement. Only at cross section 100 the discharge measured by the ADCP is underestimated by 10 % compared to the HPP discharge. The reason for this discrepancy isn't totally clear since cross section 100 is in the contraction zone where a stable flow field should be expected. Indeed, the deviation may also suggest the presence of a weak unsteady flow behaviour in this area.

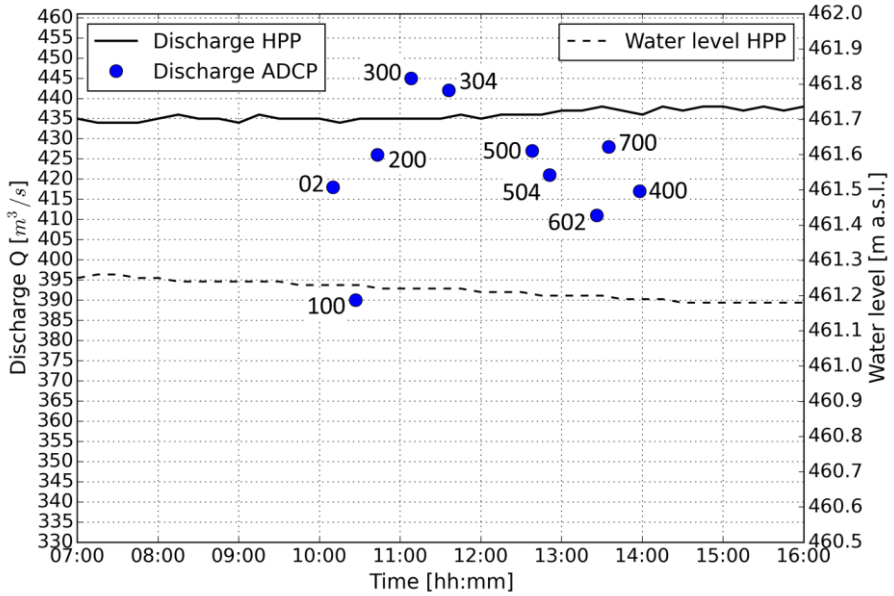

Figure 5.14: Campaign 3 (22.05.2013): comparison of the ADCP discharges with the HPP discharges

Cross section	**02**	**100**	**200**	**300**	**304**	**400**	**500**	**504**	**602**	**700**
Relative error[%]	-3.9	-10.3	-2.1	2.3	1.4	-4.4	-2.1	-3.4	-6.2	-2.3

Table 5.4: Campaign 3: relative errors of the ADCP discharges in relation to the HPP discharges

5.4.2 Results

The measured depth-averaged velocity distributions indicate a stable developing flow field in the reservoir (Figure 5.15). The large-scale flow field consists of one large clockwise vortex. Smaller vortices emerge in the shallow water areas at the orographic right side between cross sections 504 and 400. Compared to the results from campaign 1, the measured flow field behaves remarkably different, with the location of the main stream taking place on the opposite side in the wider area of the reservoir.

In summary, the results from this measurement campaign demonstrate the controlling influence of the non-submerged groyne on the developing large-scale flow field in the reservoir, at least under the hydraulic flow conditions described above.

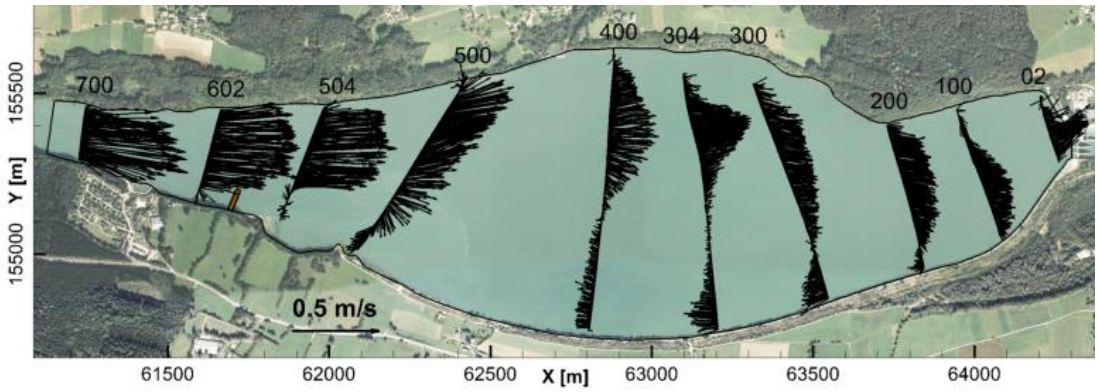

Figure 5.15: Campaign 3: plan view, depth-averaged flow velocities, after installation of groyne

5.5 Campaign 4, after installation of the groyne

5.5.1 Measurement setup

The measurement campaign 4 was conducted on 07.05.2014. The average HPP discharge was 395 m³/s with some variation in the order of ± 5m³/s. The water level at the HPP corresponded to the normal operating level of 461.5 m a.s.l. and was kept almost perfectly constant. The flow velocities were measured at 9 cross sections. At cross section 500 two ADCP transects were performed with a time difference of approximately 15 minutes. The preliminary lead time with approximately constant hydraulic flow conditions until the start of the measurement campaign was around two hours.

The comparison of the ADCP discharges with the HPP discharges is shown in Figure 5.16 and Table 5.5. As in the prior campaigns, the measured ADCP discharges agree well with the HPP discharges, with a larger deviation of around 9 % appearing at cross section 304.

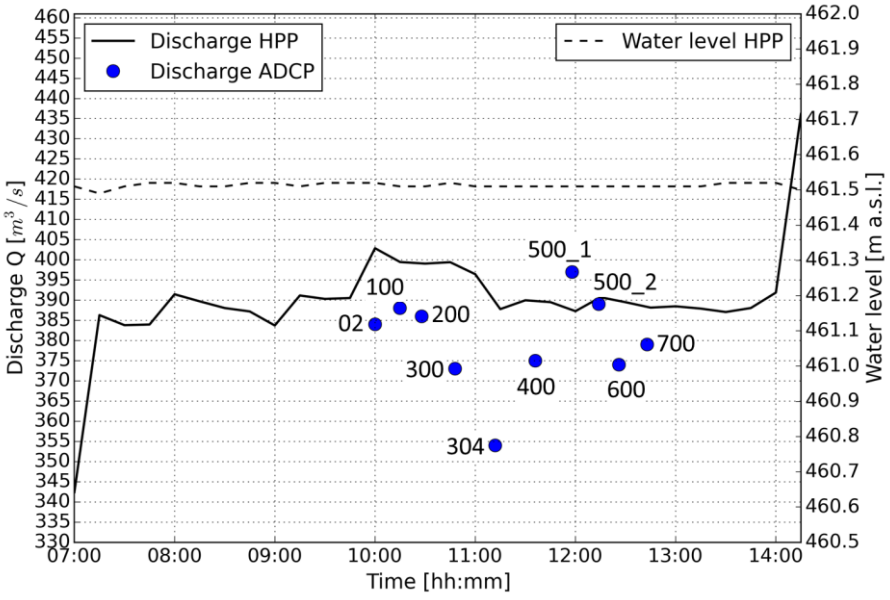

Figure 5.16: Campaign 4 (07.05.2014): comparison of the ADCP discharges with the HPP discharges

Cross section	02	100	200	300	304	400	500_1	500_2	600	700
Relative error[%]	-4.5	-2.8	-3.3	-6.5	-8.5	-3.6	2.6	-0.3	-3.9	-2.3

Table 5.5: Campaign 4: relative errors of the ADCP discharges in relation to the HPP discharges

5.5.2 Results

The developing depth-averaged flow field is shown in Figure 5.17. The repeated measurements 500_1 and 500_2 at cross section 500 show similar depth-averaged velocity distributions with the main flow direction towards the orographic left bank. Compared to the measured velocity distributions in campaign 3, the flow field is distinctively altered in the entire wider area of the reservoir. At cross section 400 the main downstream flow is very compact in the center with backflows at the left and right side of it. At cross sections 304 and 300 the main stream tends to the orographic right bank. At cross section 200 the main stream is shifted to the orographic left bank with the highest velocities in the immediate vicinity of it. By examining the results at the cross sections 400 and 304 more specifically and by considering the short time difference of around half an hour between the two transits, the depth-averaged velocity distributions have rather different shapes and characterize local developing flow fields which evidently don't fit together.

The measurement results demonstrate the distinct influence of the non-submerged groyne on the developing flow field in the reservoir. However, compared to the results from the preceding campaign 3, a more dynamic flow field develops in the reservoir. The results reveal the unsteady oscillating flow behaviour which indicates that the groyne has not enough impact to stabilize the flow field in the wider area of the reservoir.

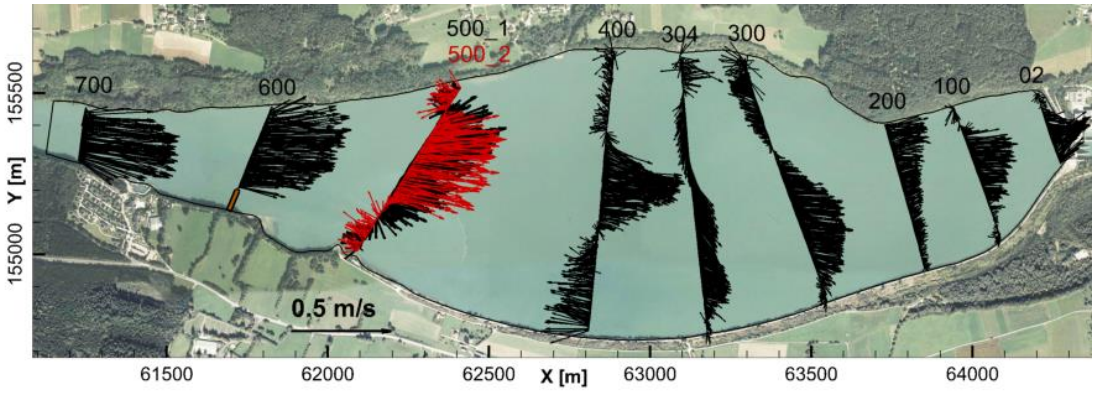

Figure 5.17: Campaign 4: plan view, depth-averaged flow velocities, after installation of groyne

5.6 Campaign 5, after installation of the groyne

5.6.1 Measurement setup

The measurement campaign 5 was conducted on 08.05.2014, one day after the campaign 4. With the intent to investigate the flow behaviour under different hydraulic flow conditions,

the water level was set to 461.0 m a.s.l. which is 0.5 m below the normal operating water level. The average HPP discharge was 420 m³/s with variations in the order of ± 5m³/s. The flow velocities were measured at 9 cross sections. At cross sections 500 and 400, two ADCP transects were performed. At cross section 500 the time difference between the two transits 500_1 and 500_2 was around 15 minutes, whereas at cross section 400 it was almost half an hour between the transits 400_1 and 400_2.

The analysis of the ADCP discharges and the HPP discharges indicates larger deviations between them, compared to the measurement campaigns 3 and 4. Figure 5.18 shows the comparison of the ADCP discharges with the HPP discharges. Table 5.6 lists the relative errors.

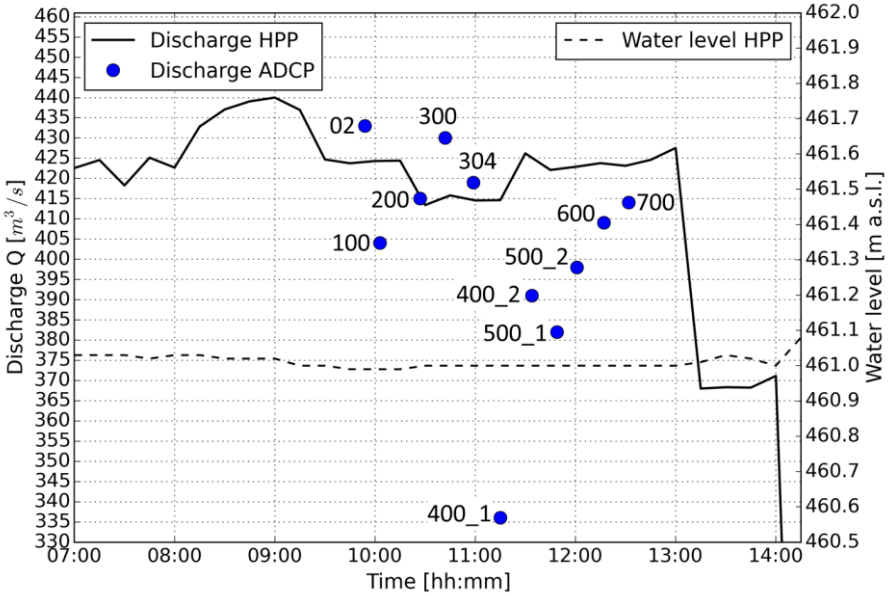

Figure 5.18: Campaign 5 (08.05.2014): comparison of the ADCP discharges with the HPP discharges

Cross section	**02**	**100**	**200**	**300**	**304**	**400_1**	**400_2**	**500_1**	**500_2**	**600**	**700**
Relative error[%]	2.1	-4.7	0.0	3.6	1.0	-19.0	-7.8	-9.5	-5.9	-3.3	-2.1

Table 5.6: Campaign 5: relative errors of the ADCP discharges in relation to the HPP discharges

5.6.2 Results

The depth-averaged velocity distributions, shown in Figure 5.19, again reveal a very interesting flow behaviour. The non-submerged groyne located at cross section 600 has a controlling impact on the developing flow field in the reservoir. However, the repeated measurements at the cross sections 500 and 400 demonstrate the remarkable unsteady flow behaviour, bearing in mind the short time interval between the respective transits.
The analysis of the projected velocities for both transects 400_1 and 400_2 in cross section 400 is presented in Figure 5.20. In cross section 400_1 the zone of high velocities in the downstream direction is more compact than in cross section 400_2. In 400_1 a backflow

zone emerges around the station 175 m which in 400_2 doesn't exist anymore. The widths of the backflow zones near the orographic right bank agree well. In the zone of the main stream the crosswise flow velocities are completely reversed which again indicates large time-dependent flow redistributions in the wider area of the reservoir.

The results from this campaign prove that the non-submerged groyne has an effect on the developing flow in that the main stream is shifted towards the orographic left bank in the reservoir. The measurements confirm the results from the preceding ADCP campaign regarding the development of unsteady oscillating flow fields. It can be stated that also under the hydraulic flow conditions in campaign 5, the groyne does not have enough impact in order to stabilize the flow field in the wider area of the reservoir.

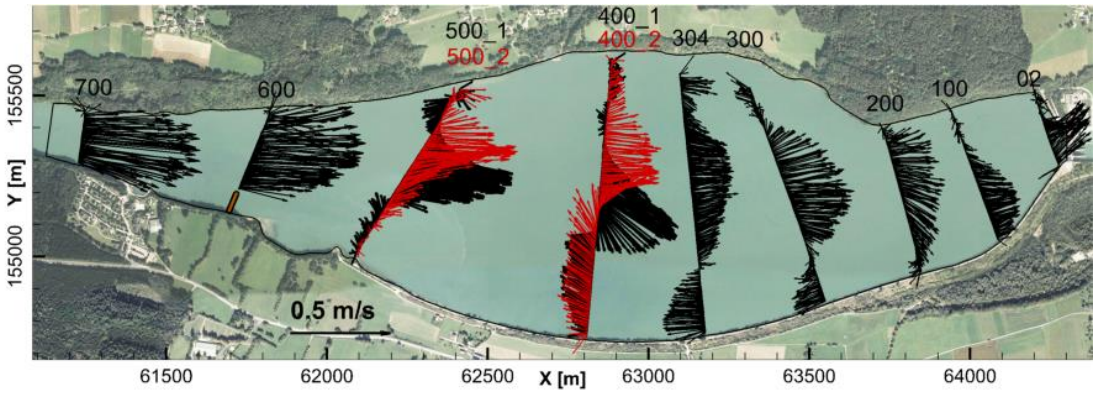

Figure 5.19: Campaign 5: plan view, depth-averaged flow velocities, after installation of groyne

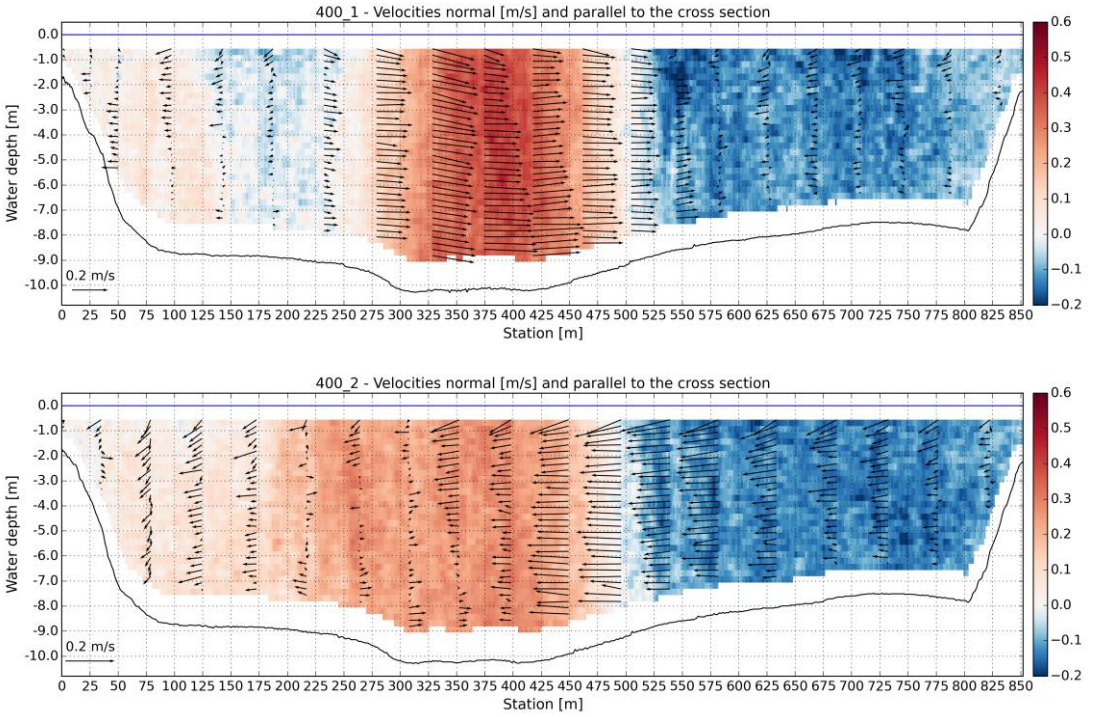

Figure 5.20: Campaign 5: cross section 400, transects 400_1 and 400_2, projected flow velocities

5.7 Comparison of ADCP field measurements with physical model results

The ADCP field measurements in campaigns 1 (before installation of the groyne, section 5.2) and 3 (after installation of the groyne, section 5.4) had very similar hydraulic boundary conditions to the hydraulic load case LC 1 (normal turbine operation) applied in the physical model experiments (sections 4.6.1 and 4.6.2). Additionally, on the respective day of the two field measurements, the HPP discharge and the operating water level were kept almost constant over a satisfactory preliminary lead time before the measurement start.

The comparisons of the ADCP campaigns 1 and 3 with the physical models results by means of the depth-averaged flow velocities are shown in Figure 5.21 and Figure 5.22. In both cases, with and without implementation of the groyne, the ADCP measurements in the prototype reproduce the measured flow fields in the physical model experiments very well, or vice versa. The horizontal shear layers and the zones of transition between downstream and upstream flows impressively occur at the almost same locations.
The matching results prove the impact of the non-submerged groyne on the developing flow field. Furthermore, the comparative study confirms the overall existence of steady state flow field conditions in the reservoir if steady or almost steady hydraulic boundary conditions are present.

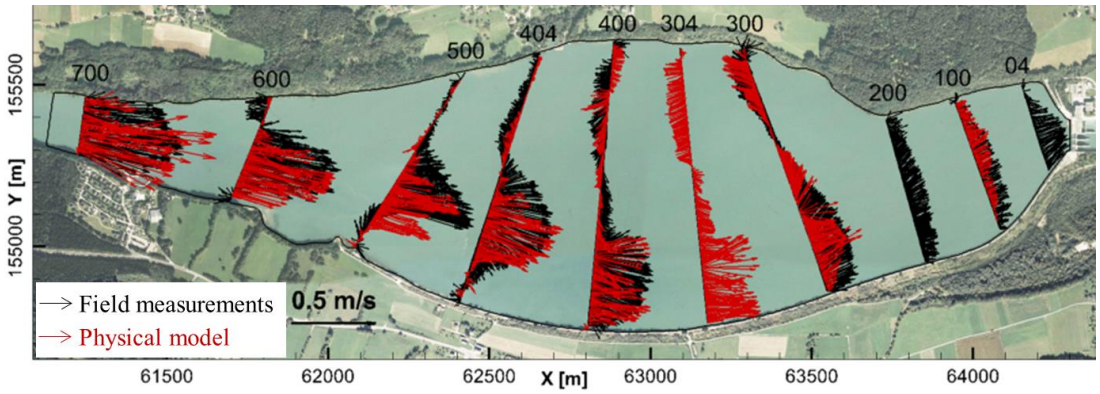

Figure 5.21: ADCP field campaign 1 and physical model results, depth-averaged flow velocities

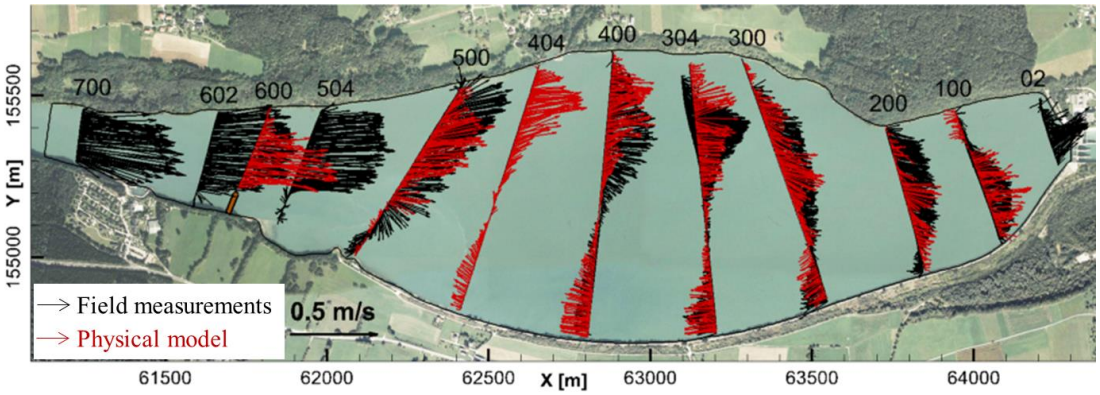

Figure 5.22: ADCP field campaign 3 and physical model results, after implementation of the groyne, depth-averaged flow velocities

5.8 Estimation of bed shear stress, roughness height and turbulent kinetic energy

This section presents some tentative analysis for the estimation of bed shear stress, roughness height and turbulent kinetic energy, based on two stationary ADCP measurements.

5.8.1 Measurement methodology

In a separate measurement campaign stationary ADCP measurements were conducted at several points in the reservoir. During the measuring phase the HPP discharge and the operating water level were kept almost constant with average values of 400 m³/s and 461.40 m a.s.l., respectively. The measuring boat was anchored at a specific measuring point via GPS positioning. With this method it was not possible to fix the ADCP sensor itself at the predefined immovable point, in the sense to have a real stationary measurement, but the ADCP device had some tolerance to drift. The preliminary examination of the data revealed that the ADCP results from most of the measured points were bad or useless because of too much drifting of the boat or stationary non-homogeneity, respectively. Though, the ADCP data from two measurement points located at the cross sections 700 and 500 have been considered to be suitable for the estimation of bed shear stress, roughness height and turbulent kinetic energy.

The measurements were carried out by means of the ADCP device RDI Rio Grande 1200 kHz. Like in the previously presented measurement campaigns, the water profiling method Water Mode 12 was used. The depth cell size was set to 25 cm and the sampling time was set to 90 seconds which resulted in a sampling frequency of around 1.5 Hz. The ADCP bottom tracks along with the depth-averaged flow velocities at the two measuring points 700 and 500 are shown in Figure 5.23. The ship tracks exhibit the drifting of the ADCP device within the distance of some meters, resulting in an effective horizontal measuring field of around 6 m² at point 700 and around 18 m² at point 500.

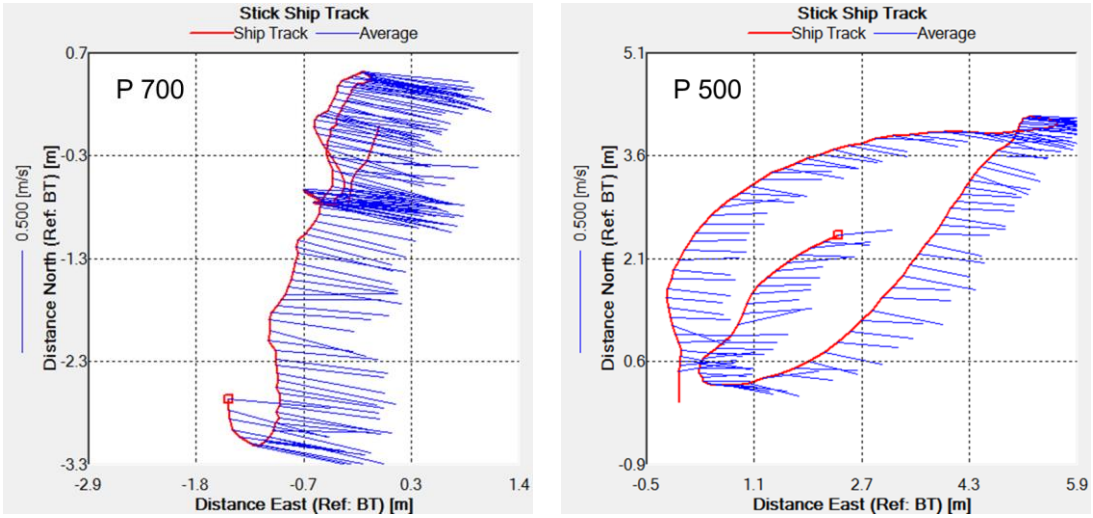

Figure 5.23: Measurement points 700 and 500; ADCP track (red) and depth-averaged velocities (blue)

5.8.2 Processing of the ADCP data

In a first analysis the time stationarity of the velocity signal was checked by calculating the cumulative mean over time for the velocity components. Figure 5.24 shows the cumulative mean over time of the horizontal velocity magnitudes UV at different water depths (Surface, Center = 3 m water depth, Bottom). At both points 700 and 500 the convergence of the velocity signal to a stationary value after 90 seconds is not perfect but acceptable.

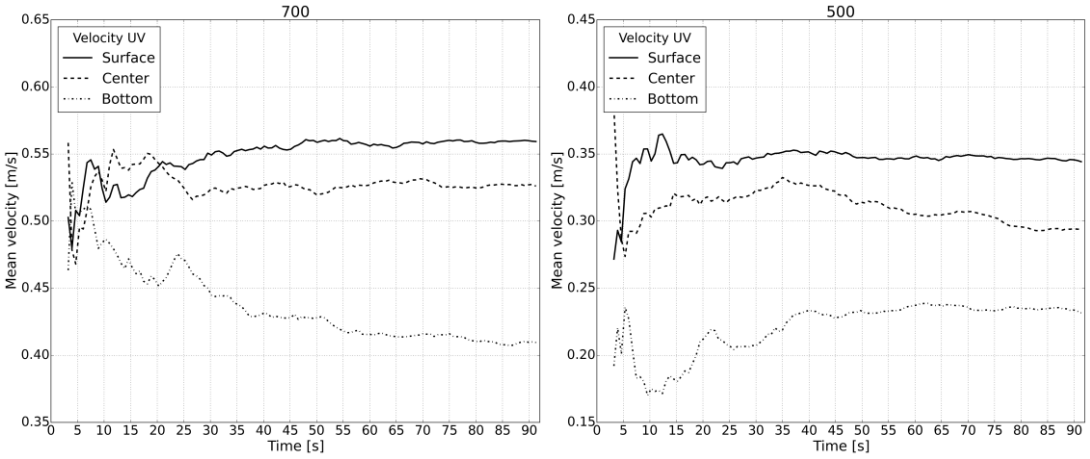

Figure 5.24: Cumulative mean over time of the velocity vectors UV at different water depths at the measurement points 700 and 500

From the raw data the time-averaged velocity vectors at different water depths and their depth-averaged velocity vector were calculated. The mean velocity magnitudes at different water depths and their depth-averaged velocity at the predefined (virtual) georeferenced points 700 and 500 are shown in Figure 5.25. While at point 700 the flow velocities at different water depths have almost the same flow direction, at point 500 a mild variation of the flow direction over the water depth can be observed. This variation can be attributed to the drifting of the ADCP device which triggers non-homogeneity along the water depth. The spreading might indicate the presence of secondary currents as well, bearing in mind the complicated flow field in this zone, as presented in the sections before.

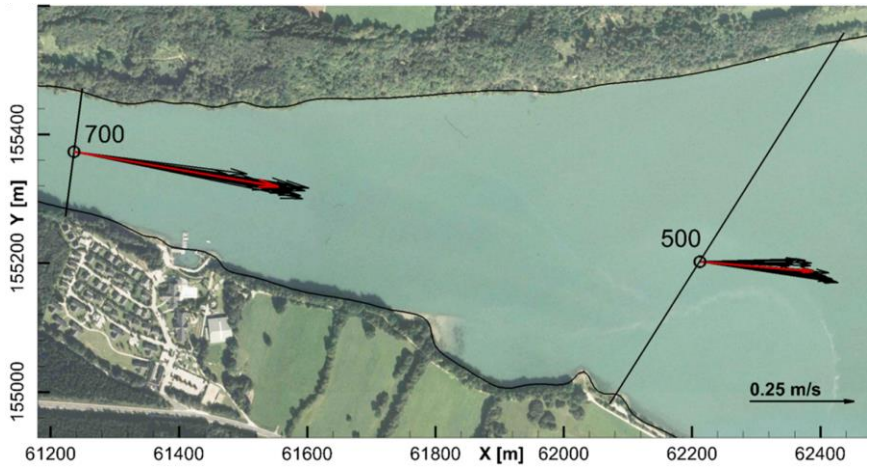

Figure 5.25: Time-averaged velocity vectors at different water depths (black) and depth-averaged velocity vector (red) at the georeferenced measuring points 700 and 500

5.8.3 Bed shear stress and roughness height

The bed shear stress and roughness height have been estimated based on the logarithmic law of the wall for hydraulic rough flow conditions and the explanations given in section 3.3.5. For the linear regression analysis two variants have been tested regarding the choice of the boundary layer thickness. In the first variant the boundary layer thickness has been assumed to correspond to the water depth and consequently, all the velocity data could be used for the analysis. In the second variant the boundary layer thickness has been set equal to the first 20 % of the water depth above the bottom. The second approach is more justified since it is generally supposed that the logarithmic law of the wall is inherently valid only in the first 20 % of the water depth, namely in the wall region (Nezu and Nakagawa, 1993). The latter approach has the disadvantage, especially when using data from ADCP measurements, that usually only a few ADCP cells are available for the regression analysis, bearing in mind that data measured in the first 6 % (for RDI Rio Grande ADCP) water column above the bottom have to be disregarded as well. In this case one could question the statistical significance of the regression analysis and the validity of the method itself. Figure 5.26 and Figure 5.27 show the vertical distribution of the instantaneous velocity magnitudes and the mean velocity magnitudes at the measuring positions 700 and 500. At both measuring positions within the wall region the velocity data from four points have been available for the regression analysis. The blue line represents the calculated logarithmic fit based on the regression analysis by means of the velocities from the four points. The visual inspection indicates a rather good match of the logarithmic law of the wall in the zone near the bottom. The linear fits of both the approaches for the positions 700 and 500 are shown in Figure 5.28 and Figure 5.29, with the y-axis displayed in natural logarithmic scale. At point 700 the linear regression gives very similar relations for the two assumptions of the boundary layer thickness. At point 500 the vertical distribution of the measured velocity data within the wall region differs significantly from the velocity distribution just outside of the wall region. This result points out that in such a case only the velocity data from inside the wall region should be adopted for the estimation of bed shear stress and roughness height.

The calculated results for the bed shear stresses τ_b and roughness heights are listed in Table 5.7. For the conversion of the equivalent roughness height k_s to the Strickler roughness value k_{st} the relation for the dimensionless friction coefficient in (2.32) and the Keulegan relation in (2.33), explained in section 2.2.2, have been used. At position 700 both the assumptions for the boundary layer thickness yield very similar bed shear stresses τ_b with a mean value of around 0.95 N/m². At point 500 the calculated bed shear stresses of 0.71 N/m² and 0.22 N/m² differ significantly. Based on the explanations given above, the latter value seems to be more plausible, which has been determined by means of the velocities from inside the 20 % wall region. The estimated roughness heights k_s differ significantly depending on the assumption for the boundary layer thickness. The comparison of just the lower values, k_s = 0.07 m at point 700 and k_s = 0.08 m at point 500, with the median grain size diameters d_{50}, measured in the range from $1.5 \cdot 10^{-4}$ m to $3.5 \cdot 10^{-4}$ m (Figure 4.7 in section 4.1.2), yields a factor of larger than 200 between k_s and d_{50}. Reflecting the commonly used relationship of $k_s = 3 \cdot d_{50}$ for flat beds (Van Rijn, 1984), the here determined considerably larger factor could be attributed to the possible presence of bed forms. However, the development of bed forms in such bed material conditions, by considering the measured fine

grain sizes, should be questioned. Another more likely reason for the discrepancy might be the fundamental uncertainty in estimating the roughness height by means of the log-law method if only very limited data are available near the bottom. Consequently, but as a valuable result, the Strickler roughness k_{st} with estimated values of around 40 $m^{1/3}/s$ can be seen as the lower range to be used in 2D or 3D numerical models of the reservoir.

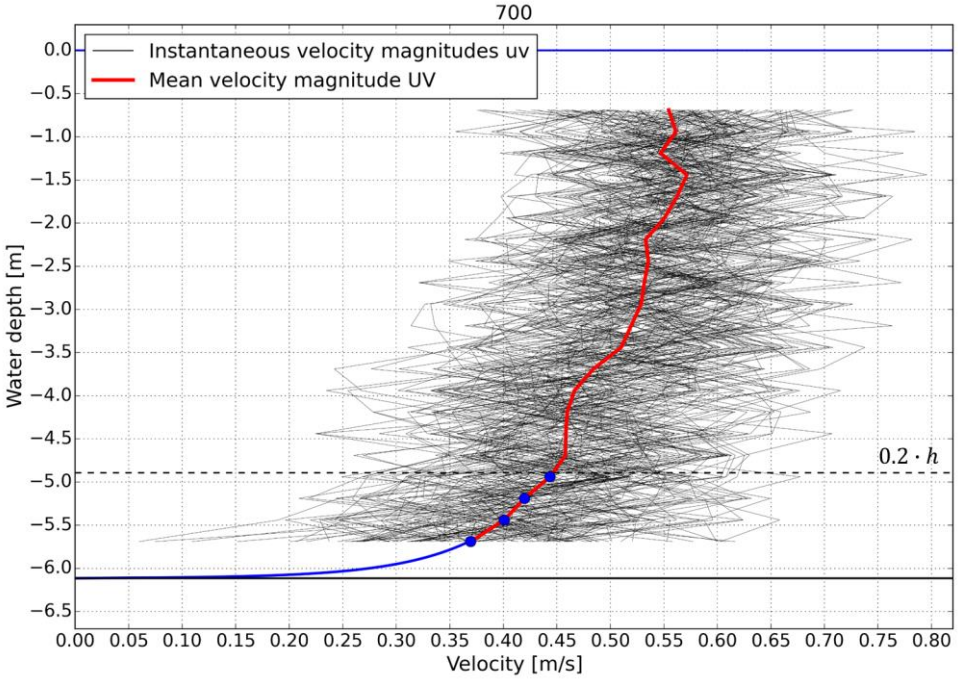

Figure 5.26: Point 700: Mean velocity UV and instantaneous velocity magnitudes

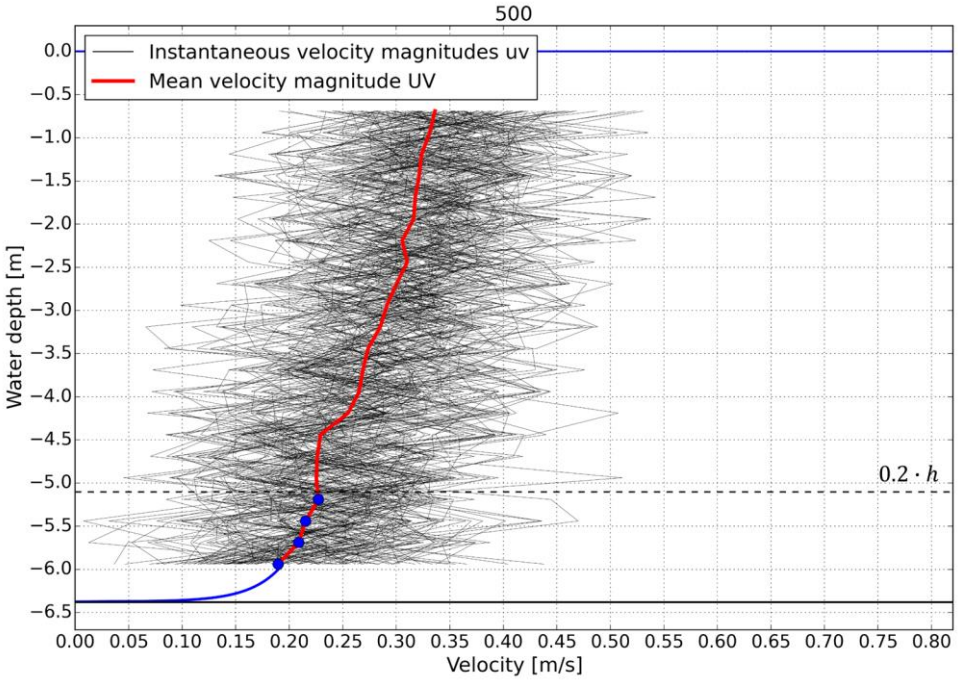

Figure 5.27: Point 500: Mean velocity UV and instantaneous velocity magnitudes

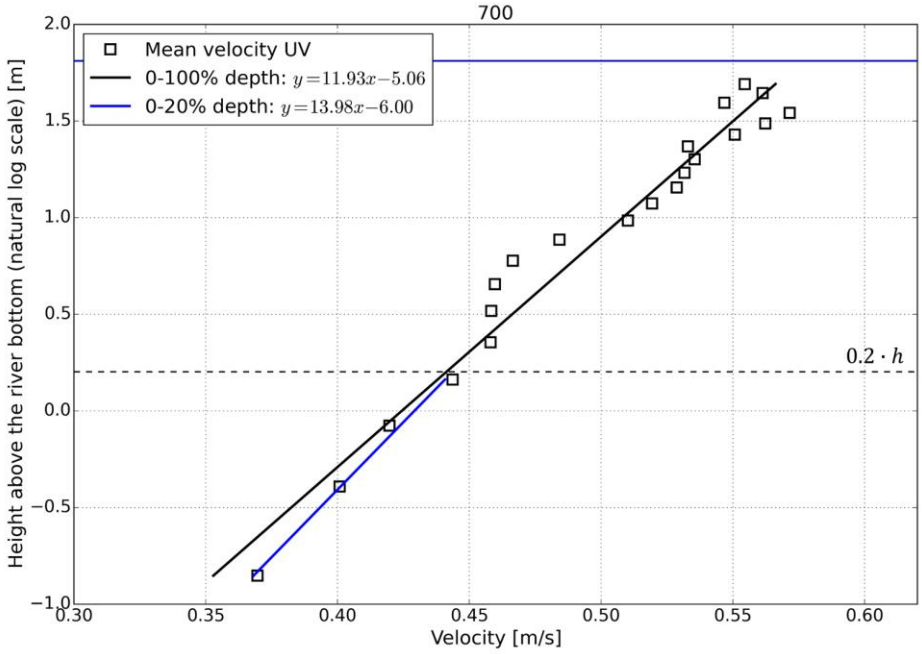

Figure 5.28: Point 700: regression analysis by adopting two different ranges for the logarithmic layer

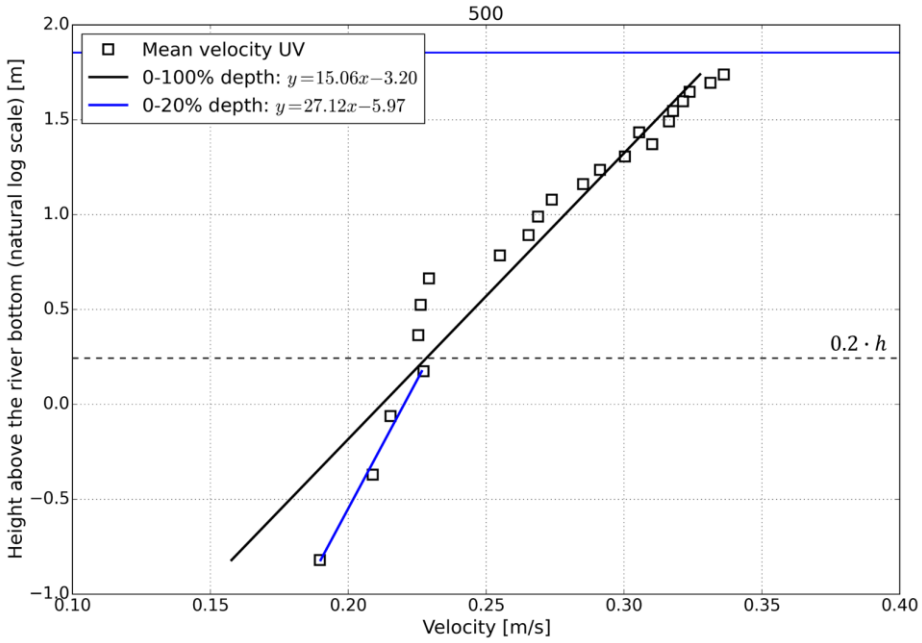

Figure 5.29: Point 500: regression analysis by adopting two different ranges for the logarithmic layer

Measurement point	**700**		**500**	
Range of regression	0-100 %	0-20 %	0-100 %	0-20 %
τ_b **[N/m²]**	1.12	0.82	0.71	0.22
k_s **[m]**	0.19	0.07	1.23	0.08
k_{st} **[m$^{1/3}$/s]**	34	41	23	40
R^2	0.96	0.99	0.93	0.98

Table 5.7: Estimated bed shear stresses and roughness heights at measuring points 700 and 500

5.8.4 Turbulent kinetic energy (TKE)

The turbulent kinetic energy k or TKE is a direct measure of the intensity of turbulent fluctuations which describe the mean kinetic energy of eddies in turbulent flow. The turbulent velocity fluctuations or the mean turbulent normal stresses can be quantified by the measured root mean square velocity fluctuations or the average variances, respectively:

$$k = \frac{1}{2}\left(\overline{u_i' u_i'}\right) = \frac{1}{2}\left(\overline{u_x'^2} + \overline{u_y'^2} + \overline{u_z'^2}\right) \tag{5.1}$$

where u_i' is the instantaneous velocity component in the direction i with i representing the x, y and z direction in the Cartesian coordinate system. The average variance of the velocity fluctuations at a given water depth in each direction i is calculated as follows:

$$\overline{u_i'^2} = \frac{1}{N}\sum_{i=1}^{N}(u_i - U_i)^2 \tag{5.2}$$

where N is the number of the measured velocities u_i along the time axis and U_i is the mean velocity component in the direction i. It has to be remembered that the TKE method in equations (5.1) and (5.2) postulates instantaneous homogeneity of the velocity fluctuations.

The evaluation of the turbulent kinetic energy has been performed by means of the ADCP data from the measuring point 700. The measuring point 700 can be considered to be situated in a rather straight river reach where unidirectional flow prevails. Thus, the subsequent comparison with relationships from the literature could be realized.
Figure 5.30 exemplifies the measured ADCP velocities u_i in x-direction over the measuring time, the calculated mean velocity U_i and the standard deviation $\sqrt{\overline{u_i'^2}}$ of the turbulent velocity fluctuations at point 700 at a water depth of 3 m.

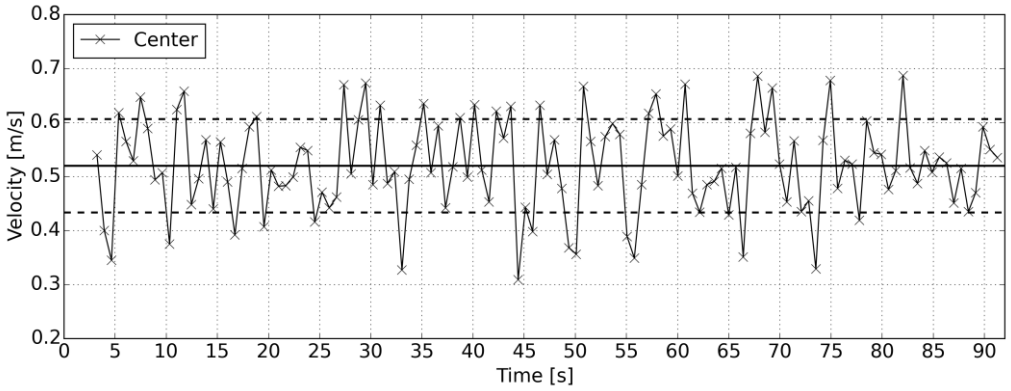

Figure 5.30: Time series of velocities in x-direction at 3 m water depth at measurement position 700; mean velocity (continuous line) and standard deviation of velocity fluctuations (dashed lines)

The recorded ADCP velocity data are affected by instrument noise. The instrument noise consists in part of the Doppler noise which results from errors in measuring the frequency change or phase shift of the reflected pulse. The Doppler noise depends on several factors, like the operational mode, cell size or processing scheme. Flow conditions such as shear and turbulence as well as the ringing effect also affect the noise level of ADCPs (Nystrom et al., 2007). For the estimation and removing of the instrument noise different procedures have been proposed in the literature (Stacey et al., 1999, Williams and Simpson, 2004, USGS, 2006).

For the presented investigation the procedure by the USGS (2006) has been used since it is a simpler method compared to the others referenced above. Furthermore, this method is also suitable for ADCP velocity data which were recorded relative to earth coordinates. In the USGS method it is assumed that at some water depth within the water column, the contribution of the variance of a velocity component to the turbulent kinetic energy is zero. Following this hypothesis, for every velocity component the minimum variance appearing within the water column is subtracted from the variance as calculated for the raw velocity components, as given by equation (5.3). The second term in equation (5.3) represents the variance due to instrument noise. The calculated turbulent kinetic energy k from the ADCP data, corrected by the estimated instrument noise, is then given by equation (5.4).

$$\overline{u'_{i,corr}}^{\,2} = \overline{u_i'^{\,2}} - min\left(\frac{1}{N}\sum_{i=1}^{N}(u_i - U_i)^2\right) \tag{5.3}$$

$$k = \frac{1}{2}\left(\overline{u'_{x,corr}}^{\,2} + \overline{u'_{y,corr}}^{\,2} + \overline{u'_{z,corr}}^{\,2}\right) \tag{5.4}$$

The correction method for instrument noise has a distinct influence on the computed turbulent kinetic energies along the water depth, as Figure 5.31 demonstrates. The corrected TKE values (TKE corrected) are significantly lower than the TKE values calculated from the raw ADCP data.

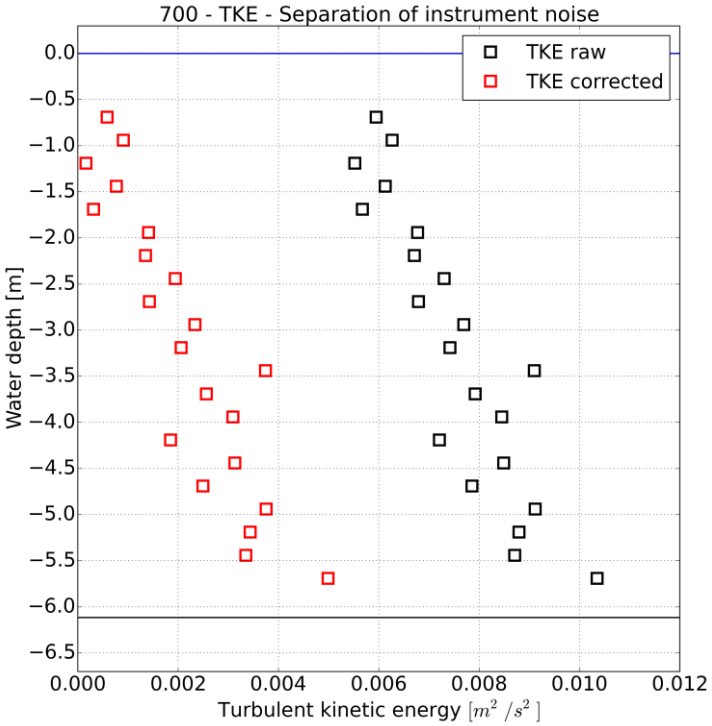

Figure 5.31: Turbulent kinetic energy over the water depth at point 700, separation of instrument noise

The measured (corrected) turbulent kinetic energies along the water depth have been compared with two relations proposed in the literature. Both approaches relate the turbulent kinetic energy k to the bed shear stress τ and the shear velocity U^*. The semi-empirical exponential law proposed by Nezu and Nakagawa (1993) is based on measurements in straight open channel flows and is given in equation (5.5). The second relation, given in equation (5.6), originates from the wall boundary condition of k, proposed by Rodi (1984) for the k-ε turbulence model. It simply assumes a linear decrease of the turbulent kinetic energy, starting from the wall boundary condition towards the water surface with k being zero at the surface. In relation (5.6) c_μ is an empirical constant used in the k-ε turbulence model with the generally adopted value of 0.09.

$$\frac{k}{U^{*2}} = 4.78\, e^{\left(-\frac{2z}{h}\right)} \tag{5.5}$$

$$\frac{k}{U^{*2}} = \frac{1}{\sqrt{c_\mu}}\left(1 - \frac{z}{h}\right) \tag{5.6}$$

For the comparison of the ADCP derived TKE with the relations given above, the bed shear stress evaluated by means of the log-law method has been used (Table 5.7), with the mean value rounded to τ_b = 0.95 N/m². The comparison, shown in Figure 5.32, reveals a remarkably good agreement in terms of magnitudes of TKE between the measured ADCP data and the relations in (5.5) and (5.6).

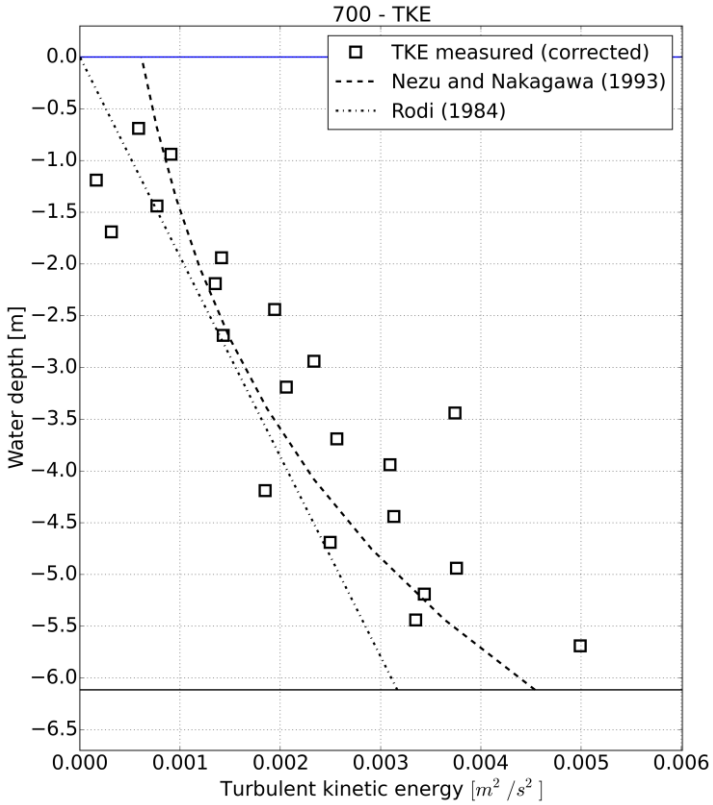

Figure 5.32: Comparison of measured TKE along the water depth with relations from Nezu and Nakagawa (1993) and Rodi (1984), τ_b = 0.95 N/m²

The results indicate the validity of the noise subtraction method by USGS (2006) for estimating the turbulent kinetic energy based on measured ADCP data. The analysis of the turbulent kinetic energy and the comparison with literature confirm the range of magnitude of bed shear stresses obtained by the log-law method, at least in this case. Furthermore, the comparison evidences the applicability of the semi-empirical relations, proposed by Nezu and Nakagawa (1993) as well as Rodi (1984), for the use as upstream boundary conditions for turbulent kinetic energy in 3D numerical models of reservoir-like flows.

5.8.5 Estimation of bed shear stress by means of the TKE method

Several studies have shown that from the estimate of turbulent kinetic energy k the turbulent shear stress τ within the water column can be estimated by the following relation:

$$\tau = C \cdot \rho \cdot k \tag{5.7}$$

The constant C was found to be around 0.20 (Soulsby, 1981) or 0.19, with the latter value adopted in later publications (Kim et al., 2000, Biron et al., 2004). In the presented study for the estimation of the bed shear stress τ_b the value of C = 0.19 and a water density of ρ = 1000 kg/m³ have been applied.

Above the river bottom and outside the range of 6 % of the total water depth the first valid measured value of turbulent kinetic energy k, corrected by instrument noise, is 0.005 m²/s² (Figure 5.32). Inserting this value in equation (5.7), the bed shear stress τ_b is calculated as 0.95 N/m². This resulting value corresponds almost to the mean bed shear stress obtained by the log-law method. USGS (2006) argued that the first valid measured TKE value might be still affected by the much stronger echo signal coming from the river bottom. Thus, they smoothed out possible spikes by averaging the measured turbulent kinetic energies from the subset of cells between 6 and 10 % of the water depth above the bottom. In the presented case the averaging of the two k values from near the bottom yields a mean TKE value of 0.0042 m²/s². Equation (5.7) yields a bed shear stress of 0.80 N/m² by using this mean value. Table 5.8 shows the comparison of the calculated bed shear stresses, obtained by the log-law method and the TKE method, respectively.

Bed shear stress τ_b	**Log-law method**		**TKE method**	
Range of regression / TKE points	0-100 %	0-20 %	1 point	2 points average
τ_b [N/m²]	1.12	0.82	0.95	0.80

Table 5.8: Calculated bed shear stresses by means of the log-law method and the TKE method

High peaks in the TKE values measured near the bottom indicate the presence of bed forms USGS (2006). The very good agreement between the bed shear stresses estimated by means of the log-law method and the TKE method demonstrates that no larger bed forms are present at measuring point 700. This finding is comprehensible when considering the measured fine grain size distribution at this location.

The investigations demonstrate that the log-law method and the TKE method yield physically plausible estimates of bed shear stress in the presented case. The comparative study evidences the applicability of ADCP measurements for the estimation of bed shear stress and turbulent kinetic energy in reservoirs.

5.9 Summary

In the prototype five ADCP moving-boat velocity measurements were carried out at predefined cross sections. Two of them were carried out before and three campaigns after installation of the groyne in the prototype. In the ADCP campaigns the developing large-scale flow fields could be determined. The ADCP measurements are able to capture very sharp horizontal shear layers with abrupt transitions between downstream and upstream flow. The measured crosswise recirculations and flow redistributions indicate the presence of strong secondary currents. The field measurements replicate the physical model experiments and evidence the impact of the non-submerged groyne on the developing flow field. In the physical model and in the prototype the horizontal shear layers and the zones of transition between downstream and upstream flows impressively are measured at the almost same locations. Though, the field measurements could confirm the physical model results for the cases without and with installation of the groyne, only, if steady flow conditions are present

in the prototype. Repetitive measurements at cross sections and analysis of measured discharges indicate the development of unsteady meandering flow for the case of typical everyday operation of the hydro power plant. These results show also that the implemented groyne has not enough impact to align the flow fields for different flow conditions and to prevent the meandering of the main stream in the reservoir.

In addition to the large-scale flow field measurements, the estimation of bed shear stress, roughness height as well as turbulent kinetic energy in the reservoir by means of two stationary ADCP measurements were investigated. The roughness height was estimated by means of the logarithmic law of the wall. For the estimation of bed shear stress the law of the wall method and the turbulent kinetic energy method were investigated and compared. Both methods yield physically plausible estimates of bed shear stress and turbulent kinetic energy in the reservoir. The comparison with approaches in literature points out the feasibility of these methods to estimate these quantities in reservoir-like flow conditions. Furthermore, the comparison evidences the applicability of the semi-empirical relations, proposed by Nezu and Nakagawa (1993) as well as Rodi (1984), for the use as upstream boundary conditions for turbulent kinetic energy in 3D numerical models of reservoir-like flows.

6 Numerical Simulations

6.1 Overview

This chapter presents the 3D and 2D depth-averaged numerical simulations of the case study. The aim of the research was to analyse the impact of the different physical and numerical parameters on the resulting flow fields in the reservoir. The investigations focused especially on the computed expansion flow phenomena in terms of main stream development.

The 3D simulation studies focused on the investigation of the following parameters:

- Bottom roughness
- Turbulence model
- Hydraulic boundary conditions; steady simulations
- Hydrostatic / Non-hydrostatic pressure assumption
- Installation of the non-submerged groyne

In the 2D depth-averaged simulations the following parameters were examined:

- Bottom roughness
- Turbulence model, with focus on the depth-averaged Mixing Length model
- Hydraulic boundary conditions; steady and unsteady simulations
- Geometrical design of the inflow zone
- Installation of the non-submerged groyne

In the numerical parameter studies it was not primary aim to combine simulation parameters or setups in a way in order to match the ADCP field measurements or physical model results of the developing complex flow fields in the reservoir. Hence, the 3D and 2D steady simulations are not compared explicitly to the field and experimental results, albeit the numerical models could reproduce the measured large-scale flow behaviours for some hydraulic load cases. In the 3D simulations further investigations have been performed in order to analyse the three-dimensionality of the flow. Section 6.5 presents the comparison of 2D unsteady simulations with two ADCP measurement campaigns for the cases before and after implementation of the groyne in the prototype. The 3D and 2D numerical results are presented generally in plan view by means of the depth-averaged flow velocities.

6.2 Mesh generation and hydraulic boundary conditions

The unstructured triangular two-dimensional mesh was generated with the free software Blue Kenue (CHC, 2011). A constant triangle edge length of 10 m was used for the entire modelling domain. The resulting 2D horizontal mesh is composed of about 19900 nodes and 39000 elements. The digital elevation model 2007 served as basis for the bottom elevations which were linearly interpolated to the mesh nodes. For the 3D numerical simulations the

three-dimensional mesh was generated by replicating the 2D mesh over the vertical. The structured grid in the vertical was created by specifying equally distributed layers over the water depth by the application of a terrain-following sigma transformation. In all 3D simulations presented hereafter the number of vertical layers was set to 10.
The inflow zone was extended by 100 m upstream of cross section 700 in order to allow the inflow to develop. The angle of the inflow boundary was defined based on the mean flow direction at cross section 700 measured in the ADCP campaigns. The measured mean flow directions at cross section 700 were almost the same in all the ADCP measurement campaigns. Figure 6.1 illustrates the triangular mesh along with the bottom elevations.

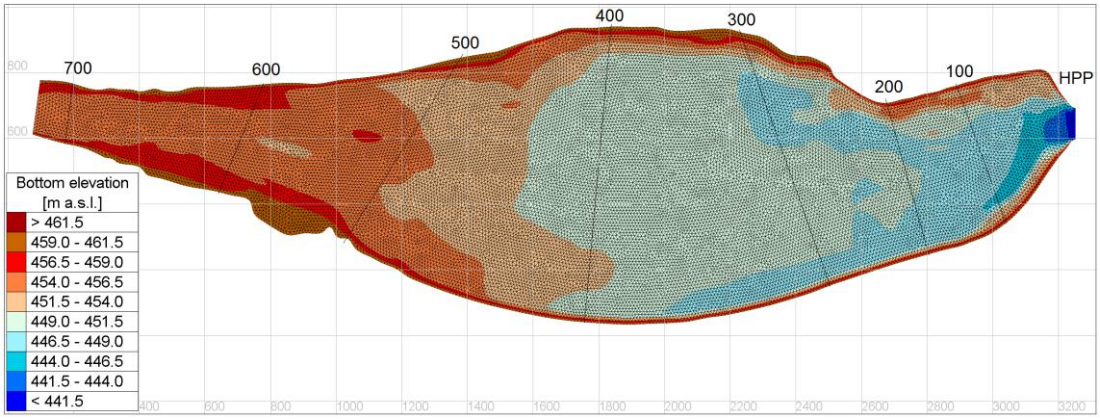

Figure 6.1: Plan view, 2D unstructured triangular mesh

Hydraulic boundary conditions

In the 3D and 2D simulations the same hydraulic boundary conditions were adopted. At the inflow boundary the discharge and at the outflow boundary the water level were imposed. Preliminary studies regarding the outflow boundary at the hydro power plant showed that the location of the open boundary – turbine outflow (weirs closed), weir outflow (turbines closed) or their combined outflow (turbine and weirs open) – doesn't have any influence on the computed flow field in the reservoir. Hence, the location of the outflow boundary condition was simply switched either to turbine outflow or to weir outflow. The open boundary location for weir outflow was used only in the simulations with an imposed discharge of 700 m³/s which represents a reservoir flushing scenario during a smaller flood event. In the steady state simulations the design discharge of 440 m³/s was used by default as upstream hydraulic boundary condition. At the downstream boundary the water level by default was set to 461.5 m a.s.l. which corresponds to the normal operating water level. In the two unsteady simulations the 24 hours flow and water level hydrographs have been applied as hydraulic boundary conditions, which were measured at the hydro power plant on the days of the two ADCP campaigns.
The simulation time was set to 4 days in order to reach a (theoretical) steady state flow field in the reservoir. A start-up time with a linear increase of the inflow was defined in order to prevent too massive oscillations at the beginning of the numerical calculations. The required long simulation time for reaching steady state conditions is explained by the very low flow velocities and the big reservoir volume of about $16.5 \cdot 10^6$ m³ (based on normal operating water level). These two factors cause the oscillations, which typically emerge during the start-up time, to fade away just slowly.

6.3 Telemac-3D simulations

6.3.1 Numerical setup

In the three-dimensional calculations for the advection of the velocities, the turbulent kinetic energy and the dissipation of the turbulent kinetic energy the method of characteristics (MOC) has been used. For the time discretization the default implicitation coefficients for the water depth (0.55) and the velocities (1.0) have been used. The time step was set to 2 seconds. The hydrostatic pressure assumption was applied by default.

The bed resistance was modelled by means of the log-law for rough walls and the Nikuradse's equivalent roughness height k_s. The roughness was assumed to be constant in the entire modelling domain. The default value was set to k_s = 0.02 m which corresponds to a Strickler roughness value k_{st} of about 50 $m^{1/3}/s$. The Mixing Length turbulence model has been applied for the vertical turbulence modelling when using the constant eddy viscosity model for the horizontal turbulence modelling. The constant eddy viscosity was set to a default value of $\nu_{t,h}$ = 0.1 m^2/s for the whole domain. In the Mixing Length model the Nezu and Nakagawa approach has been used for the calculation of the mixing length. Table 6.1 gives an overview about the default model setup and the varied parameters in the study.

3D Parameter Study	Hydraulic boundary conditions	Bottom roughness	Turbulence model
Default setup	Q = 440 m^3/s WL = 461.5 m a.s.l.	k_s = 0.02 m	Vertical: Mixing Length model Horizontal: $\nu_{t,h}$ = 0.1 m^2/s
Bottom roughness	k_s = 0.02 m, k_s = 0.10 m		
Turbulence model	Mixing Length model and $\nu_{t,h}$ = 0.1 or $\nu_{t,h}$ = 0.5 m^2/s k-ε model		
Discharge and water level	Q = 440 m^3/s \ WL = 461.5 m a.s.l. Q = 365 m^3/s \ WL – 1.0 m Q = 700 m^3/s \ WL – 2.5 m		
Pressure assumption	Hydrostatic / Non-hydrostatic pressure assumption		
Installation of the groyne			
Turbulence model	Mixing Length model and $\nu_{t,h}$ = 0.1 m^2/s or $\nu_{t,h}$ = 0.5 m^2/s		
Advection schemes	MOC scheme and k-ε model NERD scheme and k-ε model		

Table 6.1: Overview about the parameter study in the 3D numerical simulations

6.3.2 Parameter study

Bottom roughness

In this variation two different values for the roughness height were investigated: k_s = 0.02 m and as upper limit k_s = 0.10 m. A constant eddy viscosity of $\nu_{t,h}$ = 0.1 m^2/s was assumed for the horizontal turbulence modelling. Figure 6.2 shows the comparison of the two simulation

results. While the lower roughness value of k_s = 0.02 m causes the main stream to develop near the orographic right bank, with the higher roughness value of k_s = 0.10 m the main stream is shifted to the center of the reservoir. In the simulation with k_s = 0.10 m a damping of the general flow field and recirculation zones can be observed.

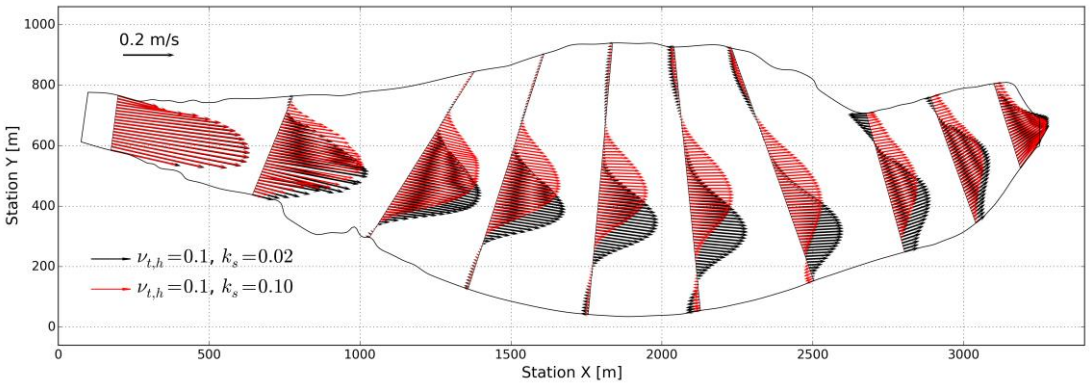

Figure 6.2: Telemac-3D, variation of the equivalent roughness height

Turbulence model

Two different approaches have been investigated for turbulence closure: the constant eddy viscosity model in combination with the Mixing Length model and the k-ε model. In the constant eddy viscosity model for the horizontal turbulence the eddy viscosity coefficient $\nu_{t,h}$ was assumed to be 0.1 m²/s or 0.5 m²/s. As shown in Figure 6.3, both assumptions lead to a similar flow behaviour in the wider area of the reservoir. The main stream is located near the orographic right bank and the backflows takes place near the orographic left bank. Though, the increased eddy viscosity coefficient of 0.5 m²/s causes the general flow field to be distinctively dampened. Furthermore, the higher turbulent diffusion dampens out the smaller scale recirculation zones which develop in the simulations with $\nu_{t,h}$ = 0.1 m²/s. In the simulated flow field by means of the two-equation k-ε turbulence model in the wider area of the reservoir the main stream is located in the center, with up to five alternations of downstream and upstream flow at cross section 400. It has to be said that in the simulation using the k-ε model a completely steady flow field could not be achieved, but a slight meandering of the main stream was calculated in the lower part of the reservoir. The variation of time step or implicitation coefficients didn't change this flow behaviour.

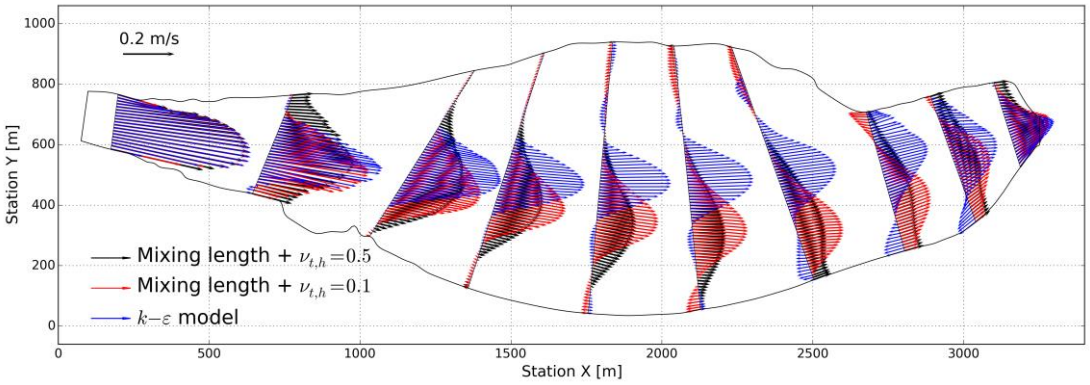

Figure 6.3: Telemac-3D, variation of the turbulence model

Figure 6.4 shows the projected flow velocities in cross section 400 for the simulations with the constant eddy viscosity approach and the k-ε turbulence model. While the plan view in Figure 6.3 doesn't emphasize the very different behaviour of the two turbulence models, the analysis of the flow velocities in the cross section demonstrates it evidently. The constant eddy viscosity approach leads to one expanded main stream in downstream flow direction with two backflow zones on both sides. The k-ε turbulence model computes a compact zone of high flow velocities in downstream direction in the central part of the cross section with backflow zones on both sides. Near the banks again a transition from upstream to downstream flow direction emerges. Even though the computed crosswise flow velocities are very low, the two turbulence models produce remarkably different crosswise velocity directions.

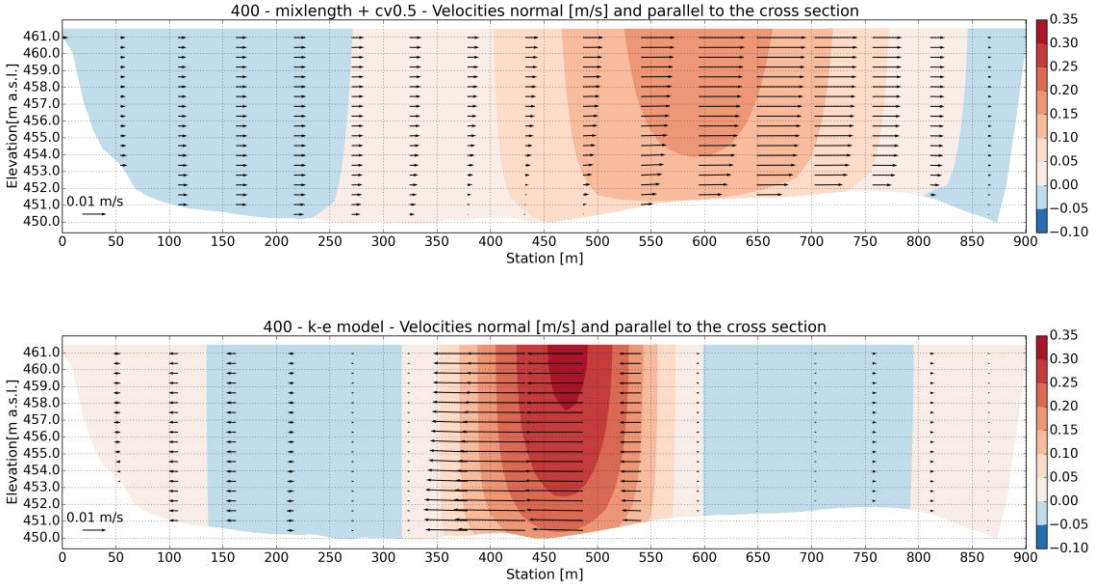

Figure 6.4: Telemac-3D, flow velocities in cross section 400; above: constant eddy viscosity model with $\nu_{t,h}$ = 0.5 m²/s, below: k-ε turbulence model

Discharge and water level

In this study two other scenarios for the hydraulic boundary conditions were simulated and compared with the default setup. In the first variation the inflow was reduced from the default value of 440 m³/s to 365 m³/s and the default water level of 461.5 m a.s.l was lowered by one meter at the outlet. These boundary conditions correspond to the mean values measured in the second ADCP measurement campaign. In the second variation a smaller flood event was simulated by increasing the discharge to 700 m³/s and by lowering the default water level by 2.5 m at the outflow boundary. This scenario should represent a reservoir flushing. The equivalent roughness height and the constant eddy viscosity were again set to k_s = 0.02 m and $\nu_{t,h}$ = 0.1 m²/s, respectively.

Compared to the default setup in both variations the main stream gets shifted towards the center in the wider area of the reservoir, as shown in Figure 6.5. In the second variation with a lowered water level of 2.5 m the main stream is located in the center of the reservoir. The main triggering mechanism can be attributed to the lowering of the water level at the outlet. The lower water level in the reservoir causes the forming of very shallow or even dry areas

at the orographic right bank in the area close downstream to the inlet. Thus, in this area the effective flow section is shifted away from the orographic right bank which has the apparent effect of changing the main flow direction. Other simulated variants which are not shown here, specifically the lowering of only the water level at the outlet while imposing the design discharge at the inlet, demonstrated the same flow behaviour.

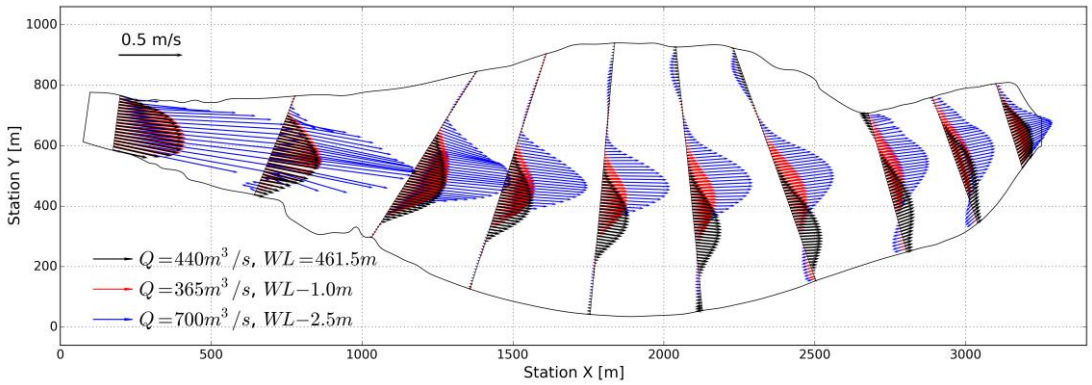

Figure 6.5: Telemac-3D, variation of discharge and water level

Non-hydrostatic pressure assumption

This variation investigated if the application of the non-hydrostatic pressure assumption has an overall impact on the results and if it leads to an enhanced development of secondary currents effects and associated flow redistributions. In the simulation normal turbine operation was simulated by applying the default values of Q = 440 m³/s and WL = 461.5 m a.s.l. as hydraulic boundary conditions. The roughness value was set to 0.02 m and for the horizontal turbulence the constant eddy viscosity value of $\nu_{t,h}$ = 0.1 m²/s was used. The Mixing Length model was applied for the vertical turbulence. Figure 6.6 shows the simulation results employing the hydrostatic and the non-hydrostatic pressure assumption. The comparison demonstrates that almost identical depth-averaged flow velocity distributions are computed with both the pressure assumptions.

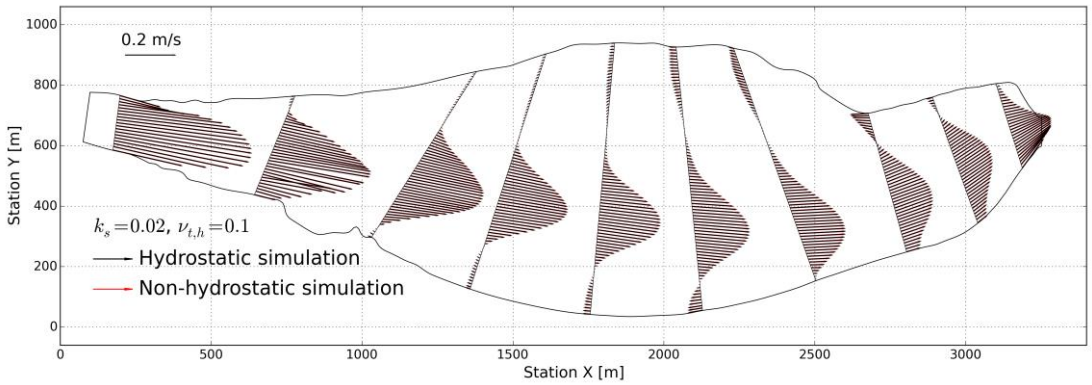

Figure 6.6: Telemac-3D, hydrostatic versus non-hydrostatic pressure assumption

For the analysis of the local secondary flow intensity the absolute angle φ between the computed surface vector $\vec{u}_{ws}$ and bottom vectors $\vec{u}_{bed}$ has been calculated by means of the following equation:

$$\varphi = \cos^{-1}\left(\frac{\vec{u}_{ws} \cdot \vec{u}_{bed}}{|\vec{u}_{ws}| \cdot |\vec{u}_{bed}|}\right) \tag{6.1}$$

Figure 6.7 shows the calculated spatially distributed secondary flow intensities in the reservoir for the simulated cases of hydrostatic and non-hydrostatic pressure assumption. The comparison demonstrates that the assumption of hydrostatic or non-hydrostatic pressure doesn't yield any remarkable differences in the secondary current intensities. The highest intensities are computed mainly in the horizontal shear zones where the upstream and downstream flow directions alternate. Along these shear zones pronounced intensities with angles larger than 120° deg can be observed, however, their crosswise widths are very limited.

The analysis of the secondary flow intensities by means of the presented method reveals that the overall three-dimensionality of the flow behaviour and the three-dimensional flow redistributions in the reservoir, computed by Telemac-3D, in general are only weak. This result suggests that the flow phenomena developing in the reservoir, at least the numerically simulated large-scale flow behaviour, can be resolved by means of the 2D depth-averaged shallow water equations.

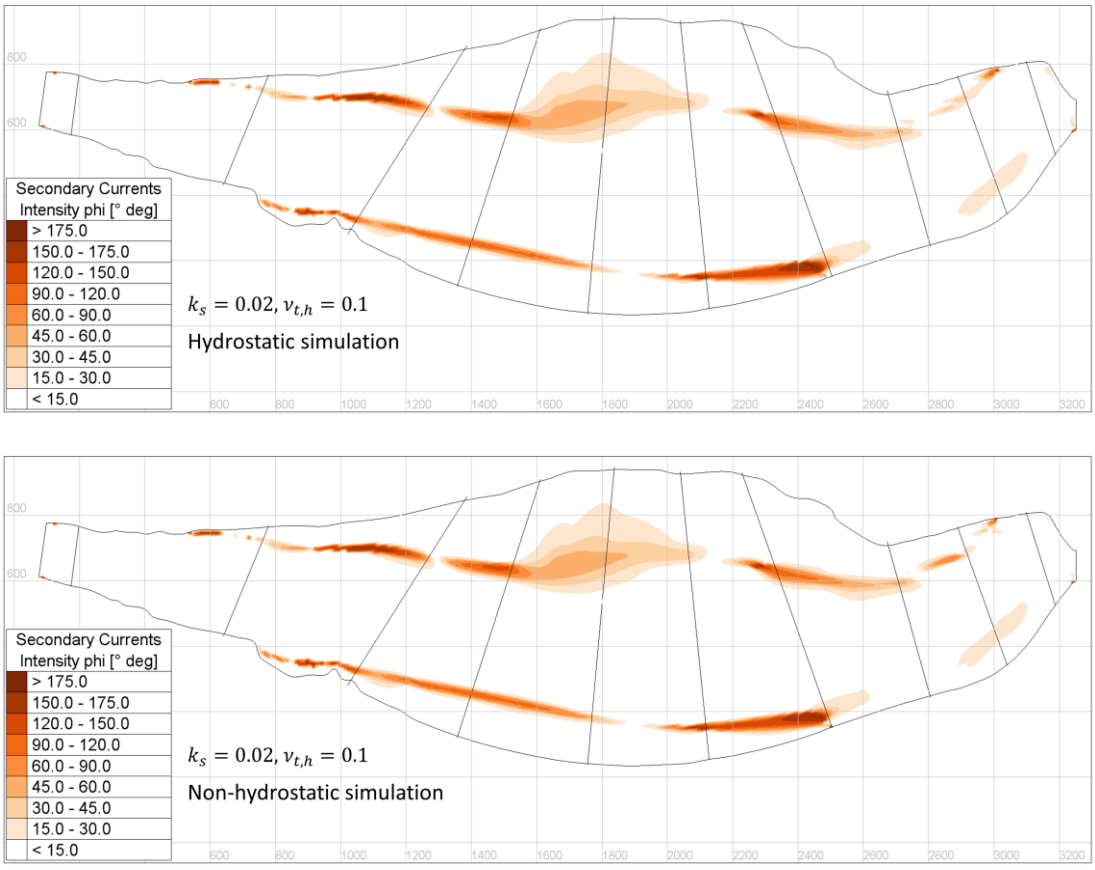

Figure 6.7: Telemac-3D, secondary flow intensities; above: hydrostatic pressure assumption, below: non-hydrostatic pressure assumption

6.3.3 Installation of the groyne

This study investigated the impact of the installed non-submerged groyne on the simulated flow field in the reservoir. In the numerical model the 70 m long non-submerged groyne was installed at cross section 600 by blocking out the corresponding mesh elements and refining the mesh around the virtual groyne (Figure 6.8).

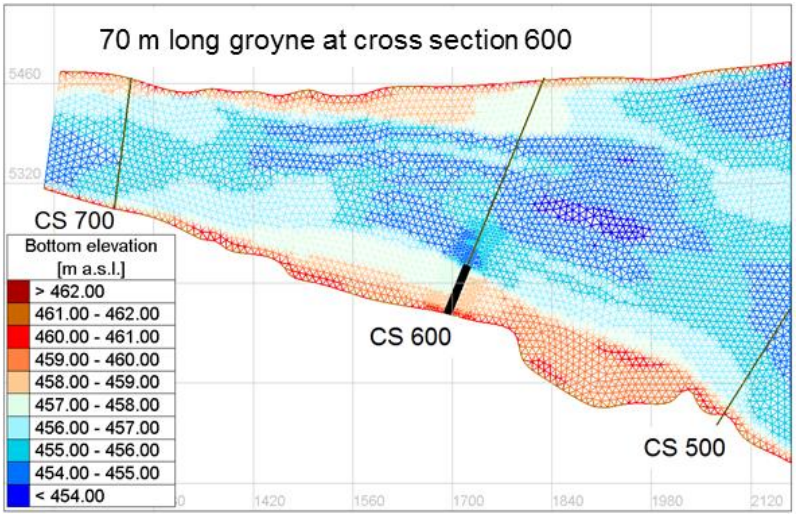

Figure 6.8: Plan view, non-submerged groyne at cross section 600

In the simulations for the hydraulic boundary conditions the default setup values of Q = 440 m³/s for the inflow condition and WL = 461.5 m a.s.l. for the outflow condition were adopted. The Nikuradse's roughness value was set to k_s = 0.02 m. In the first variation the Mixing Length model was applied for the vertical turbulence modelling, whereas for the horizontal turbulence modelling the constant eddy viscosity coefficient was set to $\nu_{t,h}$ = 0.1 m²/s or $\nu_{t,h}$ = 0.5 m²/s. In the second variation, additionally to the default advection scheme, namely the method of characteristics (MOC), the so called N-scheme for tidal flats (NERD) was tested for the advection of velocities and turbulent quantities. In both simulations the k-ε turbulence model was used.

The two 3D numerical results from the first variation, which differ in the assumption of the constant eddy viscosity coefficient, are shown in Figure 6.9. In both simulations the non-submerged groyne causes the main stream to be shifted towards the orographic left bank. Compared to the results without the installation of the groyne, shown in Figure 6.3, the developing flow field in the wider area of the reservoir behaves completely different.
Figure 6.10 shows the two numerical results from the second variation. In the simulation with the default advection scheme (MOC) the non-submerged groyne doesn't have a major influence on the resulting flow field, compared to results shown in Figure 6.3. The NERD scheme computes a noticeable different flow field compared to the MOC scheme, with the main stream developing more closely to the orographic left bank in the reservoir.

The results from the variation of the advection schemes should emphasize that in this case study the numerically simulated flow field is not only very sensitive to the chosen physical parameters, but apparently, also to the used numerical discretization scheme.

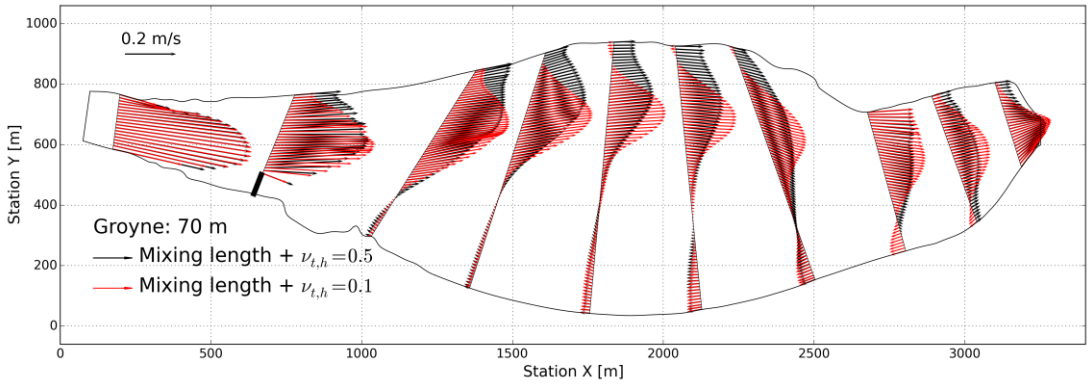

Figure 6.9: Telemac-3D, installation of the groyne, variation of the constant eddy viscosity for the horizontal turbulence modelling

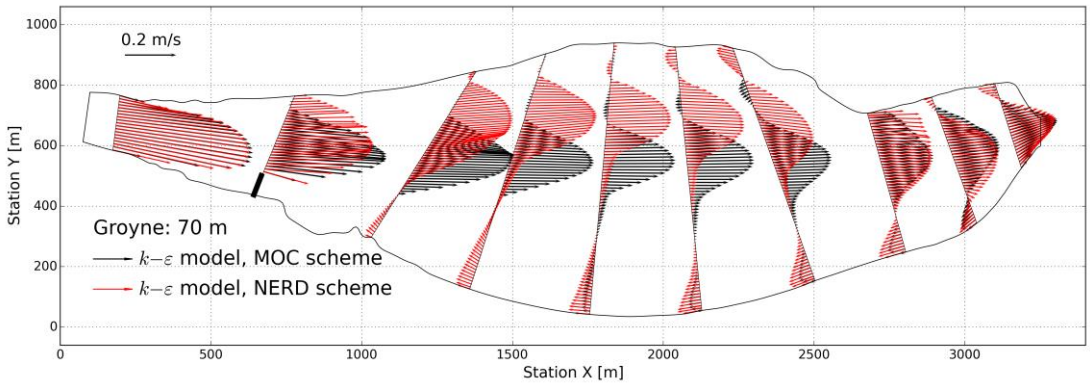

Figure 6.10: Telemac-3D, installation of the groyne, k-ε model, variation of the advection scheme

6.4 Telemac-2D simulations

6.4.1 Numerical setup

In the two-dimensional calculations for the advection of the velocities the method of characteristics in combination with the wave equation algorithm has been used. For the advection of the turbulent quantities k and ε in the k-ε model the method of characteristics has been applied as well. For the time discretization the default implicitation coefficients for the water depth (0.55) and the velocities (0.55) have been used. Based on preliminary tests, the time step was set to 5 seconds.

The bed resistance was computed by means of the Strickler's friction law. The Strickler value was set to k_{st} = 50 m$^{1/3}$/s by default. When using the newly implemented depth-averaged Mixing Length turbulence model, if not otherwise specified, the semi-empirical coefficients appearing in the model have been set to the default values of $\alpha_t = \kappa/6 \approx 0.067$ and $l_m = 4/15\kappa h \approx 0.11h$.

The varied physical and numerical parameters in the 2D numerical parameter study are provided in the overview in Table 6.2.

2D Parameter Study	Hydraulic boundary conditions	Bottom roughness	Turbulence model
Default setup	Q = 440 m³/s WL = 461.5 m a.s.l.	k_{st} = 50 m$^{1/3}$/s	-
Bottom roughness	k_{st} = 50, 55 and 60 m$^{1/3}$/s		Constant eddy viscosity model ν_t = 0.5 m²/s
Turbulence model 1	Constant eddy viscosity model: ν_t = 0.1, 0.5 and 1.0 m²/s		
Turbulence model 2	Elder model, k-ε model and Mixing Length model with $\alpha_t = 0.067$ and $l_m = 0.11h$		
Mixing Length turbulence model 1	$\alpha_t = 0.067$ and $l_m = 0.5h$ $\alpha_t = 1.0$ and $l_m = 0.5h$		
Mixing Length turbulence model 2	$\alpha_t = 0.067$ and $l_m = 0.5h$ $\alpha_t = 0.067$ and $l_m = 1.0h$ $\alpha_t = 0.067$ and $l_m = 2.0h$		
Mesh resolution	39021 mesh elements vs. 156084 mesh elements		Mixing Length model $\alpha_t = 0.5$ and $l_m = 1.0h$
Inflow zone	Repositioning of inflow boundary		Mixing Length model $\alpha_t = 0.5$ and $l_m = 1.0h$
Discharge and water level	Q = 440 m³/s \ WL = 461.5 m a.s.l. Q = 365 m³/s \ WL – 1.0 m Q = 700 m³/s \ WL – 2.5 m		Mixing Length model $\alpha_t = 0.5$ and $l_m = 1.0h$
Installation of the groyne			
Discharge and water level	Q = 440 m³/s \ WL = 461.5 m a.s.l. Q = 700 m³/s \ WL – 2.5 m		Mixing Length model $\alpha_t = 0.5$ and $l_m = 1.0h$
Length of groyne	70 m vs. 100 m long non-submerged groyne		Mixing Length model $\alpha_t = 0.5$ and $l_m = 1.0h$
Unsteady simulations			
ADCP campaign 2 (before installation of groyne)	24 h flow and stage hydrograph	k_{st} = 50 m$^{1/3}$/s	Mixing Length model $\alpha_t = 0.5$ and $l_m = 0.5h$
ADCP campaign 5 (after installation of groyne)	24 h flow and stage hydrograph	k_{st} = 50 m$^{1/3}$/s	Mixing Length model $\alpha_t = 0.5$ and $l_m = 0.5h$

Table 6.2: Overview about the parameter study in the 2D numerical simulations

6.4.2 Parameter study

Bottom roughness

In this variation three different Strickler roughness values were investigated: k_{st} = 50 m$^{1/3}$/s, k_{st} = 55 m$^{1/3}$/s and k_{st} = 60 m$^{1/3}$/s. For turbulence closure the constant eddy viscosity model was used by applying a constant eddy viscosity coefficient of ν_t = 0.5 m²/s for the whole domain. This value for the constant eddy viscosity represents a typical magnitude in 2D depth-averaged river flow simulations.

Figure 6.11 demonstrates the quite remarkable results in terms of simulated flow fields in the reservoir, depending on the applied roughness value. The lowest roughness value of k_{st} = 50 m$^{1/3}$/s causes the main stream to be located at the orographic left bank. By increasing the roughness value slightly to k_{st} = 55 m$^{1/3}$/s, the flow field changes completely

in the wider area of the reservoir. The simulation by means of the roughness value of k_{st} = 60 m$^{1/3}$/s results in the same flow behaviour compared to the latter one. The comparison demonstrates the obvious behaviour that the damping of the flow field increases with the decrease of the Strickler roughness value.
The study emphasizes that the variation of only the bottom roughness value within a physically plausible but narrow range can have a massive impact on the resulting simulated flow field. The entire flow behaviour in the wider area of the reservoir is sensitive not only to the geometrical characteristics but greatly to the adopted bottom roughness value, too.

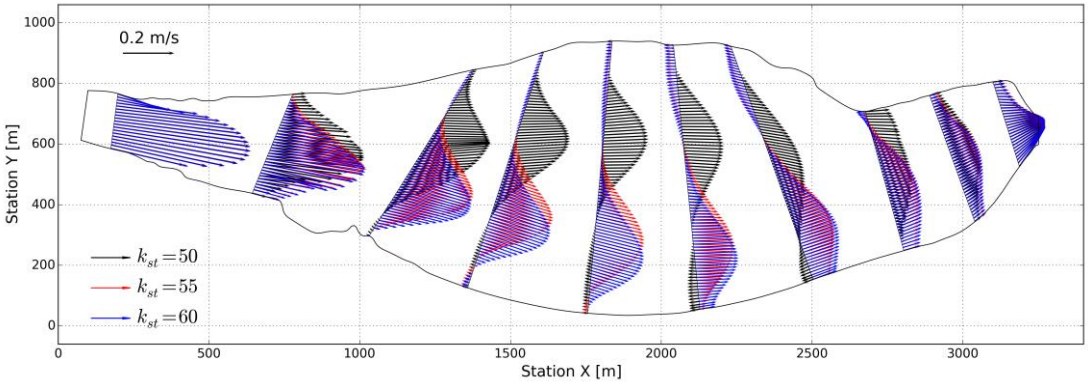

Figure 6.11: Telemac-2D, variation of the Strickler roughness value

Turbulence model

For the investigation of the influence of the chosen turbulence model on the simulated flow field in the reservoir four turbulence models, which are commonly used in numerical models for river flows, have been compared: the constant eddy viscosity model, the Elder model, the depth-averaged k-ε model and the newly implemented depth-averaged Mixing Length model. In the simulation the Strickler bottom roughness value was set to k_{st} = 50 m$^{1/3}$/s.
In the constant eddy viscosity model the eddy viscosity coefficient ν_t was assumed to be 0.1, 0.5 or 1.0 m²/s. These values lie in the typical range of depth-averaged river flow simulations. In the Elder turbulence model the default coefficients for the longitudinal and transversal dispersion have been used. Special focus has been given on the Mixing length turbulence model and the variation of its semi-empirical coefficients α_t for the vertical turbulence generation and the assumption for the mixing length l_m in the horizontal turbulence generation term.

The simulation results obtained by means of the constant eddy viscosity model and the variation of the coefficients ν_t are shown in Figure 6.12. The decrease of the eddy viscosity coefficient from ν_t = 1.0 to 0.1 m²/s leads to successive shift of the main stream from the orographic left bank to the center of the reservoir. The comparison demonstrates clearly the impact of the chosen magnitude for the eddy visocity on the resulting simulated flow field in the reservoir. Furthermore, the results show that the use of higher viscosities dampens out potentially occurring recirculation zones.
The results simulated by means of "advanced" turbulence models, namely the Elder model, the depth-averaged k-ε model and the depth-averaged Mixing Length model, are shown in Figure 6.13. All three turbulence models yield similar computed flow fields in the reservoir.

In the wider area of the reservoir the main stream is located compactly in the center with backflow zones at both sides. The results match quite well the computed flow field obtained by the constant eddy viscosity model and the eddy viscosity coefficient ν_t having a value of 0.1 m²/s. It has to be mentioned that by using the k-ε model, and even more, by using the Mixing Length model no real steady state flow conditions could be achieved, but in the lower part of the reservoir a continuous meandering of the main stream around its longitudinal axis emerges.

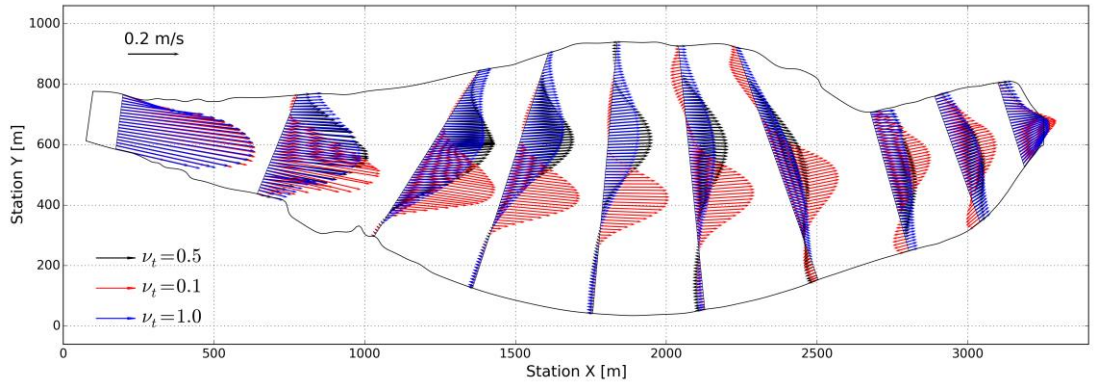

Figure 6.12: Telemac-2D: variation of the constant eddy viscosity ν_t

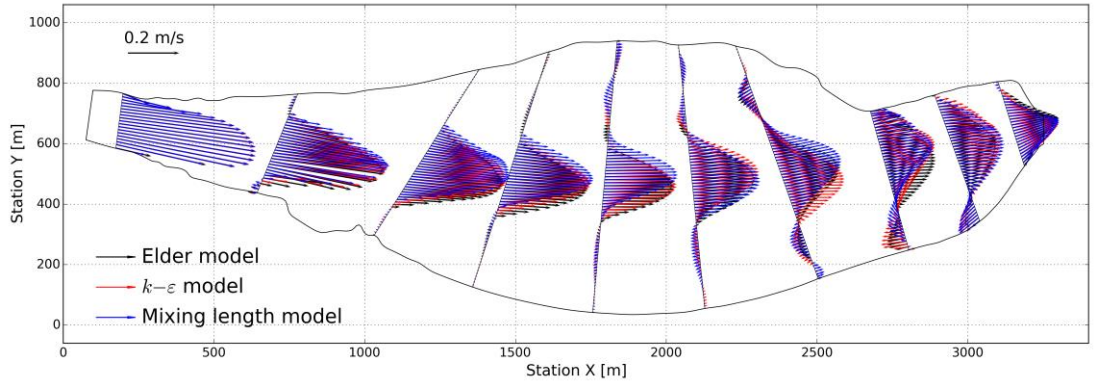

Figure 6.13: Telemac-2D: Elder model, k-ε model and Mixing Length model

The depth-averaged Mixing length turbulence model has been investigated in more detail. The semi-empirical coefficients α_t appearing in the vertical turbulence term and the mixing length l_m appearing in the horizontal turbulence term have been varied in order to study their respective influence on the simulated flow field in the reservoir.

The coefficient α_t has been varied from the default value of $\kappa/6 \approx 0.067$ to a value of 1.0. As described in section 2.2.3, this range for α_t has been proposed and used by various authors in their 2D depth-averaged models (Steffler and Blackburn, 2002, Vionnet et al., 2004, Wu et al., 2004). Based on the literature review given in section 2.3.2 and following the findings of Stansby (2003), in a first attempt the mixing length l_m has been changed from the default semi-empirical coefficient of $0.11h$ to half the water depth h. Figure 6.14 shows the simulation results when fixing l_m equal to $0.5h$ and varying the coefficient α_t for the vertical turbulence generation. Both tested values of $\alpha_t = \kappa/6$ and $\alpha_t = 1.0$ yield nearly identical flow fields. The simulation by means of the higher value calculates some more

pronounced recirculation zones in the lower part of the reservoir. The comparison leads to the intermediate conclusion that the vertical turbulence generation is not the dominant factor controlling the large-scale flow field in the reservoir. The minor role can be explained by the fact that in reservoirs typically, under normal operating conditions, highly non-uniform flow conditions with low energy gradient prevail. The low energy gradient in turn leads to very low values of shear velocity U^*, the term which constitutes to the vertical turbulence generation in the depth-averaged parabolic eddy viscosity model (section 2.3.2). The increase of the mixing length l_m from the default assumption of $0.11h$ to $0.5h$ has a distinct impact on the resulting flow field. The main stream is displaced from the center towards the orographic right river bank (Figure 6.13 and Figure 6.14). This comparison reveals the predominant influence of the horizontal turbulence production on the developing flow field in such a case. The use of the higher value for the mixing length generates higher turbulent diffusion, which in turn has a stabilizing effect on the numerical simulation. Compared to the simulations by means of the default values, the adopted mixing length of $l_m = 0.5h$ has yielded a nearly steady state condition of the flow field with only slight meandering of the main stream. This result is in line with the findings of Stansby (2003). In the validation of a 3D numerical model for the simulation of shallow wakes of a conical island he determined the mixing length l_m to have approximately a value of $0.5h$ for the transition from unstable to stable wakes. In a later publication Stansby (2006) simulated the same case by means of his 2D depth-averaged model. He used the same value for the mixing length estimation and found a worse prediction of stable wakes, compared to the 3D numerical results.

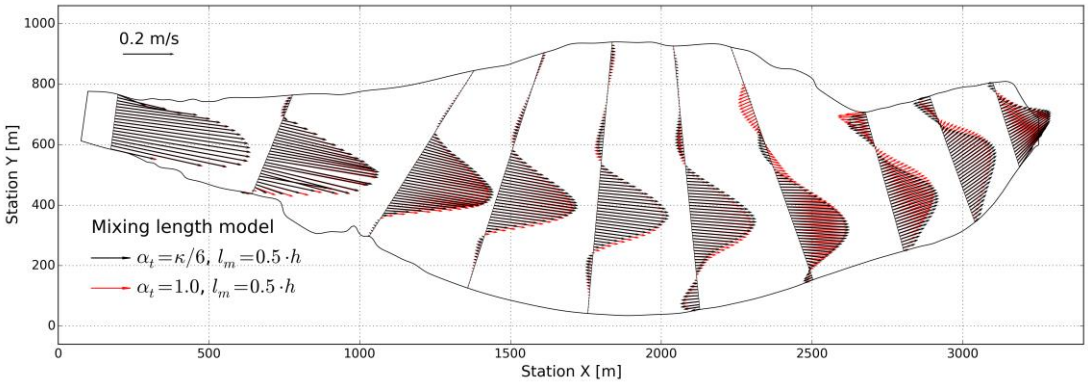

Figure 6.14: Telemac-2D: variation of the coefficient α_t in the Mixing Length model ($l_m = 0.5h$)

In the depth-averaged Mixing Length model higher values for the mixing length have been investigated with the aim to reach steady state flow conditions of the simulated flow field in the reservoir, namely $l_m = 1.0h$ and $l_m = 2.0h$. Figure 6.15 shows the comparison between the results when applying the three different mixing length relations. The simulations by means of the two higher values reach perfect steady state flow conditions. The values of $l_m = 0.5h$ and $l_m = 1.0h$ yield very similar results. The flow field is some more dampened by using the latter value. In the wider area of the reservoir both the relations compute four transitions between upstream and downstream flow directions. The result obtained by the use of $l_m = 2.0h$ demonstrates a considerable damping of the main stream development and recirculation zones which is due to the computed higher turbulent diffusion.

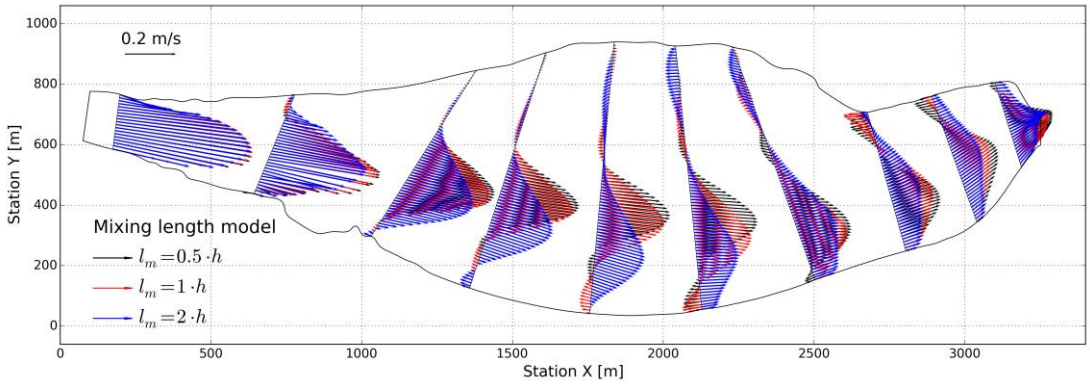

Figure 6.15: Telemac-2D: variation of the mixing length l_m in the Mixing Length model ($\alpha_t = \kappa/6$)

The results emphasize some interesting features of the Mixing Length turbulence model. In the presented case the coefficient α_t appearing in the vertical turbulence term doesn't' play a major role. The parameter study evidences that the horizontal turbulence production has the predominant influence on the simulated flow field in the reservoir. In the presented case study the assumption of the mixing length in the range between $l_m = 0.5h$ and $l_m = 1.0h$ seems physically plausible and is in line with the findings from Stansby (2003 and 2006).

Mesh resolution

In this variation the mesh sensitivity of Telemac-2D and the Mixing Length turbulence model has been studied by refining the mesh. The refining procedure consisted simply in splitting up every mesh triangle into four triangles. As hydraulic boundary conditions the design discharge of 440 m³/s and the normal operating water level of 461.5 m a.s.l. have been used. The simulation was run to a steady state flow condition. The bottom Strickler roughness k_{st} was set to a value of 50 $m^{1/3}/s$. In the Mixing Length turbulence model the coefficients α_t and l_m have been set to 0.5 and $1.0h$, respectively.

The simulation results obtained by means of the default mesh (39021 elements) and the refined mesh (156084 elements) are shown in Figure 6.16. The comparison demonstrates an excellent agreement between the two meshes which, in the first place, indicates the invariant scaling behaviour of the Mixing Length turbulence model. Furthermore, the study confirms that in the 2D simulations with the default mesh, the adopted edge length of 10 m is fine enough for capturing the main flow features in the reservoir.

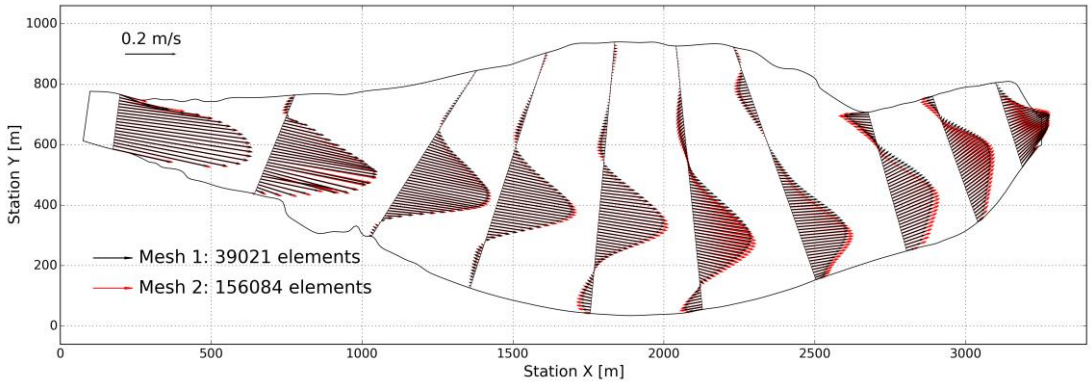

Figure 6.16: Telemac-2D: mesh sensitivity test of the Mixing Length turbulence model

Inflow zone

The previous parameter studies have shown that the simulated developing flow field in the reservoir is quite sensible to minor variations of numerical or physical parameters, like the choice of the Strickler roughness value. In numerical simulations and also in physical model studies of open channel flow special care has to be given on the locations of the hydraulic boundaries and their geometrical conditions, e.g. in terms of the dedicated zone for flow development or the inflow direction.

In this variation the default geometrical mesh design of the inflow zone has been modified by repositioning the inflow boundary. The cross section 700 has been copied about 300 m in upstream direction, parallel to its old location. The bottom elevations at the mesh nodes have been interpolated linearly between cross section 700 and the new inflow boundary. In this modified version not only the inflow length and the bottom elevations are different, but the inflow angle is slightly altered, too, compared to the default inflow geometry. Figure 6.17 shows the default inflow zone used in all presented studies (VAR 0) and the modified one (VAR 1).

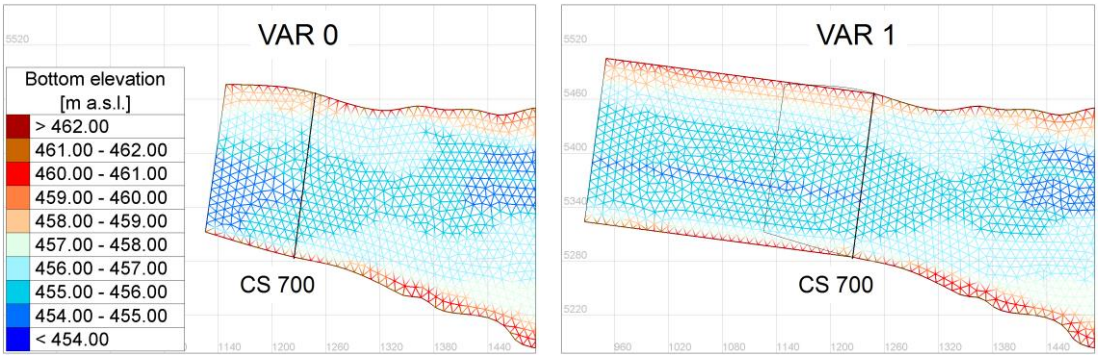

Figure 6.17: Telemac-2D: variation of the inflow zone, detail views of VAR 0 (default) and VAR 1

In the simulations the same hydraulic boundary conditions (Q = 440 m³/s, WL = 461.5 m a.s.l.), bottom roughness (k_{st} = 50 m$^{1/3}$/s) and turbulence model (Mixing Length model with α_t = 0.5 and $l_m = 1.0h$), as in the preceding study, have been adopted. The comparison of the resulting simulated flow fields, by using the two approaches for the inflow zones, is shown in Figure 6.18. The differences in the results are apparent. The simulation with the modified inflow zone (VAR 1) yields a completely different resulting flow field in the reservoir.

It is challenging to argue the pros and cons of the two approaches. The modified variant (VAR 1) is often used in physical model studies in order to create a smooth inflow zone where the flow can develop or to increase the distance from the inflow boundary to the zone of interest. In that sense the arguments for this approach are rational, especially if important measurement data aren't available. In the presented case study the default inflow geometry (VAR 0) has been set up by means of ADCP field measurements (inflow direction) and measured bottom elevations in the 100 m section upstream of cross section 700. Thus, the hydraulic and geometrical conditions measured in the inflow zone of the reservoir could be incorporated as valuable input data in the numerical model.

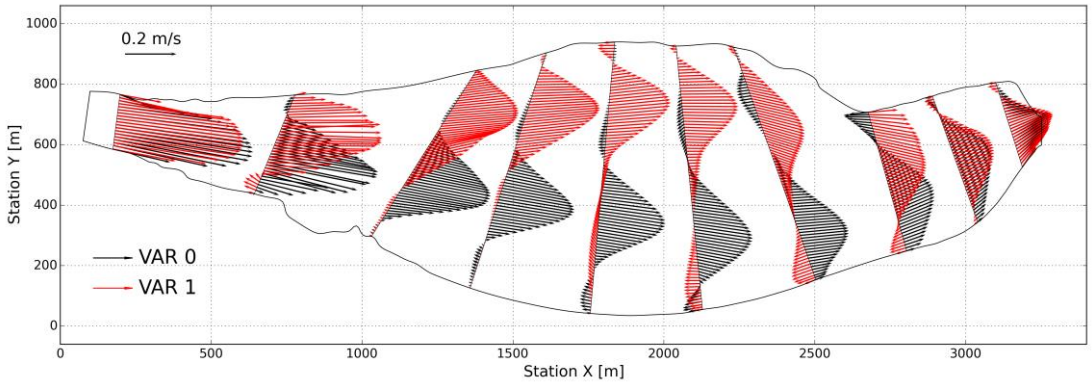

Figure 6.18: Telemac-2D: variation of the inflow zone

Discharge and water level variation

This study investigates the same two other hydraulic boundary condition settings as the Telemac-3D parameter study, described in section 6.3.2. In the 2D simulations the Strickler bottom roughness value was set k_{st} = 50 m$^{1/3}$/s and the Mixing Length turbulence with the coefficients α_t = 0.5 and l_m = 1.0h was applied.

The simulated flow fields shown in Figure 6.19 demonstrate almost the same behaviour as the results obtained by means of Telemac-3D (compare with Figure 6.5). Compared to the default hydraulic boundary conditions (normal turbine operation), in the two variants the main stream gets shifted towards the center in the wider area of the reservoir. Again, the reason can be attributed to the lowering of the water level at the outlet which causes the forming of shallow or even dry areas at the orographic right bank in the zone close downstream to the inlet. The altered flow condition in this area triggers the effective flow section to shift away from the orographic right bank which has the apparent effect of changing the main flow direction in the wider area of the reservoir.

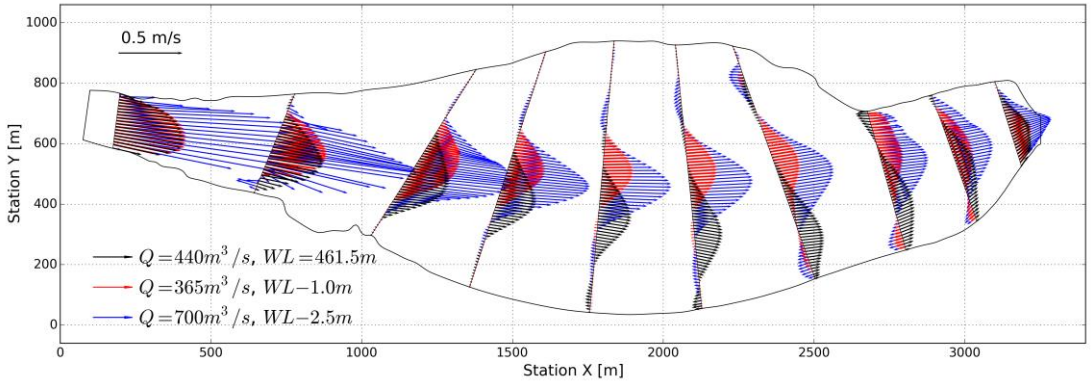

Figure 6.19: Telemac-2D, variation of discharge and water level

6.4.3 Installation of the groyne

Similar to the investigations carried out by means of Telemac-3D in section 6.3.3, this study analyses the impact of the installed non-submerged groyne on the resulting simulated flow field in the reservoir. In the simulations again the bottom roughness was set to

k_{st} = 50 m$^{1/3}$/s and the coefficients $\alpha_t = 0.5$ and $l_m = 1.0h$ in the Mixing Length turbulence model were applied.

The results presented in Figure 6.20 show that the non-submerged groyne has the impact to shift the flow field entirely from the orographic right bank to the left bank when adopting the design discharge and normal operating water level. In the flood scenario, by using a higher discharge of 700 m^3/s and a lowered water level by 2.5 m, the impact of the groyne on the simulated flow field is marginal. The main stream is shifted only slightly from the center towards the left bank compared to the simulation result without installation of the groyne (compare with Figure 6.19).

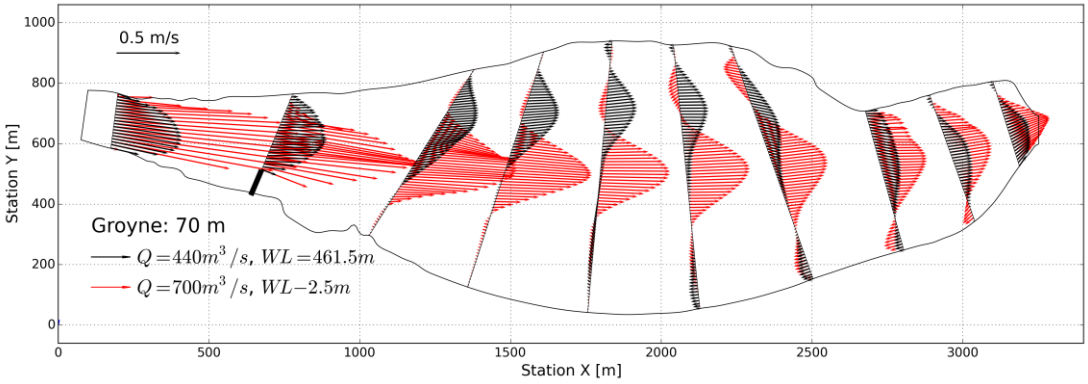

Figure 6.20: Telemac-2D, installation of 70 long groyne, variation of hydraulic boundary conditions

In a numerical experiment it has been aimed at realizing the same flow field behaviour in the flood scenario and the case of normal turbine operation by extending the non-submerged groyne from a length of 70 m to 100 m. The results are presented in Figure 6.21 for the case of the flood scenario and the two variants of groyne lengths. The comparison shows the relocation of the main stream towards the orographic left bank if a longer groyne of 100 m length is installed. The complete overlap of the simulated flow fields in the flood scenario and the case of normal turbine operation could not be realized (compare Figure 6.20 with Figure 6.21). However, the investigation shows that the installation of the longer groyne has the impact of aligning the flow fields at least to some extent by shifting the main stream towards the orographic left bank in the reservoir under different hydraulic boundary conditions.

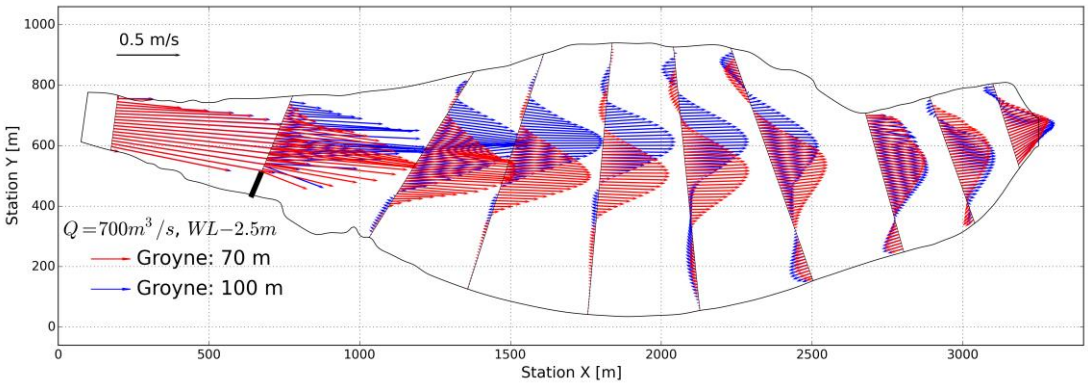

Figure 6.21: Telemac-2D, variation of the length of the groyne

6.5 Comparison of unsteady Telemac-2D simulations with ADCP field campaigns

In this final section the unsteady flow processes in the reservoir under the influence of time-varying discharge and water level, which are present typically within the operational schedule of the hydro power plant, have been investigated.
The 2D unsteady simulations aimed at investigating and replicating numerically the flow fields which were measured on the days of two ADCP measurement campaigns, namely ADCP campaign 2 (before implementation of the groyne) and ADCP campaign 5 (after implementation of the groyne in the prototype).

In the two unsteady simulations the 24 hours discharge and water level hydrographs were adopted which have been measured at the hydro power plant on the day of the respective ADCP measurement campaign. In the numerical model, for simplicity's sake, the 24 hours discharge hydrograph measured at the hydro power plant was assumed to act as inflow boundary condition at cross section 700. Of course, this assumption leads to time-shifted simulated flow fields compared to the developing flow processes occurring in the field. However, this fact was disregarded for the investigated purpose. Furthermore, the unsteady simulation of the 24 hours hydrograph may not capture all history effects of the developing flow field, bearing in mind that in the steady calculations presented in the previous section, simulation times of three to four days were required in order to reach steady flow conditions.

In the unsteady simulations the initial condition has been set to an in advance generated steady state flow field in order to prevent artificial unsteady flow effects in the results. The Strickler bottom roughness was set to a value of k_{st} = 50 $m^{1/3}/s$ and the depth-averaged Mixing Length turbulence model was used for turbulence closure. In the Mixing Length model the coefficient α_t has been set to 0.5. The assumption of the mixing length l_m in the range between $0.5h$ and $1.0h$ has yielded just steady state flow conditions under steady hydraulic boundary conditions, as described in section 6.4.2. Preliminary unsteady simulations by means of the two assumptions for the mixing length resulted in similar calculated time-dependent meandering of the flow field in the reservoir, with somewhat more damping of the developing flow field when using the higher value. For the presented investigations the mixing length l_m has been set to $0.5h$.

In the subsequent evaluations and comparisons of the simulated flow fields and the ADCP measurements the uncertainties have to be considered which emerge due to the interchanged discharge boundary conditions and the associated time lag, the possible missing of history effects as well as the inherent measurement uncertainties in the ADCP measurements.

6.5.1 Unsteady simulation of ADCP campaign 2

The unsteady simulation aimed at replicating the developing flow field in the reservoir which was measured on the day of the second ADCP measurement campaign. The ADCP campaign, presented in section 5.3, was carried out before implementation of the groyne in the prototype. The measured 24 hours discharge and water level hydrographs at the hydro

power plant have been used as inflow and outflow boundary condition, respectively. They are shown in Figure 6.22. As it can be observed, within the period of the ADCP measurements the discharge and the operating water level were nearly constant.

The measured depth-averaged velocity distributions in the ADCP campaign 2 are shown in Figure 6.23. The figure has been adopted from section 5.2. The simulated time-dependent depth-averaged flow fields are shown in Figure 6.24. In order to capture the unsteadiness, the time interval for the output of results has been set to half an hour.

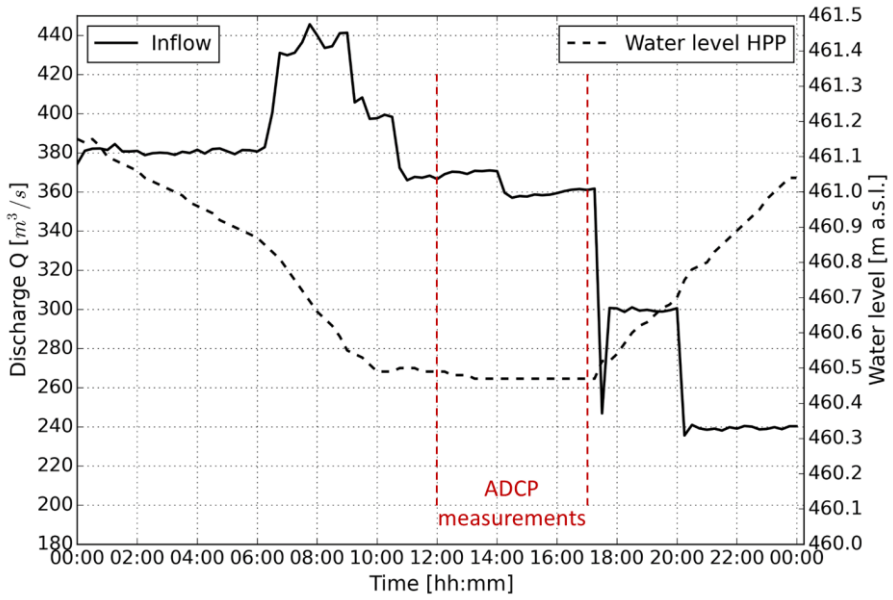

Figure 6.22: Telemac-2D: unsteady hydraulic boundary conditions from ADCP campaign 2

The simulated flow fields reveal the meandering flow field which develops in the reservoir under typical operating conditions of the hydro power plant. The results show that the unsteady boundary conditions have a remarkable impact on the time-dependent location as well as the crosswise contraction and expansion behaviour of the main stream. The comparison with the ADCP measurements shows that the simulated mutable flow field, in its entirety, fits well to the measured ADCP velocity distributions. The numerical model is able to reproduce the ADCP velocities very well especially in the area downstream of cross section 400. In the upstream part of the reservoir the numerical model shows a more steady state flow condition, as the comparison with the ADCP velocities at cross section 500 demonstrates. This difference can be attributed to the simulated flow conditions in the inflow area. In the numerical model the upper boundary condition by default doesn't allow any time-dependent variation of the inflow direction. However, in reality, some slight alterations of the inflow direction might emerge due to unsteady boundary conditions which in turn could cause the development of more flow variability downstream of the inflow zone.

In summary, this first unsteady simulation demonstrates the capability of the numerical model and the Mixing Length turbulence model – with its adapted coefficients α_t and l_m – of replicating the ADCP velocity measurements. The numerical model is able to simulate the

unsteady flow phenomena, in terms of time-dependent expansion and contraction flows, which develop in the reservoir.

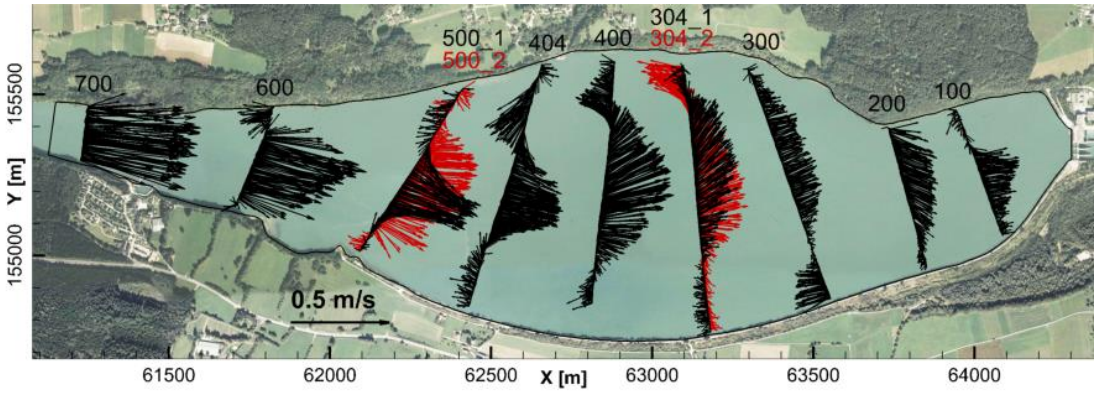

Figure 6.23: ADCP measurements from the 2nd campaign, before installation of the groyne

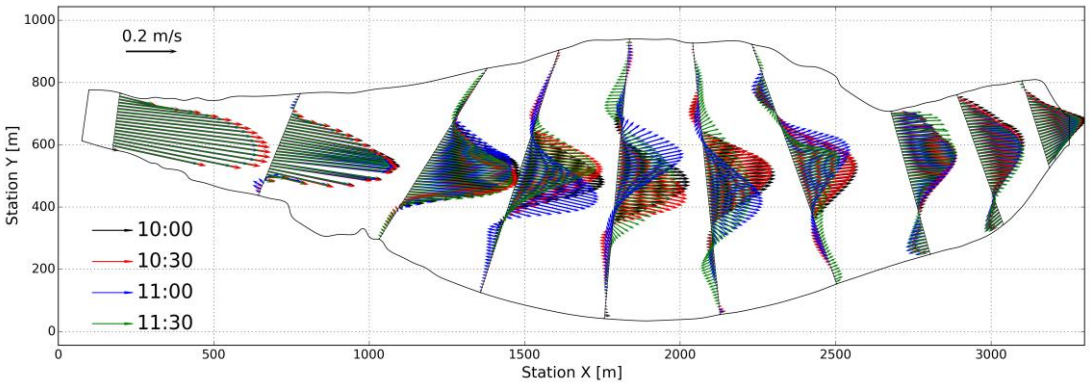

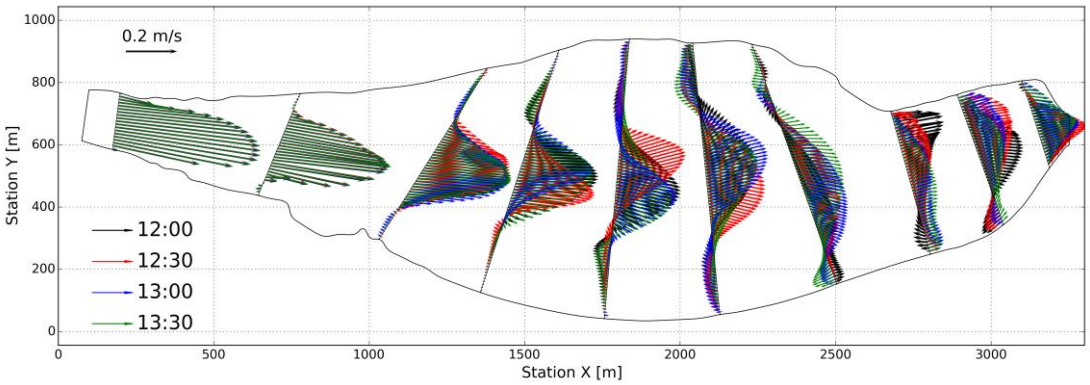

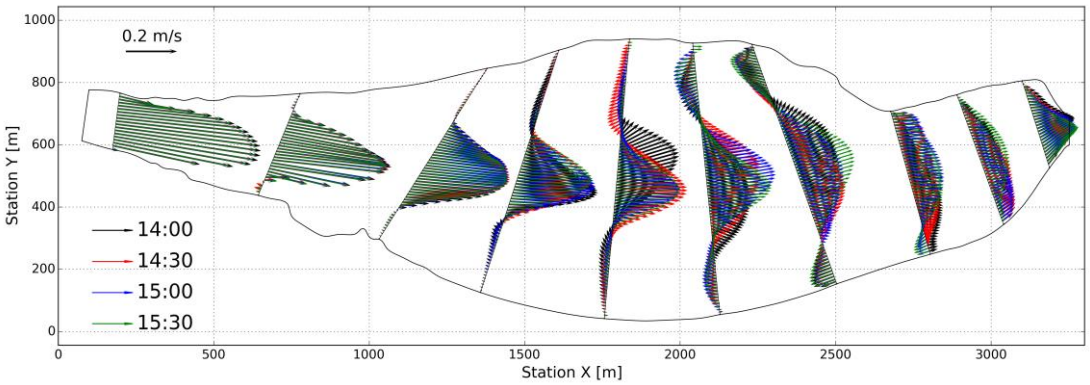

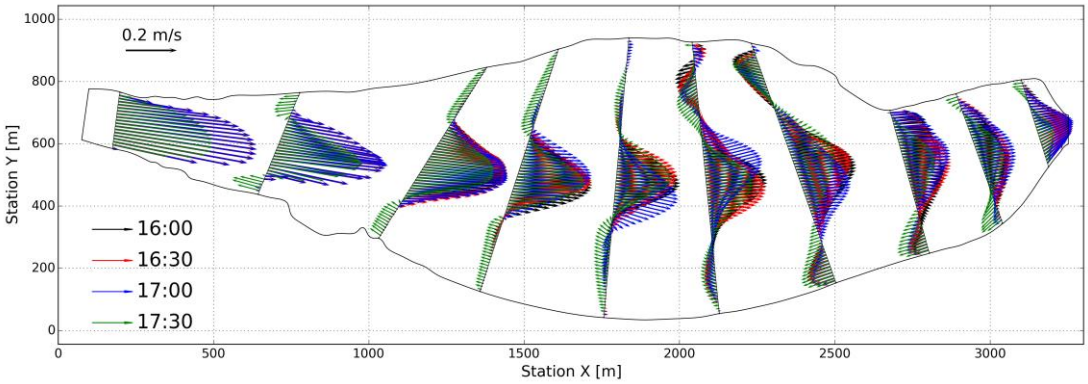

Figure 6.24: Telemac-2D: simulated time-dependent flow fields, simulation without groyne

6.5.2 Unsteady simulation of ADCP campaign 5

The unsteady simulation aimed at replicating the developing flow field in the reservoir which was measured on the day of the fifth ADCP measurement campaign, after implementation of the groyne in the prototype. The ADCP campaign is presented in section 5.6. The measured 24 hours unsteady hydraulic boundary conditions adopted in the numerical model for the time-varying inflow and water level at the outlet are shown in Figure 6.25. The ADCP measurement time was about three hours. Within this period the discharge and the operating water level had nearly constant values.

The measured depth-averaged velocity distributions in the ADCP campaign 5 are shown in Figure 6.26. The figure has been adopted from section 5.4. The simulated time-dependent depth-averaged flow fields are shown in Figure 6.27.

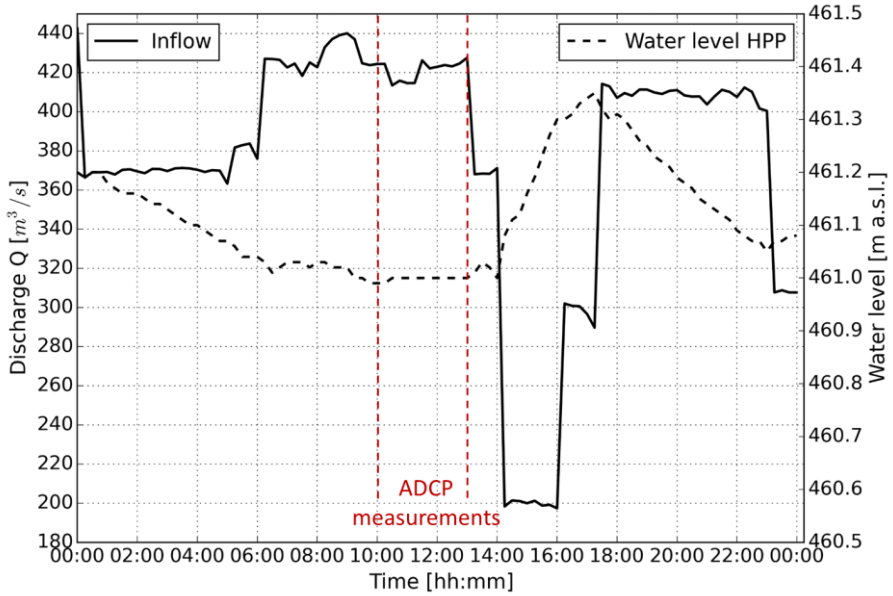

Figure 6.25: Telemac-2D: unsteady hydraulic boundary conditions from ADCP campaign 5

The simulation with the implemented groyne again indicates the important impact of the unsteady boundary conditions on the developing time-dependent flow fields in the reservoir.

The computed variable flow fields as a whole agree very well with the measured ADCP velocity distributions, considering the uncertainties described in the introductory part of this section. The measured flow dynamics, e.g. at cross section 400, can be captured by the numerical model. At cross section 500 the ADCP measurements show a complex time-dependent flow behaviour, which, despite of a time lag, the numerical model is able to replicate. The steady flow simulations have shown already that the groyne has a definitive impact on the developing flow field in the wider area of the reservoir. In these simulations the groyne causes the main stream to be shifted to the center or even to the orographic left bank, depending on the used steady hydraulic boundary conditions. However, the unsteady simulations, supported by the ADCP measurements, demonstrate that the groyne doesn't have the expected stabilizing impact on the developing flow field in the reservoir under operating unsteady flow conditions.

The simulated case with implemented groyne can be considered as validation case for the previous presented unsteady simulation without the installed groyne. The 2D numerical model with the depth-averaged Mixing Length turbulence model is able to replicate the ADCP measurements and evidences the complex unsteady flow phenomena in the reservoir which develop under unsteady hydraulic flow conditions.

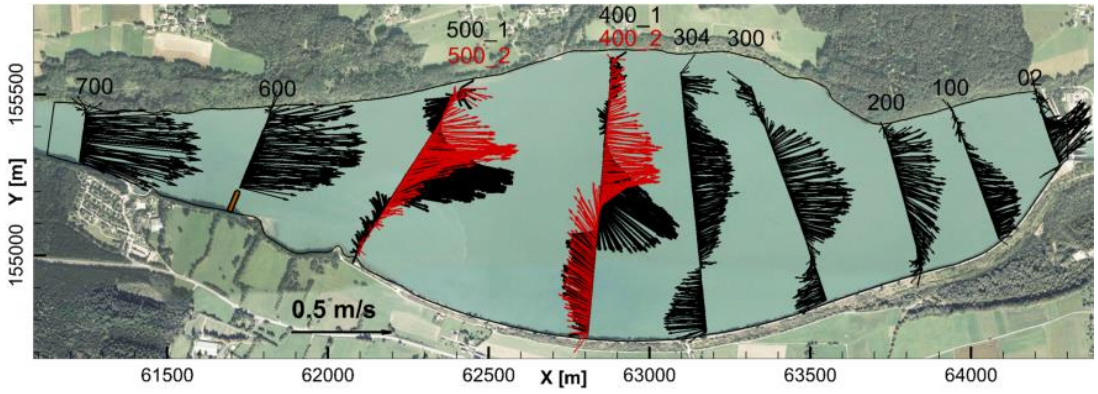

Figure 6.26: ADCP measurements from the 5th campaign, after installation of the groyne

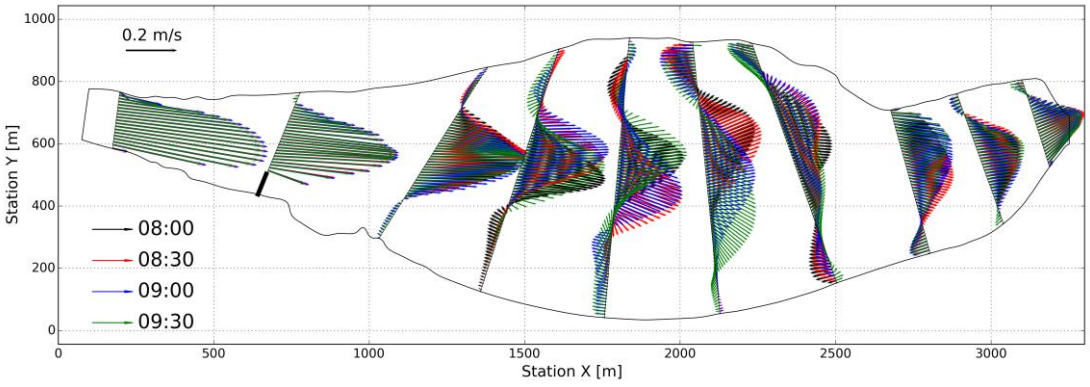

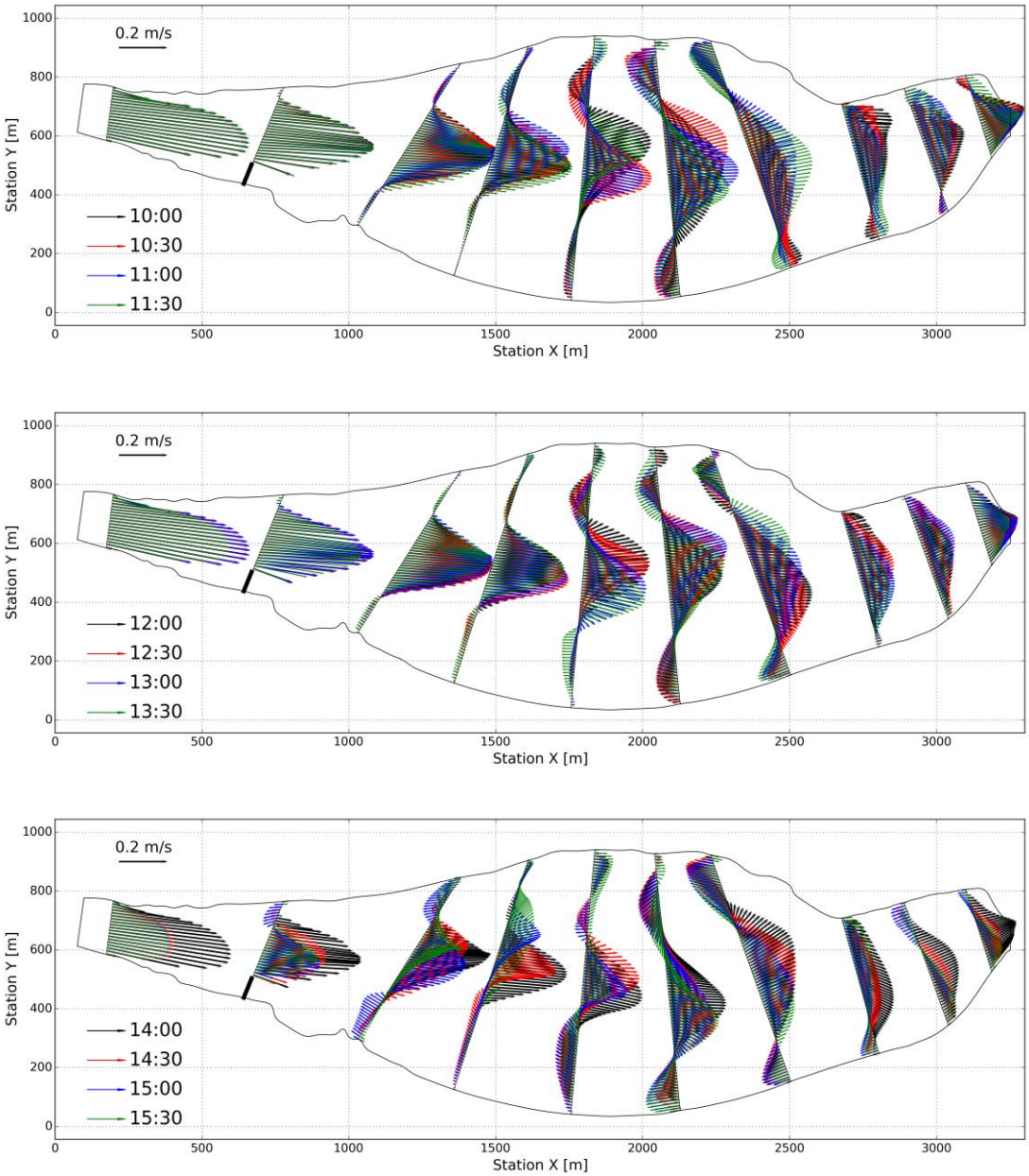

Figure 6.27: Telemac-2D: simulated time-dependent flow fields, simulation with groyne

6.6 Summary

The 3D and 2D steady numerical simulations with Telemac-3D and Telemac-2D, respectively, aimed at analysing the impact of different physical and numerical parameters on the resulting simulated flow fields in the reservoir. The investigations focused especially on the computed expansion flow phenomena in terms of main stream development.

In both numerical models the choice of the roughness value or the turbulence model has a significant impact on the computed developing flow field in terms of location of the main stream. In the steady 3D and 2D calculations the application of different discharges and water levels yields remarkable different development of depth-averaged flow fields in the

reservoir. The geometrical variation of the inflow zone, by changing the position of the inflow boundary and slightly the inflow direction, reveals the high sensitivity of the 2D simulated flow field to the setup of the inflow boundary when dealing with expansion flow in reservoirs. The installation of the non-submerged groyne in the 3D model as well as in the 2D model yields a definite alteration of the computed flow field compared to the calculations without groyne, however, not for all investigated hydraulic load cases.

The analysis of the secondary flow intensities in the simulations with hydrostatic pressure and non-hydrostatic pressure assumption reveals a weak three-dimensionality of the flow behaviour computed by Telemac-3D. This result suggests that the flow phenomena developing in the reservoir, at least the numerically simulated large-scale flow behaviour, can be resolved by means of the 2D shallow water equations. The variation of the advection scheme of velocities and turbulent quantities for the case with installed groyne revealed a remarkable difference in the 3D simulated flow field, compared to the results obtained by means of the default applied advection scheme. This fact leads to the conclusion that the numerically simulated flow field is not only sensitive to the chosen physical parameters, but apparently, also to the used numerical discretization scheme. This finding may be generally valid for 2D or 3D numerical modelling of expansion flow in reservoirs.

The parameters studies carried out in the 3D and 2D numerical simulations demonstrate that the computed large-scale flow field for a specific hydraulic load case could be fitted to the experimental results or the ADCP field measurements simply by a proper combination of selected bottom roughness coefficient and turbulence model. However, as the investigations show, the predictive capability of a fitted (calibrated) numerical model of replicating expansion flow phenomena in the reservoir under different hydraulic flow conditions or for a modified reservoir geometry has to be questioned.

In the numerical investigations a special focus was given on the depth-averaged Mixing length turbulence model implemented in Telemac-2D. The variation of its semi-empirical coefficients demonstrates that in reservoir-like flow conditions the vertical turbulence generation plays a minor role only, whereas the horizontal turbulence generation has the dominant influence on the simulated developing flow field in the reservoir. The semi-empirical coefficients in the turbulence were calibrated in order to yield just steady state flow conditions under steady hydraulic boundary conditions. Unsteady simulations of two ADCP velocity measurement campaigns, using the same calibrated values for the semi-empirical coefficients, were able to replicate the horizontally meandering flows measured in the ADCP campaigns. The simulation results evidence the development of complex unsteady flow phenomena in the reservoir which can develop even under slightly unsteady hydraulic operation of the hydro power plant.

7 Conclusion and Outlook

In this thesis, the developing flow phenomena in a shallow reservoir of a run-of-river hydro power plant were investigated. The reservoir is characterized by a gradual horizontal expansion zone which leads to the development of complex flow fields. A physical model study of the reservoir and the subsequent implementation of the experimental results in the prototype served as basis for the investigations. The research aimed at assessing the developing complex flow fields in prototype-scale by means of ADCP velocity measurements and at identifying the sensitivities in the 3D and 2D depth-averaged numerical modelling on real bathymetry and flow conditions.

Within the thesis work, an open source software was developed for processing and analyzing ADCP measurement data. In the open source 2D shallow water solver Telemac-2D the depth-averaged Mixing Length turbulence model was implemented. In the 2D numerical investigations a special emphasis was given on this turbulence model.

Physical model experiments

The physical model study dealt with the optimization of the sediment management in the reservoir. Purpose of the experiments was the analysis of the developing flow fields in the reservoir under different hydraulic flow conditions. The flow fields in the physical model were investigated by means of moving-boat Acoustic Doppler Current Profiler (ADCP) velocity measurements.

The experiments demonstrated that different flow patterns develop depending on the applied steady hydraulic boundary conditions. The location of the main downstream flow and the related backflow changes from the right bank to the left bank or vice versa, with the potential development of intermediate states. Hence, the measurements revealed a first explanation for the disordered sedimentation behaviour in the reservoir. Based on these results, the experiments aimed at developing the design of one or more training structures and identifying their optimal positioning, with the objectives to reduce the reservoir sedimentation and to increase the flushing efficiency in the study area. A solution was found by installation of a non-submerged groyne at the beginning of the expansion zone. The training structure had the effect to align the developing flow fields, in terms of location of the main stream, for different steady hydraulic flow conditions. Accordingly, the groyne was implemented in the prototype.

ADCP measurements in the prototype

In the prototype five ADCP moving-boat velocity measurements were carried out at predefined cross sections. Two of them were carried out before and three campaigns after installation of the groyne in the prototype. Primary aim of the ADCP measurements was the investigation of the developing flow fields in the reservoir before and after implementation of the groyne. For a comprehensive analysis of the flow behaviour in the expanded area the

campaigns differed in the hydraulic boundary conditions in terms of discharge and operating water level.

In the ADCP campaigns the developing large-scale flow fields could be determined. The ADCP measurements are able to capture very sharp horizontal shear layers with abrupt transitions between downstream and upstream flow. The measured crosswise recirculations and flow redistributions indicate the presence of strong secondary currents. The field measurements replicate the physical model experiments and evidence the impact of the non-submerged groyne on the developing flow field. In the physical model and in the prototype the horizontal shear layers and the zones of transition between downstream and upstream flows impressively are measured at the almost same locations. Though, the field measurements could confirm the physical model results for the cases without and with installation of the groyne, only, if steady flow conditions are present in the prototype. Repetitive measurements at cross sections and analysis of measured discharges indicate the development of unsteady meandering flow for the case of typical everyday operation of the hydro power plant. These results show also that the implemented groyne has not enough impact to align the flow fields for different flow conditions and to prevent the meandering of the main stream in the reservoir.

In addition to the large-scale flow field measurements, the estimation of bed shear stress, roughness height as well as turbulent kinetic energy in the reservoir by means of two stationary ADCP measurements was investigated. The roughness height was estimated by means of the logarithmic law of the wall. For the estimation of bed shear stress the law of the wall method and the turbulent kinetic energy method were investigated and compared. Both methods yield physically plausible estimates of bed shear stress and turbulent kinetic energy in the reservoir. The comparison with approaches in literature points out the feasibility of these methods to estimate these quantities in reservoir-like flow conditions.

Numerical modelling

The 3D and 2D steady numerical simulations with Telemac-3D and Telemac-2D, respectively, aimed at analysing the impact of different physical and numerical parameters on the resulting simulated flow fields in the reservoir. The investigations focused especially on the computed expansion flow phenomena in terms of main stream development.

In both numerical models the choice of the roughness value or the turbulence model has a significant impact on the computed developing flow field. In the steady 3D and 2D calculations the application of different discharges and water levels yields remarkable different depth-averaged flow patterns in the reservoir. The geometrical variation of the inflow zone, by changing the position of the inflow boundary and slightly the inflow direction, reveals the high sensitivity of the 2D simulated flow field to the setup of the inflow boundary when dealing with expansion flow in reservoirs. The installation of the non-submerged groyne in the 3D model as well as in the 2D model yields a distinct alteration of the computed flow field compared to the calculations without groyne, however, not for all investigated hydraulic load cases.
The analysis of the secondary flow intensities in the simulations with hydrostatic pressure and non-hydrostatic pressure assumption reveals a weak three-dimensionality of the flow

behaviour. This result suggests that the flow phenomena developing in the reservoir, at least the numerically simulated large-scale flow behaviour, can be resolved by means of 2D shallow water equations. The variation of the advection scheme of velocities and turbulent quantities for the case with installed groyne revealed a remarkable difference in the 3D simulated flow field, compared to the results obtained by means of the default applied advection scheme. This fact leads to the conclusion that the numerically simulated flow field is not only sensitive to the chosen physical parameters, but apparently, also to the used numerical discretization scheme. This finding may be generally valid for 2D or 3D numerical modelling of expansion flow in reservoirs.

In the numerical investigations a special focus was given on the depth-averaged Mixing length turbulence model implemented in Telemac-2D. The variation of its semi-empirical coefficients indicates that in reservoir-like expansion flow conditions vertical turbulence generation plays a minor role only, whereas horizontal turbulence generation has the dominant influence on the simulated developing flow field. The semi-empirical coefficients in the turbulence model were calibrated in order to yield just steady state flow conditions under steady hydraulic boundary conditions. Unsteady simulations of two ADCP velocity measurement campaigns, using the same calibrated values for the semi-empirical coefficients, could replicate the measured horizontally meandering flows.

7.1 Findings and contributions of the thesis

The findings in the thesis contribute to the understanding of developing expansion flow phenomena in shallow reservoirs which are characterized by a horizontal expansion zone. Existing research works focused mainly on the experimental investigations of abrupt expansion flow in shallow, idealized rectangular symmetrical basins. Therefore, the findings of the thesis, specifically the investigations of expansion flow phenomena in prototype-scale, constitute further important components to this research field.

The field measurements demonstrate the capability of the ADCP technique of investigating and determining complex expansion flow phenomena in shallow reservoirs. The ADCP velocity measurements are able to identify sharp shear layers, flow redistributions and secondary currents which may emerge in expansion flows. The investigation of unsteady meandering flow by means of ADCP moving-boat velocity measurements remains a challenge. With this method it is not possible to capture the complete large-scale flow field in a reservoir at a specific time, however, it allows the detection and the qualitative assessment of developing meandering flow.
The measurements in prototype scale yield an important finding in which they prove that not only the shape of the reservoir but also the hydraulic boundary conditions as well as small-scale characteristics of the reservoir, like locally existing bed elevations, have a significant influence on the developing expansion flow in a shallow reservoir. Hence, the investigation of developing expansion flow by means of a simplified physical model setup of a shallow reservoir, e.g. for prediction of preferential sedimentation zones, has to be questioned.
A second central research finding is that even slight unsteady hydraulic flow conditions, e.g. due to hydro power plant operation, may induce complex unsteady flows with large-scale

meandering of the main stream in a shallow reservoir. In addition, stationary measurements prove the capability of the ADCP technique of estimating bed shear stress, roughness height as well as turbulent kinetic energy in reservoir-like flow conditions. These quantities can be used as valuable input data for 3D and 2D depth-averaged numerical models.

The complexity of assessing expansion flow phenomena in a shallow reservoir with real bathymetry is reflected also in the 3D and 2D depth-averaged numerical modelling with Telemac-3D and Telemac-2D, respectively. The 3D and 2D depth-averaged numerical investigations demonstrate that the simulation of expansion flow on real bathymetry is associated with many uncertainties in the choices of numerical parameters and setups. The large-scale flow field to be computed for a specific hydraulic load case could be fitted to experimental results or ADCP field measurements simply by a proper combination of e.g. selected bottom roughness coefficient and turbulence model. However, the predictive capability of a fitted (calibrated) numerical model of replicating expansion flow phenomena for other hydraulic flow conditions or a modified reservoir geometry has to be critically examined. Although ADCP measurements reveal the localised presence of secondary currents, the 3D simulations indicate a weak three-dimensionality of the large-scale flow behaviour. This leads to the finding that the numerically simulated large-scale flow field in a shallow reservoir can be resolved by means of the 2D shallow water equations. 2D numerical simulations with the depth-averaged Mixing Length turbulence model confirm the suitability of using this turbulence model in simulating complex flow phenomena in shallow reservoirs. The use of this turbulence model yields a valuable outcome in which it evidences the dominant influence of horizontal turbulence generation on the computed expansion flow in a shallow reservoir, whereas vertical turbulence generation plays a minor role only. Unsteady 2D numerical simulations of ADCP measurements evidence the emerging of complex unsteady flow phenomena in shallow reservoirs which can develop even under slight unsteady hydraulic flow conditions.

The findings explained above are of high practical relevance. They highlight that velocity measurements in prototype-scale are crucial for improving the management of existing shallow reservoirs with complex shapes, e.g. for improving the prediction of preferential sedimentation zones or optimization of the flushing efficiency. The findings indicate that field measurements and numerical modelling are a very valuable combination for the assessment of developing flow phenomena for different hydraulic flow conditions in existing shallow reservoirs. It has to be recommended that field measurements are mandatory in order to verify the numerical model and its predictive capability of simulating flows in a reservoir with complex shape. As explained above, the numerical modelling of flows in reservoirs with complex shape is associated with high uncertainties. Therefore, for the design of a new shallow reservoir with complex geometry, physical model studies are recommended in order to assess future sedimentation and flow behaviour and hence, to develop an efficient and sustainable reservoir management.

The research work led to the development of an open source software for processing ADCP measurement data. The methods implemented in the software were efficiently used in the thesis for the analysis and visualization of ADCP data. The software contributes to the

understanding and analysis of ADCP velocity measurements and is intended for research purposes but also for the use in engineering practice.

The implementation of the depth-averaged Mixing Length turbulence model in the open source 2D depth-averaged shallow water solver Telemac-2D can be regarded as another scientific contribution. The model is based on the combination of the depth-averaged parabolic eddy viscosity model and the Prandtl's mixing length model for the horizontal. The turbulence model was validated and successfully applied for the simulation of developing complex expansion flow in reservoir-like flow conditions. Meanwhile, the implemented turbulence model is used by other research institutions and engineering companies for the simulation of a wide variety of free surface flows with Telemac-2D.

7.2 Outlook

The research presented in the thesis indicates the challenges in assessing developing complex expansion flow phenomena in a shallow reservoir which is characterized by a gradual horizontal expansion zone at the entrance. Based on the results, recommendations for further research work can be outlined.

In the physical model of the case study the developing flow fields under steady hydraulic flow conditions were analysed. Of course, it would be interesting to investigate experimentally, within a controlled physical model setup, the developing expansion flow phenomena under unsteady hydraulic boundary conditions, which are present during the everyday normal operation of a hydro power plant. Such investigations have a high practical relevance since they may lead to a better management of a newly created reservoir. Flow velocity measurements in a reservoir in prototype-scale for determining potentially developing meandering flows are a difficult and cost-intensive task. The developing meandering flows could be measured by large-scale particle image velocimetry (LSPIV) which measures velocities at the free surface or by the installation of several simultaneously measuring ADCPs devices which, for a given period, are anchored at predefined locations. By using ADCPs, the local flow velocities as well as the vertical velocity gradients can be measured. The measurements of vertical velocity gradients at different locations of a reservoir would allow the estimation of spatially distributed bed shear stresses, roughness heights and turbulence. The development of methods for estimating these quantities in reservoir-like flow conditions should have a high relevance in further research. In order to enhance the predictive capability of numerical models of simulating developing steady or unsteady flow fields and further, the associated sediment transport, in complex reservoir geometries, future research should focus specifically on field measurements of not only large-scale flow velocity distributions but also of other important basic physical quantities, like spatially distributed roughness heights and turbulence.

Bibliography

Biron P., Robson C., Lapointe M. and Gaskin S., 2004. Comparing different methods of bed shear stress estimates in simple and complex flow fields: Earth Surface Processes and Landforms, 29, 1403-1415.

Camnasio E., Orsi E. and Schleiss A. J., 2011. Experimental study of velocity fields in rectangular shallow reservoirs. Journal of Hydraulic Research, 49(3), 352-358.

Camnasio E., Pirotton M., Erpicum S. and Dewals B., 2012. Experimental and numerical investigation of a meandering jet in shallow rectangular reservoirs under different hydraulic conditions. Proceedings of the 3rd Int. Symp. on Shallow Flows, College of Engineering, University of Iowa, Iowa, IA.

Carr M.L and Rehmann C.R., 2007. Measuring the Dispersion Coefficient with Acoustic Doppler Current Profilers. Journal of Hydraulic Engineering, ASCE, 133, 977-982.

Cea L., Puertas J. and Vázquez-Cendón M.E., 2007. Depth Averaged Modelling of Turbulent Shallow Water Flow with Wet-Dry Fronts. Archives of Computational Methods in Engineering, 14, 303-341.

CHC - Canadian Hydraulics Centre, National Research Council, 2011. Blue Kenue, Reference Manual.

Chini N. and Stansby P.K., 2014. Modelling the flow around an island and a headland: application of a two mixing length model with Telemac3D. 34th Coastal Engineering Proceedings

Chow V.T., 1973. Open-Channel Hydraulics. International Edition, McGraw-Hill Book Company, Singapore.

Deines K.L., 1999. Backscatter Estimation Using Broadband Acoustic Doppler Current Profilers. Reprint by permission of the IEEE conference, San Diego, California.

Dewals B.J., Kantoush S.A., Erpicum S., Pirotton M. and Schleiss A.J., 2008. Experimental and numerical analysis of flow instabilities in rectangular shallow flow basins. Environmental Fluid Mechanics, 8, 31-54.

Dinehart R.L. and Burau J.R., 2005. Repeated surveys by acoustic Doppler current profiler for flow and sediment dynamics in a tidal river. Journal of Hydrology, 314, 1-21.

Dorfmann C. and Knoblauch H., 2009. Calibration of 2-D and 3-D numerical models of a large reservoir using ADCP measurements. Water Engineering for a Sustainable Environment, Proceedings of the 33th IAHR Congress, Vancouver, Canada.

Dorfmann C., Harb G. and Zenz G., 2012. Simulation of hydrodynamic and sediment transport processes – Two Austrian case studies. Proceedings of the XIXth TELEMAC-MASCARET User Conference, HR Wallingford, Oxford, United Kingdom

Dorfmann C. and Zenz G., 2013a. Numerische Untersuchungen mit Telemac bei Wasserkraftanlagen – zwei Fallstudien. Wasserwirtschaft, Springer, 12, 41-46.

Dorfmann C., Steidl J. and Zenz G., 2013b. ADCPtool: an open source ADCP postprocessing framework. Proceedings of the 35th IAHR World Congress, Chengdu, China.

Dorfmann C., Knoblauch H. and Steidl J., 2014. ADCP und Schwebstoffmessungen im Stausee Wasserfallboden. Research report, Graz University of Technology.

Dorfmann C. and Zenz G., 2016. The depth-averaged Mixing Length turbulence model for Telemac-2D. Proceedings of the XXIIIth TELEMAC-MASCARET User Conference, Cerema, Paris, France

Dufresne M., Dewals B. J., Erpicum S., Archambeau P. and Pirotton M., 2010a. Classification of flow patterns in rectangular shallow reservoirs. Journal of Hydraulic Research, 48(2), 197-204.

Dufresne M., Dewals B. J., Erpicum S., Archambeau P. and Pirotton M., 2010b. Experimental investigation of flow pattern and sediment deposition in rectangular shallow reservoirs. International Journal of Sediment Research, 25(3), 258-270.

Dufresne M., Dewals B. J., Erpicum S., Archambeau P. and Pirotton M., 2011. Numerical investigation of flow patterns in rectangular shallow reservoirs. Eng. Appl. Comput. Fluid Mech., 5(2), 247-258.

EDF - R&D, 2014. TELEMAC modelling system - 2D hydrodynamics TELEMAC-2D software, Release 7.0, User Manual. www.opentelemac.org.

Elder J.W., 1959. The dispersion of marked fluid in turbulent shear flow. Journal of Fluid Mechanics, 5(4), 544-560.

Fischer H.B., List J.E., Koh R.C.Y., Imberger J., Brooks N.H., 1979. Mixing in Inland and Coastal Waters. Academic Press, San Diego.

González J.A., Melching C.S. and Oberg K A., 1996. Analysis of open channel velocity measurements collected with an acoustic Doppler current profiler. RiverTech conference, Proceedings from the 1st International Conference On New/Emerging Concepts for Rivers, International Water Resources Association, Chicago.

Harb G., Dorfmann C., Schneider J., Haun S. and Badura H., 2012. Numerical analysis of sediment transport processes in a reservoir. Proceedings of the 6th International Conference on Fluvial Hydraulics, River Flow 2012, San Jose, Costa Rica.

Henderson A., 2007. ParaView Guide, A Parallel Visualization Application, Kitware Inc.

Hervouet J.-M., 2007. Hydrodynamics of Free Surface Flows: modelling with the finite element method. Wiley.

Hunter J.D., 2007. Matplotlib: A 2D graphics environment. Computing in Science & Engineering, IEEE Computer Society.

Jia Y. and Wang S.S.Y., 1999. Numerical model for channel flow and morphological change studies. Journal of Hydraulic Engineering, ASCE, 125, 924-933.

Jia Y. and Wang S.S.Y., 2001. CCHE2D: Two-dimensional Hydrodynamic and Sediment Transport Model For Unsteady Open Channel Flows Over Loose Bed. Technical Report No. NCCHE-TR-2001-1, NCCHE, School of Engineering, The University of Mississippi

Jones E., Oliphant T., Peterson P. and others, 2001. SciPy: Open Source scientific tools for Python. http://www.scipy.org.

Jones W.P. and Launder B.E., 1972. The Prediction of Laminarization with a Two-Equation Model of Turbulence. International Journal of Heat and Mass Transfer, 15, 301-314.

Kantoush S., 2008. Experimental study on the influence of the geometry of shallow reservoirs on flow patterns and sedimentation by suspended sediments. PhD thesis. Ecole Polytechnique Fédérale de Lausanne, Switzerland.

Kármán von, T., 1930. Mechanische Ähnlichkeit und Turbulenz. Nachrichten von der Gesellschaft der Wissenschaften zu Göttingen, Fachgruppe 1 (Mathematik) 5, 58-76.

Kim D., Muste M., Weber L. and Asman R., 2007. AdcpXP, A tutorial for using AdcpXP. IIHR - Hydroscience & Engineering, University of Iowa.

Kim S., Friedrichs C., Maa J. and Wright L., 2000. Estimating bottom stress in tidal boundary layer from acoustic Doppler velocimeter data. Journal of Hydraulic Engineering, ASCE, 126, 399-406.

Kobus H., 1984. Wasserbauliches Versuchswesen. Schriftenreihe des deutschen Verbandes für Wasserwirtschaft und Kulturbau 39, 2nd Edition. Parey Verlag, Hamburg.

Lane S.N., Bradbrook K.F., Richards K.S., Biron P.M. and Roy A.G., 2000. Secondary circulation cells in river channel confluences: measurement artefacts or coherent flow structures? Hydrological Processes, 14, 2047-2071.

Latosinski F.G., Szupiany R.N., García C.M., Guerrero M. and Amsler M.L., 2014. Estimation of Concentration and Load of Suspended Bed Sediment in a Large River by Means of Acoustic Doppler Technology. Journal of Hydraulic Engineering, ASCE, 140(7)

Launder B.E. and Spalding D.B., 1974. The numerical computation of turbulent flows. Computer Methods in Applied Mechanics and Engineering, 3 (2), 269-289.

Malcherek A., 2002. Fließgewässer - Hydromechanik und Wasserbau. Institut für Wasserwesen, Universität der Bundeswehr München, Version 3.0.

Mueller D.S., Wagner C.R., Rehmel M.S., Oberg, K.A. and Rainville F., 2013. Measuring discharge with acoustic Doppler current profilers from a moving boat, U.S. Geological Survey, Techniques and Methods, book 3, chap. A22, http://dx.doi.org/10.3133/tm3A22.

Muste M., Yu K. and Spasojevic M., 2004. Practical aspects of ADCP data use for quantification of mean river flow characteristics; Part I: moving-vessel measurements. Flow Measurement and Instrumentation, 15, 1-16.

Nezu I. and Nakagawa H., 1993. Turbulence in Open-Channel Flows. IAHR Monograph, Balkema Publishers, Rotterdam, The Netherlands.

Nikuradse J., 1932. Gesetzmäßigkeiten der turbulenten Strömung in glatten Rohren. VDI Forsch.-Heft, 356.

Nystrom E.A., Chris R. Rehmann C.R. and Oberg K.A., 2007. Evaluation of Mean Velocity and Turbulence Measurements with ADCPs. Journal of Hydraulic Engineering, ASCE, 133, 1310-1318.

Oliphant T., 2006. Guide to NumPy. http://www.numpy.org.

Parsons D. R., Jackson P. R., Czuba J. A., Engel F. L., Rhoads B. L., Oberg K. A., Best J. L., Mueller D. S., Johnson K. K. and Riley J. D., 2013. Velocity Mapping Toolbox (VMT): a processing and visualization suite for moving-vessel ADCP measurements. Earth Surface Processes And Landforms. doi: 10.1002/esp.3367.

Peltier Y., Erpicum S., Archambeau P., Pirotton M. and Dewals B., 2013. Experimental and numerical investigation of meandering jets in shallow reservoir: Potential impacts on deposit patterns. THESIS conference, Two-phase modelling for sediment dynamics in geophysical flows, EDF, Chatou, France.

Peltier Y., Erpicum S., Archambeau P., Pirotton M. and Dewals B., 2014. Experimental investigation of meandering jets in shallow reservoir. Environmental Fluid Mechanics, 14(3), 699-710.

Peltier Y., Erpicum S., Archambeau P., Pirotton M. and Dewals B., 2015. Can Meandering Flows in Shallow Rectangular Reservoirs Be Modeled with the 2D Shallow Water Equations?. Journal of Hydraulic Engineering, ASCE, 141(6), 1-10.

Prandtl L., 1925. Bericht über Untersuchungen zur ausgebildeten Turbulenz. Zeitschrift für angewandte Mathematik und Mechanik, 5, 136-139.

Rajaratnam N. and Nwachukwu B., 1983. Flow near groin-like structures. Journal of Hydraulic Engineering, ASCE, 109, 463-480.

Rastogi A.K. and Rodi W., 1978. Predictions of heat and mass transfers in open channels. Journal of the Hydraulic Division (ASCE), 104, 397-420

RD Instruments (RDI), 2006a. Acoustic Doppler Current Profiler - Principles of Operation, Third edition for broadband ADCPs, San Diego, CA.

RD Instruments (RDI), 2006b. Workhorse Rio Grande ADCP, Datasheet. www.rdinstruments.com.

RD Instruments (RDI), 2006c. StreamPro ADCP, Datasheet. www.rdinstruments.com.

RD Instruments (RDI), 2011. WinRiver II, Software User's Guide, San Diego, CA.

Rennie C.D., Millar R.G. and Church M.A., 2002. Measurement of bedload velocity using an acoustic Doppler current profiler. Journal of Hydraulic Engineering, ASCE, 128, 473-483.

Rhoads B.L. and Kenworthy S.T., 1998. Time averaged flow structure in the central region of a stream confluence. Earth Surface Processes And Landforms, 23, 171-191.

Rodi W., 1984. Turbulence Models and Their Applications in Hydraulics, 2nd edition. IAHR Monograph, Rotterdam, the Netherlands

Rozovskii I.L., 1954. Concerning the Question of Velocity Distribution in Stream Bends. DAN URSR (Report of the Academy of Sciences of the Ukraine), 1.

Schlichting H., 1979. Boundary layer theory. McGraw-Hill Book Company, New York.

Socolofsky S.A. and Jirka G.H., 2002. Environmental Fluid Mechanics, Part I: Mass Transfer and Diffusion. Engineering Lectures, 2nd edition, Institut für Hydromechanik, Universität Karlsruhe.

Shen C., Niu J., Anderson E.J. and Phanikumar M.S., 2010. Estimating longitudinal dispersion in rivers using Acoustic Doppler Current Profilers. Advances in Water Resources, 33, 615-623.

Soulsby R.L., 1981. Measurements of the Reynolds stress components close to a marine sand bank. Marine Geology, 42, 35-47.

Stacey M.T., Monismith S.G. and Burau J.R., 1999. Observations of Turbulence in a Partially Stratified Estuary. Journal of Physical Oceanography, 29, 1950-1970.

Stansby P.K., 2003. A mixing-length model for shallow turbulent wakes. Journal of Fluid Mechanics, 495, 369–384

Stansby P.K., 2006. Limitations of Depth-Averaged Modeling for Shallow Wakes. Journal of Hydraulic Engineering, ASCE, 132, 737-740

Steffler P. and Blackburn J., 2002. River2D - User Manual, University Of Alberta

Steidl J., 2014. ADCP - Messungen im Hochgebirgsspeicher Wasserfallboden. Master Thesis, Graz University of Technology.

US Army Corps of Engineers, 2011. Verification and Validation of the Coastal Modeling System, Report 3, CMS-Flow: Hydrodynamics. Coastal and Hydraulics Laboratory, U.S. Army Engineer Research and Development Center.

USGS, 2006. Estimates of Shear Stress and Measurements of Water Levels in the Lower Fox River near Green Bay, Wisconsin. Scientific Investigations Report 2006–5226 by Stephen M. Westenbroek, U.S. Geological Survey, Reston, Virginia.

Van Rijn, L.C., 1984. Sediment Transport, Part III: Bed forms and alluvial roughness. Journal of Hydraulic Engineering, ASCE, 110 (12), 1733-1755.

Van Rossum G. et al., 2013. Python Language Website. www.python.org.

Verbund VHP, 2007. Die Kraftwerke an der österreichischen Drau. Brochure, Villach, Austria.

Vionnet C.A., Tassi P.A. and Martin Vide J.P., 2004. Estimates of flow resistance and eddy viscosity coefficients for 2D modelling on vegetated floodplains. Hydrological Processes, 18, 2907-2926.

Williams E. and Simpson J.H., 2004. Uncertainties in Estimates of Reynolds Stress and TKE Production Rate Using the ADCP Variance Method. Journal of Atmospheric and Oceanic Technology, 21, 347-357.

Wu W., Wang P. and Chiba N., 2004. Comparison of Five Depth-Averaged 2-D Turbulence Models for River Flows. Archives of Hydro-Engineering and Environmental Mechanics, 51, 183-200.

Wu W., 2008. Computational River Dynamics. Taylor & Francis, London

List of Figures

List of Tables

Appendix

About the author

Personal Data

Name:	Clemens Dorfmann
Birth date:	28.12.1978
Place of birth:	Bozen (Italy)
Nationality:	Italy

Education

2007 - 2017	Doctoral Programme in Engineering Sciences Graz University of Technology, Graz (Austria)
2007	Award NEPTUN Wasserpreis of the master thesis (Federal Ministry of Agriculture, Forestry, Environment and Water Management, Austria)
2004 - 2005	One year Erasmus study at the University of Padova, Italy, with focus on hydrology, hydrodynamics and hydraulic engineering
1999 - 2006	Diploma Study Civil Engineering at the Graz University of Technology, Specialization study: "Water and Environment". Master Thesis: Optimierung der Ab- und Aufstauvorgänge bei Stauraumspülungen an der Oberen Mur
1998 - 1999	Study Civil Engineering and Project Management at the University of Applied Science (FH Kärnten), Spittal an der Drau, Austria
1993 - 1998	Scientific High School, J.Ph.Fallmerayer, Brixen, Italy

Professional Experience

2007 - 2016	Project and University Assistant at the Institute of Hydraulic Engineering and Water Resources Management, Graz University of Technology, Graz
May 2008	Visiting Researcher at the Norwegian University of Technology, Prof. Nils Reidar Olsen: 3-D sediment transport modelling of reservoir flushing with SSIIM

Teaching / Co-lecturer as University Assistant

- Basic Hydraulics (Undergraduate studies)
- Hydraulic Engineering (Undergraduate studies)
- Advanced Hydraulics (Master studies)
- River and Sediment Hydraulics (Master studies)
- Numerics in Hydraulic Engineering (Master studies)
- Supervision of Master thesis as well as Master and Bachelor projects

Research Projects carried out at the Institute (2007-2016)

Numerische Berechnungen und Monitoring Feldversuch, Grundablass Drossensperre, 2007
Project work. 1D hydraulic modelling, Hec-Ras

Numerische Berechnungen, Murverlegung Unzmarkt, 2008
Project work. 1D hydraulic and sediment transport modelling, Hec-Ras

Numerische Berechnungen, KW Schönau an der Enns, 2010
Project co-work. 3D hydraulic and sediment transport modelling, SSIIM

Numerische Berechnungen, KW Kendlbruck an der Mur, 2011
Project co-work. 2D hydraulic and sediment transport modelling, Telemac-2D

Numerische Berechnung, Hochwasserschutz Villach, 2011
Project work. 2D hydraulic modelling, Telemac-2D

Entsanderanlage Högmoos, Numerische Berechnung, 2011
Project co-work. 2D hydraulic modelling, Telemac-2D

Numerische Berechnungen, KW Leoben, 2012
Project co-work. 2D hydraulic and sediment transport modelling, Telemac-2D

Numerische Berechnungen, KW Niklasdorf an der Mur, 2012
Project co-work. 2D hydraulic modelling, Telemac-2D

Numerische Berechnungen, KW Ferschnitz and der Ybbs, 2012
Project work. 3D hydraulic and sediment transport modelling, Telemac-3D

Numerische Berechnungen, KW Fisching, 2013
Project co-work. 3D hydraulic and sediment transport modelling, Telemac-3D

Numerische Berechnungen, Hochwasserschutz Schöckelbach, 2013
Project work. 2D hydraulic modelling, Telemac-2D

Ökologische Ersatz- und Ausgleichsflächen Brenndorfer Bucht-West, 2013
Project work. 2D hydraulic modelling, Telemac-2D

Numerische Berechnungen im Stauraum des Kraftwerks Edling an der Drau, 2014
Project work. 2D and 3D hydraulic modelling, Telemac-2D and Telemac-3D

Ökologische Ersatz- und Ausgleichsflächen Brenndorfer Bucht-Ost, 2014
Project work. 2D hydraulic modelling, Telemac-2D

ADCP Messungen im Speicher Wasserfallboden, 2014
Project work. Measurements of flow fields and suspended load concentrations

ADCPtool: Entwicklung der Open Source ADCP postprocessing Software, 2014
Project work and supervision

Bed Load Analyzer: Entwicklung der Software zur Berechnung von hydraulischen und sedimentologischen Parametern in gegliederten Querschnitten, 2012-2015
Project work and supervision

Grundsatzstudie Stauraum KW Edling, 2015
Project work. Analysis of the sedimentation evolution in the reservoir

Plabutschtunnel, Ausgießversuch, Monitoring Ost- und Weströhre, 2015
Project work. Field measurements

Numerische Berechnungen, Selkacher Bucht, KW Feistritz-Ludmannsdorf an der Drau, 2016
Project co-work. 3D hydraulic and sediment transport modelling, Telemac-3D

Plabutschtunnel, Ausgießversuch, Monitoring Ost- und Weströhre, 2016
Project work. Field measurements

Plabutschtunnel, Siphon Monitoring Oströhre, 2016
Project work. Field measurements

Lainbergtunnel, Ausgießversuch, Monitoring, 2016
Project work. Field measurements

European Space Agency (ESA): Enhanced Flood Forecasting System for Critical Infrastructure Protection in Medium Size Alpine Catchments (EFFORS), 2013-2017

Physical model studies

Vollmodell KW Feistritz-Ludmannsdorf an der Drau, 2010
Project work, Optimization of the sediment management in the reservoir

Vollmodell KW Schönau an der Enns, 2010
Project co-work. Optimization of the sediment management in the reservoir

Schnittmodell KW Ferlach an der Drau, 2010
Project work. Investigation of the weir capacity and the stilling basin performance

Schnittmodell KW Annabrücke an der Drau, 2010
Project work. Investigation of the weir capacity and the stilling basin performance

Schnittmodell KW Feistritz-Ludmannsdorf an der Drau, 2011
Project work. Investigation of the weir capacity and the stilling basin performance

Vollmodell Siphon, Lainbergtunnel, 2016
Project work. Investigation and optimization of discharge capacity of the siphon

Vollmodell Denil-Fischpass, 2016
Project work. Investigation and measurements of the velocity distribution and turbulence

Organizer of Workshops

- Hybrid Hydraulic Modelling – Application, Methods, Challenge. In cooperation with University of Ljubljana, Graz, 06.05.2009
- 3D numerical modelling with Fluent, Flow-3D and SSIIM – Theory, Applications and Practice. Benchmark workshop in cooperation with University of Innsbruck, Graz, 20.-21.11.2009
- openTELEMAC-MASCARET workshop. For Austrian civil engineering companies, Graz, 13.05. 2013
- Application of the numerical modelling open source suite openTELEMAC-MASCARET. Workshop, University of Innsbruck, Innsbruck, 21.-22.11.2013

- Hydraulische Modellierung von Fließgewässern mit Open Source Software. With Uwe Merkel, Graz, 09.07.2014

Board Member

- ÖWAV (Austrian Water and Waste Management Association): Working group: ”Surge and sink waves – ecological and energy related challenges”, 2007-2008
- Federal Ministry of Agriculture, Forestry, Environment and Water Management: Working group: ”Development of the guideline for the estimation of the dam-break outflow hydrographs and the related flood analysis”, since 2014
- Scientific Committee, openTELEMAC-MACARET consortium, since 2015

Reviewer

- Journal of Hydraulic Research
- Water - Open Access Journal

Participation in Seminars and Workshops (most relevant)

- Fachtagung: Nachfragegerechte Stromversorgung: vielfältige Chancen für die Wasserkraft, Glarus, Schweiz, 06.-07.2007
- DWA Seminar: Entlandung von Stauräumen, Stuttgart, 27.09.2007
- DWA, 10. Gewässermorphologisches Kolloquium: Sedimentmanagement in Flussgebieten, Koblenz, 05.-06.11.2007
- ÖWAV Seminar: Schwebstoffe im Fließgewässer - Erfassung des Schwebstofftransportes, Wien, 26.03.2009
- ÖWAV Seminar, Speicher- und Pumpspeicherkraftwerke, Planung, Bau und Betrieb, Graz, 23.09.2009
- AGAW Symposium, Wasserrahmenrichtlinie und Versorgungssicherheit, Villach, 01.-02.10.2009
- River Flow 2010, International Conference on Fluvial Hydraulics, Master Class: Sediment in reservoirs, Nils Reidar B. Olsen & Thorsten Stoesser, Braunschweig, 07.-10.09.2010
- South East Europe (SEE) Hydro Power Symposium, Wasser – Energie und Lebensraum, Graz, 30.09.2010
- UFRIM, Urban Flood Risk Management, International Symposium, Graz, 21.-23.09.2011
- ÖWAV Seminar, Speicher- und Pumpspeicherkraftwerke, Investitionssicherheit, Marktumfeld und technische Lösungen, Graz, 29.11.2012

- 12th International Benchmark Workshop on Numerical Analysis of Dams, ICOLD, Graz, 02.-04.10.2013
- Schwall und Sunk: Forschungsstand & Ausblick, 6. Expertentag, Verein für Ökologie und Umweltforschung, Wasser Cluster Lunz, Lunz am See, 20.-21.05.2014
- BAW Kolloquium: Herausforderung Sedimenttransport – Methoden und Konzepte im Flussbau, Karlsruhe, 26.11.2014

Co- supervision of Master Thesis

Wasserwirtschaftliches Management der Kraftwerksanlagen an der Pöls. Georg Edelsbrunner and Jakob Friess, 2008

1D-numerische Untersuchungen der Abflussvorgänge an der Lutz-Vorarlberg. Knut Sterlé, 2008

2D-numerische Untersuchungen der Abflussvorgänge an der Lutz-Vorarlberg. Peter Prossliner, 2008

3-D numerische Modellierung von Laborversuchen in einem Glasgerinne. Christoph Ortner, 2009

2-D numerische Modellierung eines Wehrüberfalls. Marco Oblasser, 2011

Entwicklung einer Software zur Berechnung von hydraulischen und sedimentologischen Kennwerten in gegliederten Flussquerprofilen. Reinhard Fleißner, 2013

Optimierung der Ab- und Aufstauvorgänge an der Görtschitz. Stefanie Knauhs and Katharina Sammer, 2014

Untersuchung von Spüleinrichtungen zur Reinigung von Stauraumkanälen der Mischwasserbewirtschaftung. Thomas Golger, 2014

Grundlagen der ADCP-Messtechnik und Auswertung von Messdaten. Shkelzen Kryeziu, 2014

ADCP Messungen im Hochgebirgsspeicher Wasserfallboden. Jakob Steidl, 2014

2D Numerical Simulations of Dam Failure. Konrad Moser, 2014

3D-numerische Berechnung der Wehrförderfähigkeit für ein Flusskraftwerk. Fabian Gottfried Heinzle, 2014

Morphodynamic Modelling of Sediment Control Groynes in a Meandering River entering a Reservoir. Zhina Mohammed. University of Ottawa, with Prof. Colin Rennie, 2016

Hydromorphological assessment applied on a stretch on river Sulm. Julia Cancola, 2016

Publications

Dorfmann C. and Knoblauch H., 2008. ADCP measurements in a reservoir of a run-of-river Hydro Power Plant. 6th International Symposium on Ultrasonic Doppler Methods for Fluid Mechanics and Fluid Engineering, Prague.

Dorfmann C. and Knoblauch H., 2008. 2D numerische Modellierung am Speicher des Draukraftwerks Feistritz. Wasserbausymposium, Eigenverlag der Versuchsanstalt für Wasserbau, Hydrologie und Glaziologie, ETH Zürich, 207-1, 327-336.

Dorfmann C. and Knoblauch H., 2009. Calibration of 2-D and 3-D numerical models of a large reservoir using ADCP measurements. Water Engineering for a Sustainable Environment, Proceedings of the 33th IAHR Congress, Vancouver, Canada.

Dorfmann C., Knoblauch H. and Moser A., 2010. Physikalische und numerische Modellierung des Strömungsverhaltens im Stauraum des KW Feistritz-Ludmannsdorf an der Drau. Österreichische Wasser- und Abfallwirtschaft. 62, 3-4, 62-66.

Harb G., Haun S., Zechner S., Dorfmann C. and Schneider J., 2011. The influence of secondary currents on reservoir sedimentation – experimental and numerical studies. Proceedings of the 34th IAHR World Congress, Brisbane, Australia.

Dorfmann C., Harb G. and Zenz G., 2012. Simulation of hydrodynamic and sediment transport processes – Two Austrian case studies. Proceedings of the XIXth Telemac-Mascaret User Conference, HR Wallingford, Oxford, UK.

Harb G., Dorfmann C., Schneider J., Haun S. and Badura H., 2012. Numerical analysis of sediment transport processes in a reservoir. Proceedings of the 6th International Conference on Fluvial Hydraulics, River Flow 2012, San Jose, Costa Rica.

Haun S., Dorfmann C., Harb G. and Olsen N. R., 2012. 3-D numerical modelling of the reservoir flushing of the Bodendorf reservoir, Austria. IAHR Europe Congress, Munich.

Harb G., Dorfmann C. and Badura H., 2012. Vergleich von 2D und 3D numerischen Simulationen für die Berechnung von Wasserspiegellagen und Sohlschubspannungen. Wasserbausymposium. Verlag der Technischen Universität Graz, 291-299, Graz.

Oblasser M., Dorfmann C. and Zenz G., 2012. 2-D und 3-D numerische Modellierung eines Wehrüberfalls. Wasserbausymposium. Verlag der Technischen Universität Graz, 159-166, Graz

Fleißner R. and Dorfmann C., 2012. Entwicklung einer Software zur Berechnung von Wasserspiegel und Sedimenttransport in gegliederten Querschnitten. Wasserbausymposium. Verlag der Technischen Universität Graz, 29-37, Graz

Dorfmann C., Steidl J. and Zenz G., 2013. ADCPtool: an open source ADCP postprocessing framework. Proceedings of the 35th IAHR World Congress, Chengdu, China.

Dorfmann C. and Zenz G., 2013. Numerische Untersuchungen mit Telemac bei Wasserkraftanlagen – zwei Fallstudien. Wasserwirtschaft, 12, 41-46.

Dorfmann C. and Zenz G., 2013. Development of a Flood Forecasting System for Medium Size Alpine Catchments. Abstract in the proceedings of the XXth Telemac-Mascaret User Conference, Bundesanstalt für Wasserbau (BAW), Karlsruhe, Germany.

Saberi O., Dorfmann C. and Zenz G., 2013. 2D hydraulic modelling of a dam break scenario. Wasserbausymposium. ICOLD Benchmark Workshop, 36, 283-292, Austrian National Committee on Large Dams, Graz

Harb G., Dorfmann C., Badura H. and Schneider J., 2014. Numerical Analysis of Sediment Transport Processes during a Flushing Event of an Alpine Reservoir. Proceedings of the 8th International Conference on Fluvial Hydraulics, River Flow 2014, Lausanne, Switzerland.

Dorfmann C., Moser K. and Zenz G., 2014. 2D Numerical Simulations of Embankment Dam Failure Due To Overtopping. Proceedings of the XXIth Telemac-Mascaret User Conference, Artelia, Grenoble, France.

Dorfmann C., 2014. Modelle für Wasserströmungen. High Performance Computing in Österreich. Brochure of the Vienna Scientific Cluster (VSC), Wien.

Dorfmann C., Redtenbacher M. and Zenz G., 2015. Investigating the sediment transport processes in a river meander. Abstract in the proceedings of the XXIIth Telemac-Mascaret User Conference, STFC Daresbury Laboratory, Warrington, UK.

Dorfmann C. and Zenz G., 2015. Numerische Untersuchungen mit Telemac bei Wasserkraftanlagen – zwei Fallstudien. In Wasserkraftprojekte Band II, Ausgewählte Beiträge aus der Fachzeitschrift Wasserwirtschaft, Entwicklungen, Herausgeber: Stephan Heimerl, Springer Vieweg, 124-132.

Schneider J., Zenz G. and Dorfmann C., 2016. Ökologische und Morphologische Verbesserung bei einem Laufkraftwerk. 14. Symposium Energieinnovation, Energie für unser Europa, Graz.

Dorfmann C. and Zenz G., 2016. The depth-averaged Mixing Length turbulence model for Telemac-2D. Proceedings of the XXIIIth Telemac-Mascaret User Conference, Électricité de France (EDF), Paris, France.